Università Campus Bio-Medico di Roma

School of Engineering

PhD Course in Biomedical Engineering

(XXV - 2010/2012)

Microtechnologies for compliant interfaces between manipulated objects, hand prostheses and the nervous system

Maria Teresa Francomano

Coordinator

Prof. Giulio Iannello

Supervisors

Prof. Eugenio Guglielmelli

Prof. Dino Accoto

April 23, 2013

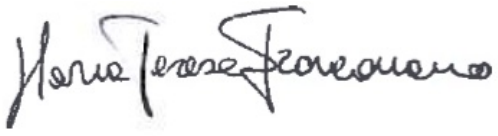

Microtechnologies for compliant interfaces between manipulated objects, hand prostheses and the nervous system

A thesis presented by

Maria Teresa Francomano

in partial fulfilment of the requirements of the degree of

Doctor of Philosophy

in Biomedical Engineering

Coordinator

Prof. Giulio Iannello

Supervisors

Prof. Eugenio Guglielmelli

Prof. Dino Accoto

April 23, 2013

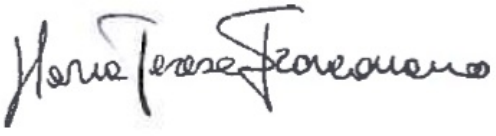

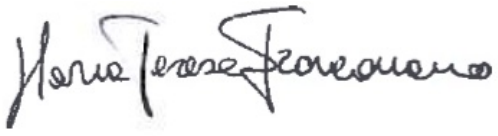

Table of contents

Abstract 11

List of figures 13

List of tables 19

Chapter 1

Introduction 21

1.1. Thesis overview 23

Bibliography 25

Chapter 2

Hand capabilities: from Humans to Prosthetics 26

2.1. Hand main functions and control 26

2.2. Hand sensory system 27

2.2.1. Human hand mechanoreceptors 28

2.2.2. Slip perception 31

2.2.2.1. Basic definitions 31

2.2.2.2. Human slip sense 33

2.3. Hand Prosthetic Devices: State of the Art 36

2.3.1. Commercial devices 38

2.3.2. Research prototypes 40

2.4. Discussion 42

2.5. Conclusion 44

Bibliography 46

Maria Teresa Francomano

Chapter 3

Neural Interfaces 52

3.1. Organization of the PNS 53

3.2. Peripheral neural interfaces: State of the Art 54

3.3. A novel implantable peripheral interface: The concept 56

3.3.1. Electromagnetic Stimulation of PNS 60

3.4. Feasibility analysis of the proposed approach 61

3.5. Discussion 64

Bibliography 67

Chapter 4

The artificial sense of touch 71

4.1. The importance of the tactile feedback 71

4.2. Main Requirements for Tactile Sensory Systems 72

4.3. Artificial tactile sensors 74

4.3.1. Capacitive tactile sensors 74

4.3.2. Piezoresistive tactile sensors 75

4.3.3. Piezoelectric tactile sensors 76

4.3.4. Inductive tactile sensors 76

4.3.5. Optoelectric tactile sensors 76

4.3.6. Strain gauges 77

4.4. Slip sensors 77

4.4.1. Displacement sensors 79

4.4.2. Microvibration transducers 80

4.4.2.1. Accelerometers 81

4.4.2.2. Acoustic detectors 81

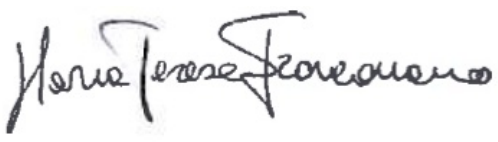

4.4.2.3. Piezoelectric materials 82

4.4.2.4. Piezoresistive materials 83

4.4.2.5. Photoelastic materials and photoelectric devices 83

4.4.2.6. Others 84

4.4.3. Force sensors 84

4.4.4. Heat microfluxes detectors 85

4.4.5. Discussion 86

4.5. Artificial tactile skins 90

4.6. Conclusion 91

Bibliography 93

Chapter 5

Flexible sensors for prosthetic hands 100

5.1. Flexible technologies and materials 101

5.2. A thermal slip sensor 102

5.2.1. Working principle 103

5.2.2. The rigid prototype 104

5.2.3. Optimization design 108

5.2.3.1. Geometrical model 108

5.2.3.2. FEM Thermal Analysis 109

5.2.3.3. Dimensional Analysis 109

5.2.3.4. Thermal model 113

5.2.3.5. Sensitivity Analysis 113

5.2.4. Optimized sensor development 114

5.2.5. Thermal slip sensor on flexible substrate 116

5.2.5.1 Fabrication and thermal characterization 116

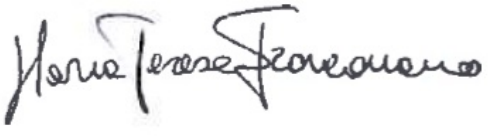

5.2.5.2. Experimental set-up 120

5.2.5.3. Detection strategy 122

5.2.5.4. Results and Discussion 125

5.3. Flexible arrays of thermal slip sensors 130

5.3.1. Design 130

5.3.2. Array Microfabrication 130

5.3.3. Array control 132

5.3.4. Set-up 133

5.3.5. Results 134

5.4. Flexible multilayered silicon structures 136

5.4.1. Optimal SU-8 thickness for metallization integrity 136

5.4.2. FEM analysis 138

5.4.3. Results 139

5.5. Discussion 141

Bibliography 144

Chapter 6

Engineered surface for adhesion control 147

6.1. A novel technique for modulating adhesion forces 149

6.1.1. Theoretical background 149

6.1.2. The electrowet adhesion 151

6.1.3. Active surface development 152

6.1.4. The experimental set-up 152

6.1.5. Experimental protocol 155

6.2. Results and Discussion 156

6.3. Conclusion 159

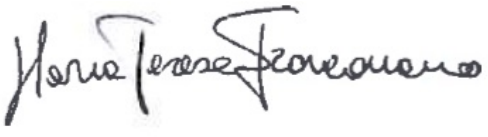

Chapter 7

Stretchable sensorized skin for prosthetic hands 162

7.1. Flexible versus stretchable substrates 163

7.2. Stretchable materials 164

7.3. Stretchable technologies 164

7.3.1. Wavy layouts 166

7.3.2. Open meshes 168

7.4. Flexible Poliurethane (PU) Foam as stretchable substrate 169

7.5. Soft Contact/Pressure Sensors on a stretchable PU Foam 172

7.5.1. Skin design 173

7.5.2. Sensors detection strategy 175

7.5.3. Skin Fabrication 177

7.5.4. Experimental tests 177

7.5.4.1. Experimental set-up 178

7.5.4.2. Results and Discussion 182

7.6. Development of Crystalline Foams 186

7.7. Discussion 191

Chapter 8

Conclusion 195

8.1. Overview of the presented work 196

8.2. Major achievements beyond the state of the art 198

8.3. Further improvements and potential impact 199

List of Publications 202

Acknowledgements 205

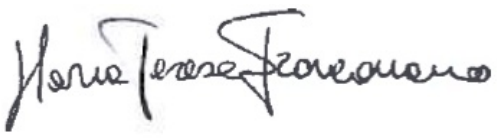

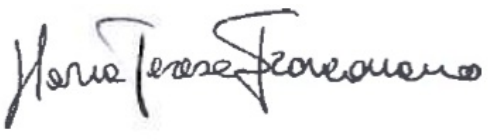

Abstract

Some factors in the field of upper limb prosthetics impede the usability of most advanced devices. The main limitations deal with two challenges, namely: *i)* the restoration of a bidirectional comunication channel with the Central Nervous System (CNS), which would allow the direct control of the prosthesis; and *ii)* the provision of a rich sensory feedback for providing the necessary information about the contact conditions to the low level control of the prosthesis, thus enabling dexterous manipulation tasks.

This PhD thesis investigates novel solutions for overcoming the mentioned limitations, for reliably interfacing the prosthetic hand and the human neural system as well as the former to the external environment.

To this aim, aspects of neurophysiology, microtechnology, robotics and material science have been integrated.

Starting from the study of neural interfaces state-of-the-art, the theoretical feasibility analysis of a novel bidirectional interface between upper limb prosthetic devices and the CNS, based on electromagnetic stimulation of the neurons and electrical recording of their responses, is presented. Results show that microprobes, integrating microcoils and planar electrodes, could represent a promising alternative to existing solutions, nowadays based on pure electrical means and whose performace, especially during stimulation, are prone to be affected by fibrotic reactions.

As it regards exteroceptive interfaces, the focus is on tactile sensors, based on thin film technologies, easily integrable on artificial skins and with a low computational cost. Capacitive pressure sensor arrays and thermal slip sensors, which, from a comparative analysis of the state-of-the-art, appear among the most promising solutions for the specific application, have been developed and tested.

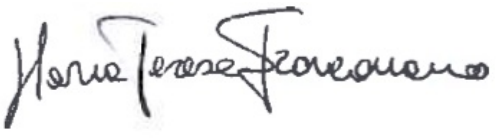

Finally, friction enhancing mechanisms have been investigated for improving the grasp stability, especially when wet objects are contacted, without increasing the cognitive burden of the user. In particular, a novel mechanism, named *electrowet adhesion*, based on electrowetting and wet adhesion techniques, has been investigated and its feasibility has been proved by means of tests performed using an *ad hoc* engineered surface. Tests show the capability of this device of actively modulating the adhesion force at the interface with wet substrates by acting on external electric fields. This surface can be further miniaturized and developed on a flexible substrate, thus being technologicaly compatible with the tactile sensors, with which it would constitue an artificial skin.

Special attention has been paid on choosing soft materials (flexible or stretchable) for all the technological solutions presented, in order to guarantee compliance, to avoid mechanical mismatches at the interface and to allow the foldability of the developed devices around complex surfaces.

The work is organized in seven Chapters, starting with the analysis of the state-of-the-art. The main outcomes are analyzed and discussed in each Chapter, wherease conclusions and the impact of the work presented are discussed in Chapter 8.

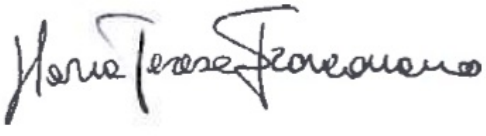

List of figures

1.1. Schematic of the interrupted link between the upper-limb amputee and the external environment 22

2.1. Skin mechanoreceptors..... 31

2.2. Grasping forces during weight lifting..... 32

2.3. Neural pathway of grasp stability control..... 35

2.4. Timeline of the main progresses in the upper limb prosthetic field..... 40

2.5. Research prototypes of prosthetic hands..... 41

2.6. Main challenges of upper limb prostheses..... 44

3.1. Spinal nerves of the upper limb..... 52

3.2. Peripheral nerve structure..... 54

3.3. Invasive interface classification..... 56

3.4. Concept of the novel PNS interfaces..... 58

3.5. Microprobes intra-neural configuration..... 59

3.6. Microprobes Cuff configuration..... 59

3.7. Typical spatial distribution of $(\partial E_x)/\partial x$ generated by a square coil..... 63

4.1. Number of publications (on the left) and citations (on the right)..... 78

4.2. Slip sensors: a taxonomy based on the detected physical quantity associated to slip..... 78

4.3. Slip detection by displacement monitoring. Slip causes the motion of a point within the contact area..... 79

4.4. Slip detection by microvibrations monitoring..... 80

4.5. Slip detection by monitoring thermal changes in thermal microfluxes..... 86

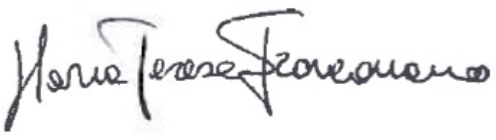

4.6. Comparison of slip detection strategies..... 90

5.1. Schematic of the slip sensor..... 105

5.2. Steps of the lift-off process..... 105

5.3. Snapshot of the fabricated slip sensor..... 104

5.4. Control scheme of the rigid slip sensor..... 107

5.5. Sensor response time for one test, performed using a bar of delrin..... 107

5.6. FEM simulations relating the power dissipation and different slip speeds 110

5.7. Relation between A and 1/Fo..... 111

5.8. Linear relation between A and 1/Fo..... 112

5.9. Footprint of the optimized sensor metal part..... 117

5.10. Fabrication process of the optimized sensor..... 115

5.11. A 3D schematic of the flexible sensor..... 115

5.12. Microfabrication process..... 118

5.13. Picture of a bent slip sensor..... 118

5.14. Thermal characterization of the flexible sensor..... 119

5.15. Experimental relation between the current supplied to the sensing element and its resistance variations when the sensor is suspended in air..... 120

5.16. Electromechanical performance of the thermal slip sensor during bending..... 120

5.17. Experimental set-up..... 121

5.18. States diagram..... 124

5.19. Simplified logical circuit, implementing the bang-bang temperature control..... 125

5.20. CVT vs. Thermal conductivity for the tested materials 127

5.21. Dissipated power vs. thermal diffusivity for the tested materials..... 128

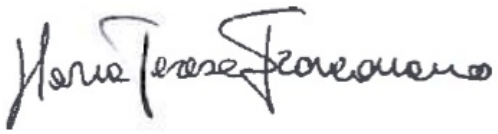

5.22. CV vs numer of crank turns, during a slip test..... 129

5.23. Response time of the thermal slip sensor..... 129

5.24. Array of slip sensors..... 131

5.25. Schematic of slip directions detection (A) and array control (B)..... 132

5.26. Workplow of the array control algorithm..... 133

5.27. Experimental set-up for testing the array control software..... 134

5.28. Simulated slipping path (a-l)..... 135

5.29. Detected slipping path, using the developed control algorithm..... 135

5.30. Schematic of the laminated device cross section 137

5.31. Maximum normalized curvatures (log) in function of SU-8 thickness (um, log)..... 139

5.32. Maximum curvature as a function of SU-8 thickness..... 140

5.33. Maximum curvatures allowed as a function of SU-8 thickness..... 141

6.1. Schematic representing the wet adhesion mechanism..... 149

6.2. EWOD configuration. θ is contact angle and ΔV is the applied voltage..... 151

6.3. Wetting phenomenon in a solid-walled channel. Liquids (1) and (2) are immiscible..... 151

6.4. Example variation of the contact angle due to the application of an electric field..... 153

6.5. Charge distribution on the PDMS vertical walls when an electric field is applied..... 154

6.6. Cross section of testing device..... 154

6.7. Experimental set-up..... 155

6.8. Example of obtained data during a trial..... 156

6.9. One-way ANOVA test applied to patterned PDMS surface. Class 0: no voltage applied; Class 1: 60V applied..... 157

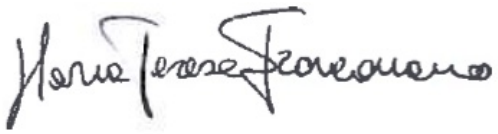

6.10. One-way ANOVA test, related to data obtained when voltage is not applied, both for patterned (Class 0) and flat (Class 1) PDMS layers..... 158

6.11. One-way ANOVA test, related to data obtained when voltage is applied, both for patterned (Class 0) and flat (Class 1) PDMS layers..... 158

6.12. Comparison between trials performed using a flat PDMS layer, when voltage is applied (Class 1) and not (Class 0), and using a patterned PDMS layer when voltage is applied (Class 2)..... 159

7.1. Ways of stretching..... 165

7.2. Out-of-plane wavy layouts..... 167

7.3. Sinusoidal 2D springs for electrical interconnections..... 168

7.4. 2D spring shaped electrical connections..... 169

7.5. Open meshes stretchable interconnections..... 169

7.6. FPF layer. A. Top view; B. Cross section..... 170

7.7. Bar coating of a FPF layer..... 170

7.8. Variety of foam densities..... 171

7.9. Stress-strain curves Plain PU elastomer (Black), Rigid (Red) and Soft (Blue) FPF substrates under tensile loading..... 171

7.10.Thin gold film deposited on a FPF layer..... 172

7.11. Strain localization of metal cracks above air cells (during stretching)... 172

7.12. Gold path integrity above bulk PU zones, after the application of cyclic uniaxial deformations..... 173

7.13. 3D rendering of the multilayered skin..... 174

7.14. A. Schematic of the capacitive sensors array. B. Sensing areas (2 capacitive sensors are present within each area), distributed along a robotic finger..... 174

7.15. Schematic of each sensing unit, whose capacitance is: C=C1+C2..... 175

7.16. Schematic of a planar capacitor..... 175

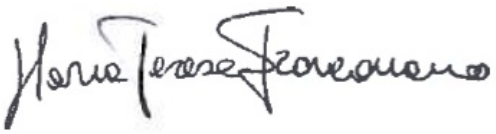

7.17. Capacitor local deformation resulting in a local change of the electrode area A (A+ΔA)..... 176

7.18. Main steps of the sensorized skin fabrication process..... 178

7.19. Experimental set-up for capacitance measurements..... 179

7.20. Block diagram of the AD7147 evaluation board..... 180

7.21. A. Snapshot of two FPCBs (one per each phalanx); B.The 4 connections endings of the FPBC, to be connected to the custom-made board; C: Back side of one FPCB, showing PADs..... 181

7.22. Block diagram of the FPCB..... 181

7.23. Contact tests..... 182

7.24. Capacitance variations (with respect to the measured capacitance when no pressure is applied) occurring in correspondence of one of the sensing unit, versus applied pressures..... 183

7.25. Schematic of soft capacitive sensors deformation when a force F is applied..... 184

7.26. Best fitting of experimental data..... 184

7.27. Example of data obtained during one trial when different pressure are applied on the same sensing unit..... 185

7.28. An example of multitouching..... 185

7.29. On-off sensor response, once pressed by human finger..... 186

7.30. a) Whole microfluidic chip sizes; b) Channels dimensions..... 187

7.31. Main steps of the microfluidic chip fabrication 188

7.32. Photos of the SU-8 Master mold (A) and of the PDMS replica (B) 188

7.33. Microfluidic chip packaging. (A) is the foam reservoir..... 189

7.34. Pinch-off mechanism at the orifice. Q_l is he liquid flow, and P_g is the gas pressure..... 189

7.35. Experimental set-up..... 189

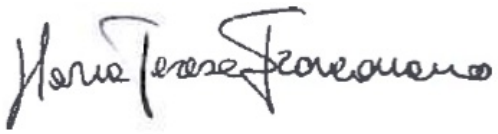

7.36. Pattern obtained in the output channel..... 190

7.37. SEM image of an obtained foam..... 190

8.1. Main PhD thesis addressed issues..... 195

Maria Teresa Francomano

List of tables

2.1. Main features of hand mechanoreceptors..... 29

2.2. Schematic of mechanoreceptors types and related features..... 30

3.1. Peripheral neural interfaces classification..... 55

4.1. Main tactile sensors requirements for prosthetic robotic hands..... 73

4.2. Main advantages and disadvantages of tactile force sensors..... 74

4.3. Main advantages and disadvantages of the reviewed slip sensors..... 89

4.4. Qualitative evaluation of slip sensors..... 90

5.1. Sensor layers geometrical data..... 109

5.2. Sensitivity analysis outcomes..... 114

5.3. Table of States..... 123

5.4. Logical conditions..... 123

5.5. Truth table..... 124

5.6. Parameters set during trials..... 126

5.7. Thermal properties of bars materials..... 127

5.8. List of symbols..... 137

5.9. Mechanical properties of Si, SU-8, Au, Pt, Cr..... 138

7.1. Measured capacitance values per each sensing unit..... 177

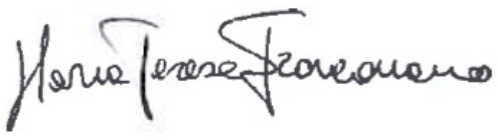

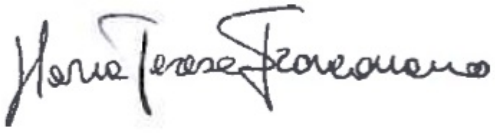

Chapter 1

Introduction

Technological advances in the emerging field of Biomedical Robotics are steadily growing within different subdomains (i.e. diagnosis, surgery, rehabilitation), according to societal and patients' needs.

Patients' independent living, safety and quality of life are the most important addressed issues, which stimulate the design of novel human-machine interfaces as well as the development of enabling technologies for sensory systems, mobile energy supply, energy efficiency and biocompatible materials.

Among several pathologic or traumatic causes, *amputation* is a common source of physical disability, which entails the occurrence of the phantom limb pain syndrome as well as negative repercussions on amputees' daily activities and quality of life.

Subjects with an amputation are affected psychologically, socially and economically.

Part of the rehabilitation iter, after an amputation, may include training with an artificial limb as the use of a prosthesis allows restoring body acceptance [Saradjian, 2008].

Nevertheless, for upper-limb amputees it is of huge importance the restoration of the lost link between the body and the external environment (Figure 1.1), in order to accomplish manipulation tasks, which encompass about 60% of daily life activities [Faria, 2012].

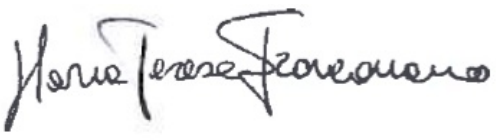

To this aim, an ambitious challenge focuses on the development of an upper limb prosthetic device, achieving performance comparable to that of the human hand, especially in terms of dexterity during fine manipulation.

Despite advances in electronics, mechanical design and intelligent grasping control, commercially available hand prostheses still have some limitations which, in most cases, impede their usability.

This is mainly due to interfacing problems, which do not allow restoring an effective sensory-motor feedback.

Figure 1.1: Schematic of the interrupted link between the upper-limb amputee and the external environment.

By definition, an interface is a boundary with the surrounding, which influences the interactions with the latter. For amputees, interactions occur:

- between the body and the artifact;
- between the body and the environment, through the artifact.

Therefore, it is of great importance to develop interfaces, which should allow, in an as natural as possible way, to connect *i)* the artifact to the human body, by establishing a robust and selective bidirectional communication channel with the Central Nervous System (CNS); and *ii)* the human body and the external environment, by restoring a rich sensory feedback.

Maria Teresa Francomano

This confers on engineered interfaces and sensory systems a dominant role: their importance lies also on providing technological improvements, such as new functions, robustness and reliability, to the artifact itself.

1.1. Thesis overview

The aim of this thesis is to investigate how advances in microtechnologies and material science can overcome some of the current limitations of interfacing technologies connecting a prosthetic hand and the human neural system as well as the former and the manipulated objects. To this aim two main topics have been addressed:

1. design of novel bidirectional interfaces between upper limb prosthetic devices and the human CNS;
2. development of exteroceptive interfaces, embedding novel tactile sensors and active substrates on artificial skins.

Special attention has been paid on using a common technological ground and on choosing flexible/stretchable materials, in order to avoid mechanical mismatches at the interface and to allow the foldability of the developed devices around complex surfaces.

In particular, special efforts have been dedicated in:

- Implementing a feasibility analysis of a novel stimulation technique of the Peripheral Nervous System (PNS), based on electromagnetic means.
- Developing and characterizing two different types of tactile sensors: *i)* a novel flexible thermal slip sensor; and *ii)* soft pressure sensors on a stretchable substrate.
- Implementing a novel technique for modulating adhesion forces during the manipulation of wet objects, for achieving a stable grasp.

The thesis is organized as follows. The application scenario is detailed in Chapter 2. The topic 1., i.e. neural interfaces, is addressed in Chapter 3, while Chapters 4-7 focus on exteroceptive interfaces (topic 2.).

Chapter 3 introduces the different existing types of neural interfaces, highlighting their limitations. A new approach, based on the *in situ* electromagnetic

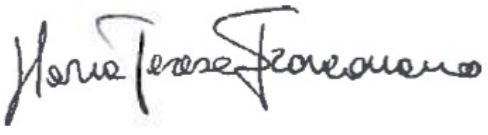

stimulation of the peripheral nerves, is proposed and its feasibility analysis is reported.

Chapter 4 details the artificial sense of touch. Special attention is paid to contact, pressure and slip detection, which are the most important sensing modalities for characterizing static and dynamic events during objects manipulation.

Chapter 5 reports on the development of a novel slip sensor. The sensor, based on thermo-electrical phenomena, is easy to fabricate and robust with respect to *i)* the variety of possible surface features of the handled objects, as well as *ii)* the mechanical noise. Moreover its response time is comparable to those of human mechanoreceptors. An array configuration of slip sensors, capable of detecting object slip direction, is also reported.

Chapter 6 is devoted to a novel technique for modulating the adhesion forces at the interface with wet substrates. It mainly consists in a voltage-controlled method, merging two well established techniques: wet adhesion and electrowetting.

An artificial skin, embedding contact/pressure capacitive sensors, is described in Chapter 7. The skin has been developed on a heterogeneous stretchable substrate. The sensors are able to discriminate contact events occurring with plastic and metal objects, as well as with human fingers. Moreover, they have been preliminarily characterized for detecting applied pressure values.

Finally, Chapter 8 is devoted to conclusions.

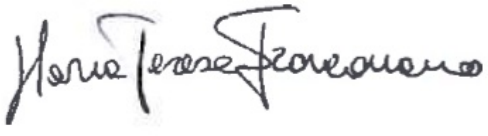

Bibliography

[Faria, 2012] D. R. Faria, R. Martins, J. Lobo, and J. Dias, "Extracting data from human manipulation of objects towards improving autonomous robotic grasping", Robot. Auton. Syst, vol. 60(3), pp. 396-410, March 2012.

[Saradjian, 2008] Saradjian. A, Thompson. R. A, and Datta Dipak. The experience of men using an upper limb prosthesis following amputation: Positive coping and minimizing feeling different. Journal of Disability and Rehabilitation, 30(11), pp. 871-883, 2008.

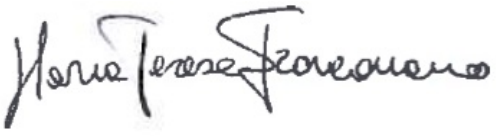

Chapter 2

Hand capabilities: from Humans to Prosthetics

The hand is one of the most fascinating and sophisticated biological systems, with a complex mechanical structure and a composite sensory system. Human hand allows us accomplishing a wide variety of tasks, ranging from multifinger grasping to the individuated movements of single fingers.

Human hand *dexterity* consists in our capability of performing tasks with high speed, fine control (i.e. with high precision and accuracy) while exerting low forces (ranging from 0.1 to 2 N, as in microsurgical tasks [Charles and Williams, 1989; Sabatini, 1989]). Example tasks requiring high dexterity include [Salthouse, 1984]: typing (where the inter-key stroke intervals are in the range 130-170 ms), microsurgery (requiring forces below 2 N with a range of motion of 150-500 um), and playing piano (keystrokes interval: ~56 ms).

Hand dexterity is enabled by both the central and peripheral control capabilities as well as by the high-density tactile receptors in the hand skin, continuously providing information about contact, as needed for operating in unstructured environments and for adapting in real-time interaction forces and fingers configuration.

2.1. Hand main functions and control

The hand functions are basically three:

1. Manipulation of objects;

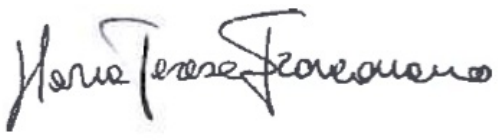

2. Exploration of objects, surfaces, textures, etc., having different properties and temperature;

3. Interaction and communication with the others.

Prehensile movements are a subcategory of manipulation tasks, and they include movements in which an object is seized and held partly or wholly within the compass of the hand.

The fundamental requisite of grasping is that the object, whether it is fixed or freely movable, should be held securely.

Stability may be achieved mainly in two ways: *i)* the object may be held in a clamp formed by the partly flexed fingers and the palm, counter pressure being applied by the thumb lying more or less in the plane of the palm. This is referred to as the *power* grip; and *ii)* the object may be inched between the flexor aspects of the fingers and the opposing thumb. This is called *precision* grip.

The posture of the fingers is controlled by considering the shape of the object, its size as well as the intended activity to be performed.

When the hand is actually grasping an object, normal and tangential forces exerted to its surface are finely coordinated for maximizing stability. Fingertip forces can be synchronized or decoupled when required, e.g. for preventing object slip.

Finger motion, as well as the adaptation of forces, can be controlled thanks to constraints arising in the peripheral biomechanical object-finger coupling, or produced by the innervation of spinal motoneuron pools, or coming from the motor cortex.

The efficacy of the motor control mostly relies on the sensory information coming from the tactile receptors branching beneath the hand skin, as detailed in the next section.

2.2. Hand sensory system

Several studies have been devoted to understand the physiological mechanisms behind the human sense of touch, thus inspiring the development of robotic tactile sensing even more.

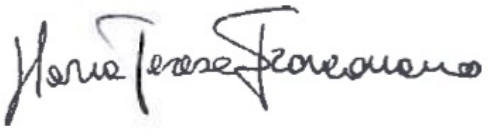

In humans there are two main sensing modalities [Dahiya, 2010]: *i) kinesthetic sensing*, which allows perceiving limb motions and forces, thanks to internal receptors; and *ii) cutaneous sensing*, which allows, by means of skin receptors, to detect static and dynamic events, occurring at the external surface of the skin.

Sensory receptors in muscles generally constitue the primary source of proprioceptive information, but signals arising from joint and cutaneous receptors also contribute to the awereness of limb movement [Matthews, 1988]. Indeed, skin stretch resulting from joint movements is encoded by skin mechanoreceptors, thus providing an important input to the CNS. This input is then used to interpret position and movement signals arising from other sources [Clark, 1985].

On the contrary, kinaesthetic information from muscles is not sufficient for a good contact control [Kaneko, 1991]. Therefore skin sensors have a crucial role in measuring physical parameters at the contact location.

2.2.1. Human hand mechanoreceptors[1]

There are four types of specialized mechanoreceptors (Figure 2.1) within the skin of the human hand (totally 17.000 receptors in the grasping surfaces).

They can be classified using two criteria: the size of their receptive field and their response to stimuli. The receptors with a small receptive field are called Type I units, while those with large fields are called Type II. Units that respond to static stimuli are named SA (i.e. Slow Adapting), while those with no static response are denoted FA or RA (i.e. Fast or Rapidly Adapting) [Johannson and Vallbo, 1979].

These four classes of tactile mechanoreceptors provide information about the objects contacting the skin. Several studies examined the spatial and temporal resolution of the hand skin, providing measures of spatial acuity [Darian-Smith, 1984].

[1]This work has been partly published by the author (*M. T. Francomano, D. Accoto, and E. Guglielmelli, "Artificial Sense of Slip–A Review", IEEE Sensors Journal, 2013, DOI:10.1109/JSEN.2013.2252890*; paper n. 4 of *List of Publications*).

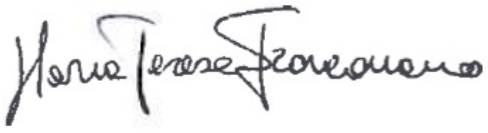

When a smooth, flat surface is moved on the skin or when the finger scans a surface for discriminating a dot or a bar on that surface, the threshold height for detecting such feature is only 0.1 um [Darian-Smith, 1984]. The accuracy with which a point of stimulation can be localized on the fingertip is 0.15 mm [Darian-Smith, 1984].

The threshold for detecting a vibratory stimulus applied to the hand depends on a number of factors, including the *locus* of stimulation, the size of the stimulated area, the duration of the stimulus, and the frequency of vibration. The sensitivity to vibration is highest around 250 Hz, when the amplitude of the smallest vibration that can be detected is less than 1um.

Johnson and Phillips have shown that normal subjects are able to distinguish between one and two 0.5 mm diameter points when there is no gap separating them [Darian-Smith, 1984]. Similarly, subjects are capable to identify whether a gap is present between two indenting edges when the two edges are separated by only 0.8-0.9 mm.

Table 2.1 reports the main features, in terms of resolution, of the human hand cutaneous receptors.

Property	**Resolution**
Surface texture irregularities	0.1um
Skin displacement	11.2um
Force discrimination	0.06 N
Transient temperature variations	0.02-0.05°C

Table 2.1: Main features of hand mechanoreceptors (from [Jones, 1997]).

The detected parameters by the four types of mechanoreceptors include skin stretch, skin curvature, vibration, and muscle force and length (Table 2.2).

Signals from FA receptors indicate the earliest stage of slip [Srinivasan, 1990], and are responsible for a reflexive and subconscious increase in the grasping force in order to prevent further slipping (see section 2.2.2).

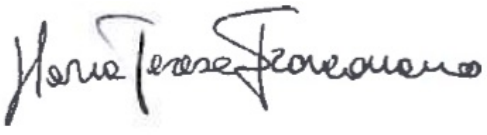

Signals from FAII endings detect when the contact between the fingers and the objects starts and ends. Finally, signals from SAI and SAII receptors signal pressure and skin stretch, respectively.

There are also other free nerve endings in the fingertip skin, which respond to local mechanical deformation. Some of them are sensitive to thermal stimuli and pain (Figure 2.1).

Mechanoreceptor type	**Field Diameter**	**Spatial density on the fingertip**	**Frequency range**	**Detected parameter**
Meissner (FAI)	3-4 mm	1500 cm-2	10-60 Hz	Skin stretch
Pacinian (FAII)	> 20 mm	75 cm-2	50-1000 Hz	Vibration
Merkel (SAI)	3-4 mm	750 cm-2	0-30 Hz	Compressive stress
Ruffini (SAII)	> 10 mm	75 cm-2	0-15 Hz	Skin stretch direction

Table 2.2: Schematic of mechanoreceptors types and related features.

In particular, thermal sensation depends on two different kinds of receptors, warm and cool receptors, whose distribution varies over the surface of the hand, with cold receptors being more numerous than warm receptors.

Both types of thermoreceptor are insensitive to mechanical stimuli but may react to chemical agents (e.g. methanol).

The above mentioned overview explains how human tactile experience emerges from a variety of sensors, able to detect a number of different physical parameters [Weinstein, 1969].

Mechanoreceptors responses are strongly nonlinear and time varying: sensitivity varies greatly with stimulus size, shape and duration.

In general, human sensing and motor control bandwidths range from a few Hz to thousands Hz. The velocity of signals transmission through the nerve is usually less than 60m/s. The fastest reflexes show latencies of at least 20-30 ms.

The fast adaptation of forces during grasping appear, therefore, to rely on anticipatory or feedforward controls, using open loop signals from the CNS that

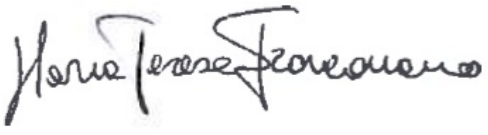

are very accurately tailored to task requirements (section 2.2.2.2, Figure 2.3) [Johansson and Westling, 1988].

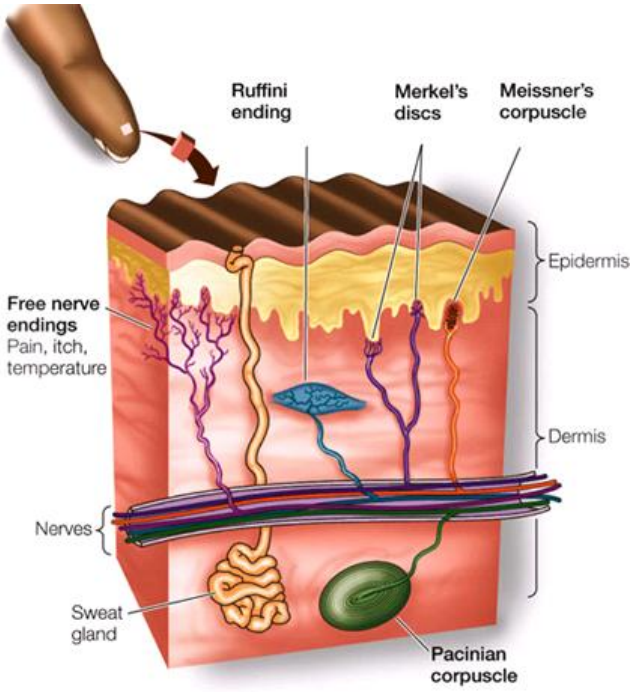

Figure 2.1: Skin mechanoreceptors [Sadava, 2007].

2.2.2. Slip perception[2]

2.2.2.1. Basic definitions

The contact between two bodies, say a finger pad (P) and an object (O), occurs over small surfaces, sometimes approximated to points, placed over an ideal contact surface, S.

To avoid interpenetration or detachment, any couple of coincident points $(p, q) \in S$, with $p \in P$, $q \in O$, must move with the same speed in the direction perpendicular to S.

[2] This work has been partly published by the author (*M. T. Francomano, D. Accoto, and E. Guglielmelli, "Artificial Sense of Slip–A Review", IEEE Sensors Journal, 2013, DOI:10.1109/JSEN.2013.2252890*; paper n. 4 of *List of Publications*).

Maria Teresa Francomano

Slip occurs if the two points have different tangential velocities. *Incipient* (or *micro*) *slip* is a relative displacement occurring in a narrow region of *S*, while *total* (or *macro*) *slip* involves any point of *S*.

These definitions imply that *incipient* and *total slips* are temporally contiguous phenomena, with *incipient slip* preceding *total slip*.

Let's consider the interaction forces at the contact surface, as schematized in Figure 2.2. Here, two fingers hold an object with mass M. Limiting the analysis to the vertical direction, a stable grip requires the compression forces to be regulated so that $F_{t_1} + F_{t_2} = Ma$. Of course, according to Coulomb's friction model, $F_{t_k} \leq \mu_s F_{n_k}$ (k=1, 2), where μ_s is the (static) friction coefficient.

The simplest strategy to prevent object slipping consists in regulating the normal component of the grip force (F_n) to its least effective value. Indeed, slip events may occur if at least one of the following conditions is verified: *i)* the normal grip force is insufficient, as it may happen during its gradual application starting from a no-load condition or if object properties (e.g., mass) are wrongly estimated; *ii)* when the tangential force, which should be counterbalanced, is higher than expected or quickly increasing (e.g., due to an unexpected perturbation, such as a collision); or *iii)* the friction coefficient becomes too low, as in the case of wet and slippery surfaces.

A direct measurement of slip is therefore useful for regulating handling and grasping forces.

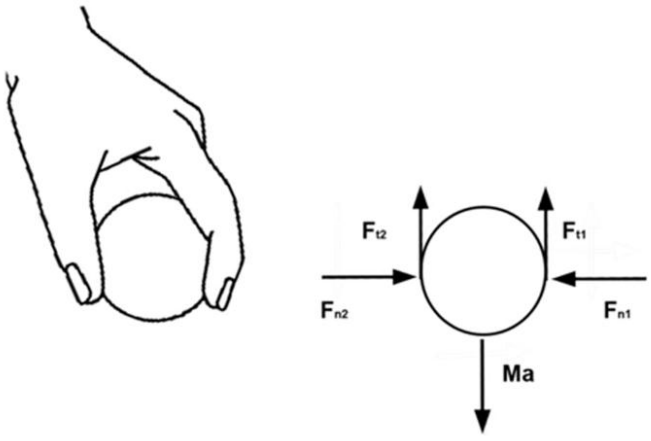

Figure 2.2: Grasping forces during weight lifting.

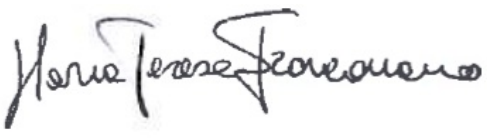

2.2.2.2. Human slip sense

The inner physiological mechanisms of what can be referred to as "slip sense" are still object of investigation and different research paths have been explored during the years.

For example, some studies put emphasis on the biomechanical behavior of the hand during manipulation [Dandekar, 2003; Maeno, 1998; Phillips, 1981].

As mentioned, mechanoreceptors mediate the response to mechanical stimuli [Johannson and Vallbo, 1979] (Table 2.2) and provide information about friction [Cadoret 1996] and interaction forces [Johansson and Westling, 1984]. Friction is influenced by several tribological factors, including sweat secretion and contact occlusion [Pasumarty, 2011].

Each mechanoreceptor (Table 2.2) encodes the spatiotemporal tactile information as spikes of action potentials, i.e. voltage pulses generated when the stimulus overcomes a threshold. Examples of mechanoreceptors recordings are reported in [Johansson and Birznieks, 2004] and [Johansson and Flanagan, 2009].

Multiple parallel pathways are used to process and transform somatosensory information before it reaches the CNS. Studies dated back to the 1920s [Adrian, 1928] report that the relative timing of the first impulses elicited in individual units in response to external stimuli are fundamental to the rapid encoding and transfer of tactile information (e.g. direction of applied force and shape of the object surface) [Johansson and Birznieks, 2004].

Another crucial issue is related to the decoding of such information. According to the *coincidence detection hypothesis* [Johansson and Flanagan, 2009] central neurons preferentially respond when receiving synchronous inputs from different sources. Once the information is decoded, motor outputs, corresponding to corrective responses, are elaborated according to strategies resembling finite-state control algorithms, i.e. based on basic logic rules (e.g., AND, IF-THEN) [Johansson and Flanagan, 2009].

The capability of perceiving *incipient slip* is important for the stability of manipulation tasks [Westling and Johansson, 1987].

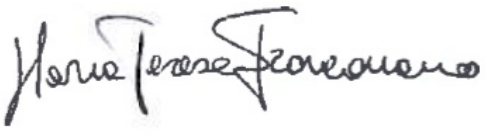

The loads over the contact area on the finger pad are not uniform, being higher at the center and lower at the boundary. Therefore, *incipient slip* starts near the edge of the contact area. It can be easily detected if the surface is characterized by a regular and homogeneous texture (e.g. dots), generating detectable skin vibrations [Srinivasan, 1990].

There are evidences that slip is mainly detected by FA receptors, the mechanoreceptors most sensitive to dynamic events (Table 2.2). The responses of FAII afferent receptors to initial contact area the most important in encoding the intensity of friction forces.

Information about slip direction comes from FAI and from "slow acting" receptors (SAI and SAII).

Epidermal ridges enhance the tactile spatial acuity by transmitting magnified signals from skin surface to the mechanoreceptors [Maeno, 1998].

Healthy people adapt forces on the basis of the frictional conditions. The response to external stimuli is generally affected by an accumulation of delays related to *i)* stimulus transduction by receptors, *ii)* neuronal conduction from the periphery to the central processing unit, *iii)* elaboration of the response, and *iv)* muscle activation.

The sensorimotor system reacts faster to unexpected sensory events, such as object slip, during fine manipulation.

This improvement in terms of reaction times is evidently not attributable to an improved performance of sensorimotor or effector mechanisms.

Rather, stimuli from mechanoreceptors are managed by the central nervous system to control manual tasks mainly by means of predictive strategies based on (forward) internal models [Flanagan, 2001; Flanagan, 2006] (Figure 2.3). Visual cues about the shape of the object and/or sensorimotor memory of previous, expectedly similar, manipulation experiences can provide the information required to elaborate predictions. A mismatch between predicted and actual sensory information triggers corrective actions in less than 100 ms [Dahiya, 2010; Flanagan, 1993].

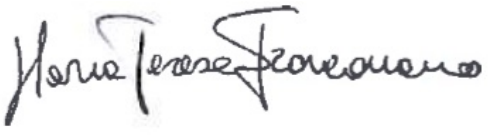

Repeated interactions (e.g. grasping attempts) become necessary in case of misleading cues, or when manipulated objects have unusual properties affecting the interaction, such as extremely slippery surface, as in the case of a wet bar soap [Flanagan, 2000] (Chapter 6).

Some brain imaging studies identified the cerebral areas involved in grasp and manipulation control. Evidences suggest that the right posterior parietal cortex, as well as the bilateral cerebellum, play important roles, possibly storing the forward internal models [Hermsdorfer, 2003].

However, force adaptation (i.e. basic grip/load force coupling) seems to be robust to a variety of cerebral lesions, including cerebellar ones [Hermsdorfer, 2003], which suggests that the central neural architecture supporting these skills is still not exactly identified.

What is demonstrated is that humans control grasp forces almost optimally, with forces just 10–40% above the minimum value required to prevent slip [Johansson and Flanagan, 2008].

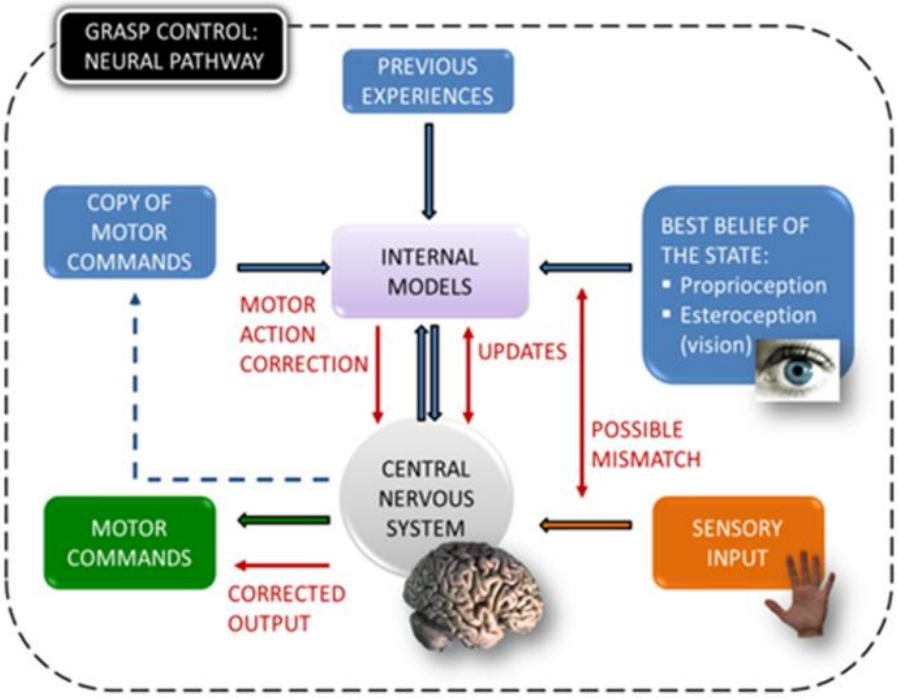

Figure 2.3: Neural pathway of grasp stability control.

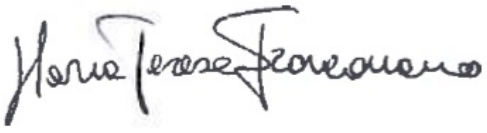

2.3. Hand Prosthetic Devices: State of the Art

The loss of the biological hand is a major source of disability. It can be due to trauma (i.e. accidents) and cancer, but also to diseases (e.g. peripheral artery diseases, diabetes) or genetic imperfections.

It has been estimated that there are about 100.000 traumatic upper limb amputees in Europe, with about 2.000 new cases each year [Banzi, 2005; UK Prosthetic Services, 2006]. In the USA the number of amputations is around 140.000 annually [Business Wire, 2007].

Overall, 67% of upper limb amputees are male. Frequently amputations occur during the productive working years:in the 60% of cases they involve subjects with an age between 16 and 54 years [Clement, 2011].

For amputees *prostheses* represent a considerable alternative to a hand transplant, which involves critical drawbacks. For example, a donor limb has to match the recipient's in terms of size and shape, meaning that suitable donor limbs are rare. The recipient's reliance on long-term immunosuppression and the complexity of transplant surgery are likely to limit transplantation as the major reconstructive option for amputees. Therefore the more widespread option for an upper limb amputee is to opt for an artificial replacement.

The concept of prosthesis was already known to ancient Egyptians [Thurston, 2007]. The first upper limb extremity prostheses were passive aesthetic hands, which simply provided a physical entity, resembling in appearance the biological counterpart.

If traditional prostheses are passive artificial limbs without any intelligence, advanced devices aim at achieving performance comparable to those of the biological counterparts [Belter and Dollar, 2011]. Nevertheless, as mentioned, the human hand is by nature so complex that replicating its function using a bionic device is a significant challenge. The introduction of robotics in the domain of prosthetics provides considerable opportunities to improve functionality.

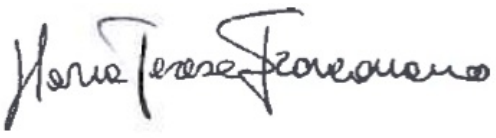

Over the last few decades there have been great research efforts in this field. However, there is still a large gap between current state of the art and ideal devices, which should be highly functional, durable, cosmetic, and inexpensive.

The development of robotic upper limb prostheses started in the 1950's [Thurston, 2007]. Nowadays these devices are mainly governed using a *i)* myoelectric control; *ii)* body powered cable control; and *iii)* switch control.

Myoelectric prosthetic hands are detailed in section 2.3.1. Body-powered prostheses are typically cable-driven via a harness strapped around the contralateral shoulder that runs to the terminal device. The cable control system uses the motion and forces generated primarily by shoulder flexion and abduction for actuating and controlling the elbow joint and the artificial limb [Jones, 1997].

Wrist pronation and supination is usually provided by a simple friction joint rotated by the opposite hand into the correct orientation as needed by the artificial hand to grasp an object. Palmar prehension and precision handling are both possible with this type of body-powered prosthesis, and although movements take longer to execute than with the normal hand, their pattern of usage is similar to that observed in normal hands [Jones, 1997]].

One of the main disadvantages of body-powered systems is that the harness often necessitates extreme body movements, such as trunk rotation to turn a heavy object.

Forces that operate on the hand are in turn transmitted through the cable to the body. This force information is surprisingly accurate, as subjects are able to duplicate precisely small grasp forces. This basic sensory information can be augmented by providing subjects with additional information by means of, e.g., electro cutaneous feedback.

On the other hand, switch control systems use the movements and forces generated by fine body movements to actuate and control electromechanical components and require less force and movement than a cable-operated prosthesis. Various switches are available for activating the terminal device,

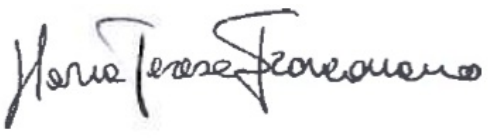

including pull, rocker, push-button, and toggle, the use of which depends on the particular residual capacities of the amputee.

A switch-control is generally used in situations where there is a limited range of motion and force available for a cable control system and the EMG potentials (section 2.3.1.) are not adequate or appropriate for myoelectric control [Jones, 1997].

Commercially available prostheses and research prototypes gradually improved since their introduction into the market, with the aim of restoring also the capability to sense and explore the surrounding world. Currently available bionic hands are able to produce better functional grips, including key, power, precision, index point and thumb park. This confers far wider applications than previously achievable.

2.3.1. Commercial devices

The leading industrial players of upper limb prosthetic devices are Ottobock (Germany), LTI (USA), Motion Control (USA), and RSL-Steeper (UK) [Clement, 2011].

Myoelectric prostheses are technologically the most advanced (Figure 2.4). They are user-controlled: the contraction of specific muscles in the residual limb triggers movements through EMG signals. Alternatively, neural motor signals can be diverted for triggering the activation of the prosthesis. In this way, it is possible to easily control but a limited set of movements, such as hand opening and closing or wrist rotation [Zecca, 2002]. Techniques such as electrical pattern recognition can be used to activate whole muscle groups needed for certain movements. Nevertheless learning how to use a myoelectrically controlled prosthesis can be time consuming and difficult and there must be enough electrical activity in the limb stump for them to properly work.

In 1964 the first myoelectric prosthesis was manufactured in the United Kingdom (Russian Arm, Hanger Limb Factory) based on a Russian design [B. Popov, 1993].

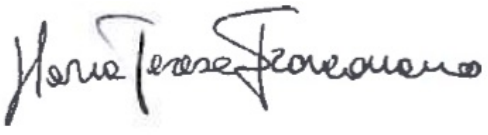

After that, the Elektrohand 2000 was developed in 1988 by Otto Bock (Germany). This myoelectric hand prosthesis was especially developed for children from 18 months to 13 years old (Otto Bock, www.ottobock.com).

With a 300 mm/s opening/closing speed and enhanced EMG signal processing, the myoelectric Sensorhand from Otto Bock (1997) has excellent speed and responsiveness (Otto Bock, www.ottobock.com). The *autograsp* feature keeps held objects from slipping by monitoring and changing grip force as needed.

Another type of myoelectric controlled hand prosthesis is the iLimb Hand, developed in 2007 by Touch Bionics (Touch Bionics, www.touchbionics.com). The control system monitors each finger in order to avoid crushing objects. However, although comprising five independent fingers, the hand is basically controlled like traditional hands, i.e. through a two-electrode superficial EMG interface. Moreover the hand sensory system is limited and not employable for delivering sensory-feedback to the amputees.

Finally, the RIC Neurocontrolled Bionic Arm is an example of a new generation bionic prosthesis [Clement, 2011] potentially replacing the entire arm.

The *targeted motor reinnervation* technique has been often exploited for increasing the accuracy of myoelectrically controlled prostheses.

In this technique the nerves that once supplied the amputated limb muscles are surgically anastomosed into the remaining muscles of the amputation stump to create independently controlled nerve-muscles units. The reinnervated muscles act as biological amplifiers of motor commands in the amputated nerves and the surface electromyogram can be used to enhance control of a robotic arm. This technique has shown promising results with the ability to achieve intuitive control of multiple functions in a bionic hand.

An alternative system being developed to increase accuracy of myoelectric prostheses involves the implantation of bipolar differential EMG electrodes within the muscles to create a system capable of reading intra muscular EMG signals that increase the number of control sources available for prosthesis control.

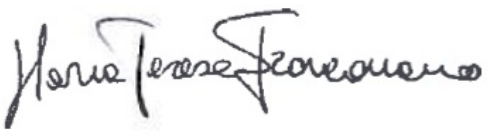

Somyography is an alternative method of limb control under development. It utilizes ultrasounds to measure the size change of contracting muscles in the stump. This technique shows potential to increase the accuracy of movements and force calculations compared to present day myoelectrical systems.

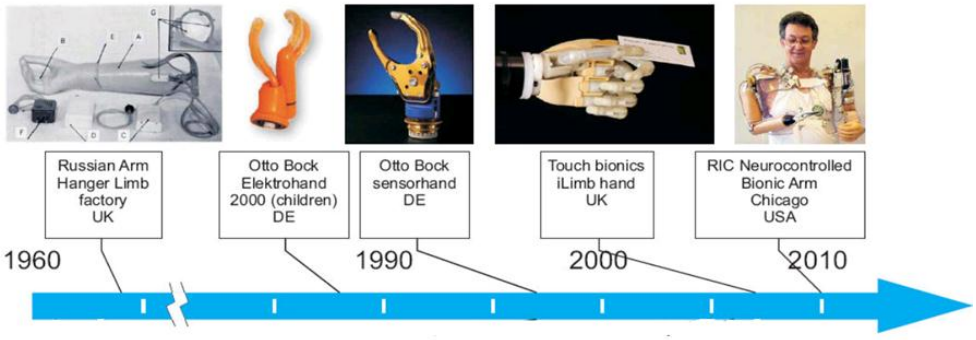

Figure 2.4: Timeline of the main progresses in the upper limb prosthetic field [Butter, 2008].

2.3.2. Research prototypes

Several examples of research prototypes are reported in literature (Figure 2.5). Although all prototypes differ from each other, they all aim at being low power and lightweight, while still allowing a number of prehension patterns useful in activities of daily living.

Some of these requirements have been met by improving mechanical components (e.g. implementing different underactuated mechanisms and clutching systems [Clement, 2011]). However, in most cases the sensory system is inexistent or limited to low-level grip control.

In 1995 the MARCUS [Kyberd, 1993; Kyberd, 2001] three fingered sensorized prosthesis, controlled by a hierarchical controller [Kyberd, 1995], was presented. The sensory system represented an innovation with respect to the state-of-the-art since proprioceptive and exteroceptive sensors were integrated in the prototype, both on the fingertips and on the palm.

Researchers at the University of Southampton [Light, 2000; Light, 2002] developed an ultra-light limb (400g) that mimics movements in real hands with 6 sets of motors and gears so that each of the five fingers can move independently.

Maria Teresa Francomano

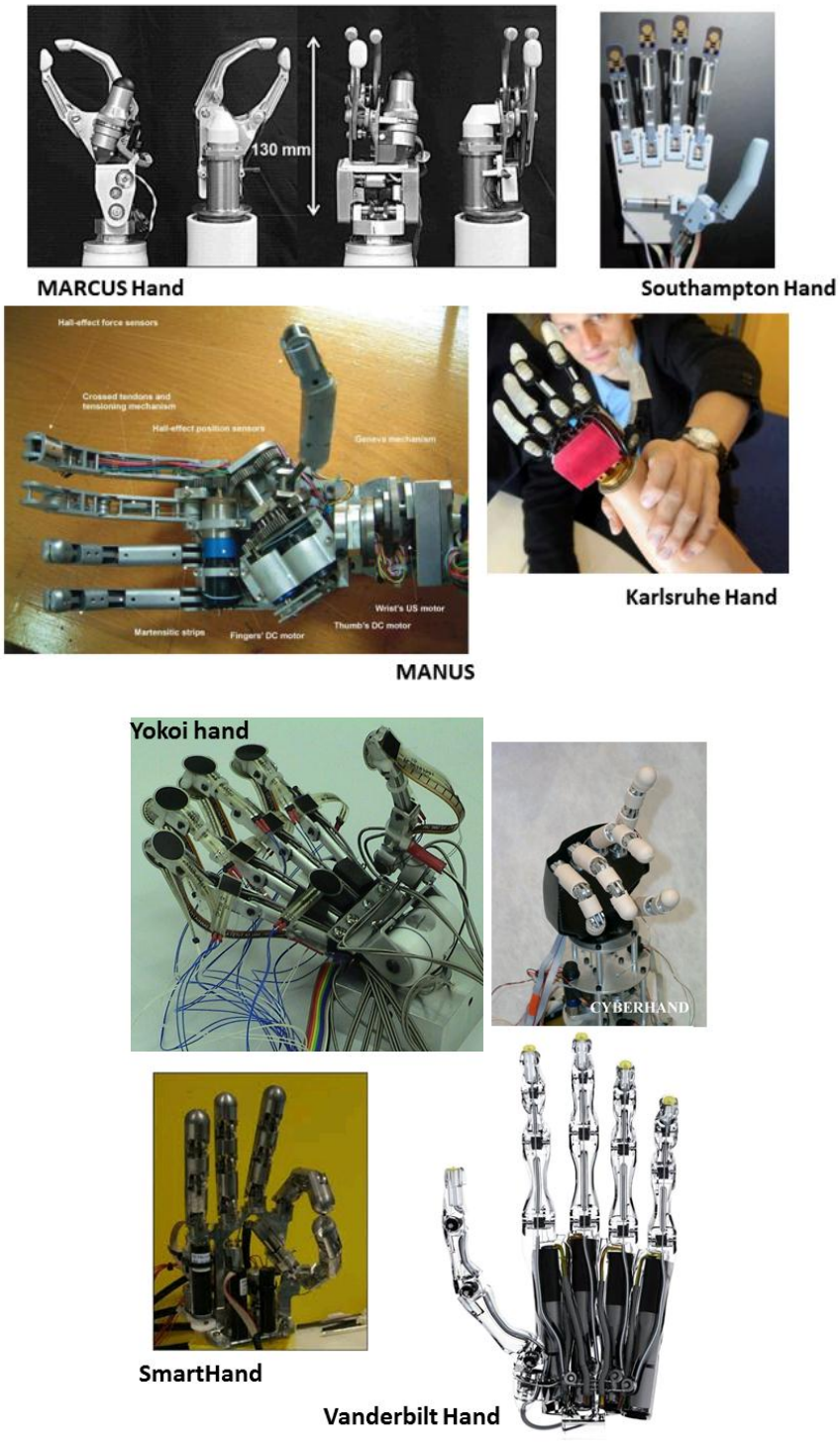

Figure 2.5: Research prototypes of prosthetic hands.

The MANUS project [Pons, 2004] proposed a prosthesis with ten joints, three of which independently driven. From a sensory point of view, force and position sensors are distributed in the hand, which is controlled by means of a hierarchical control architecture

Research at the Forschungszentrum Karlsruhe [Pylatiuk, 2004] focused on the development of a prosthetic hand with a high number of grasping patterns and with a low weight and good cosmetic appearance.

The SmartHand prosthesis [Cipriani, 2009], developed at Scuola Superiore Sant'Anna (SSSA), is an innovative transradial hand, including actuators, control system and 40 sensors.

Other prosthetic hand platforms include the Cyberhand [Carrozza, 2006; Cipriani, 2008], the Yokoi hand [Ishikawa, 2000], and the Vanderbilt University prototypes [Fite, 2008; Wiste, 2009].

2.4. Discussion

Human hand's sensory and motor capacities have been widely investigated.

Such studies have provided a wealth of information about the human hand, and have given design inputs for the development of upper limb prostheses emulating selected featured of the human hand.

Current commercial prosthetic hands are structurally simple. Consequently they are reliable but the available functionalities are limited and far from attaining the requirements. In order to increase users' acceptance, more improvements are expected, starting from the possibility of accomplishing dexterous tasks, by controlling the hand in a as natutal as possible way.

Therefore the main challenges on which current and future research activities should focus on (Figure 2.6) include:

- *Technological improvements,* for example, for *i)* incorporating as many degrees of freedom as the natural hand, using smart actuators and novel kinematic design; *ii)* employing lightweight materials for mechanics; *iii)* using compact, strong and energy efficient actuators; and *iv)* developing energy storage/generation/transfer devices for a longer operability.

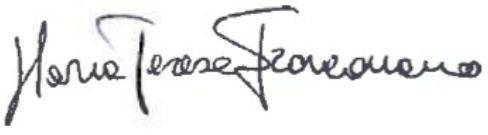

- *Physical connection to the human body*. Invasive connection to the PNS and non-invasive connection to the CNS are the most implemented solutions. In the future it is expected to have a less invasive and more effective connection to the CNS (Chapter 3).
- *Human control of the prosthesis*. New control systems are necessary for enabling the user to make effective use of the prosthetic device (adaptive control).

  A possible solution to reduce the cognitive burden inflicted to the user in controlling a limb with several DOFs is to split the control into a higher level (i.e. user intention detection for "task control"), demanded to the human nervous system, and a lower one (e.g. for coordination or reflexive/subconscious actions) to be handled at the peripheral (device) level.
- *External feedback to the user.* Sensory feedback is more important in upper extremity prosthetics than in lower limbs prostheses, because hands often are required to explore and manipulate unknown objects. The use of a wide variety of sensors could allow the perception of objects properties as well as static and dynamic conditions during contact. Moreover, sensory feedback would enable decoupling the basic control loops, executed at device level, from higher cognitive functions (i.e. CNS control of the prosthesis).

  Both for aesthetic and technological reasons, there is a strong need for elastic, human like sensorized skin (artificial skin).

  Usually prosthetic devices are covered by a silicone glove enhancing their cosmetic appearance and thus improving their acceptability by the user. Coverings have been developed, which can closely resemble the natural skin. However the durability of the coverings requires diligent care and adds further costs to the prosthesis. Nonetheless, the most important improvement to address is the sensorization of such coverings.

Furthermore, several other factors should be taken into account:

- Power consumption: for allowing the use of the prosthesis for a whole day without battery recharge;

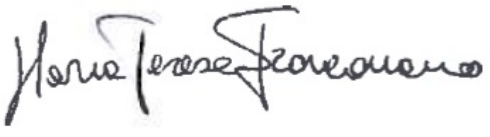

- Modular design: for easily manufacturing and maintenance purposes;
- Reliability and durability.

The above mentioned open issues represent the reasons why most amputees do not customarily use active devices, often refuging to a purely cosmetic prosthesis [Atkins, 1996; Carrozza, 2002].

On the other hand, the same challenges, which promise higher expectations of independence, are the driving forces of current research activities.

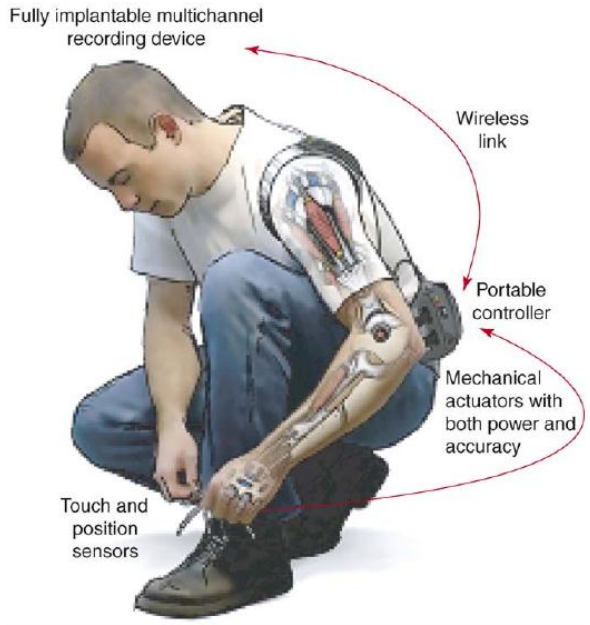

Figure 2.6: Main challenges of upper limb prostheses [Lebedev and Nicolelis, 2006].

2.5. Conclusion

Human hand sensory and motor capabilities provide an existence proof that a wide variety of high dexterity manipulation tasks can be accomplished by a single system.

Over the last few decades there have been great strides in the development of novel prosthetic hands and terminal devices that take advantage of the latest technological advances, moving towards more dexterous and realistic hand devices.

Nowadays, although the characteristic performance of some prosthetic devices are impressive, there is still a large gap between current state-of-the-art and

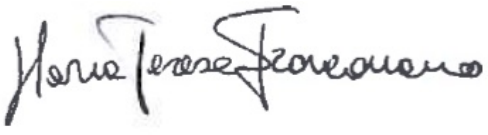

devices that have the ideal combination of being highly functional, durable, cosmetic, and inexpensive.

The ultimate goal is to achieve a "Biomechatonic design", which would need the integration of the prostheses with the CNS, so that the artificial limb could be controlled and perceived as if it were the natural hand, without any need for training or adaptation.

The lack of success in imparting a *sense of touch* to myoelectric hands is a major issue in current research on prosthetic devices. A number of groups have developed different systems for providing tactile and proprioceptive feedback, but so far no system has been accepted clinically.

An additional problem is the issue of a reliable *multichannel communication link to peripheral nerves*. Although there has been considerable research on surgically implanted telemetry systems, the problems associated with chronic attachment of electrodes to residual muscles and nerves have not been solved.

The two mentioned challenges, i.e. the possibility of naturally controlling the hand, and of restoring the tactile feedback usually provided by the skin, are the focus of this PhD thesis and they will be addressed in the following Chapters.

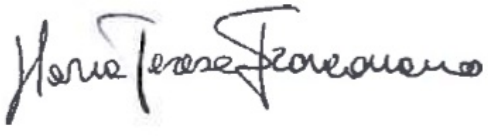

Bibliography

[Adrian, 1928] Adrian, E. D. The Basis of Sensation (Norton, New York, 1928).

[Atkins, 1996] D. J. Atkins, et al. "Epidemiologic overview of individuals with upper limb loss and their reported research priorities," JPO Vol. 8, no. 1, 1996.

[Balter and Dollar, 2011] J. T. Belter and A. M. Dollar, "Performance Characteristics of Anthropomorphic Prosthetic Hands", in Proc. IEEE International Conference on Rehabilitation Robotics, Zurich, Switzerland, June 29-July 1, 2011.

[Banzi, 2005] Banzi, et al. "Analisi delle strategie di controllo per protesi di arto superiore in pazienti con amputazioni transomerali o disarticolati di spalla", Biosys, ANIPLA, 2005, pp. 290-300.

[Business Wire, 2007] BusinessWire. Growing Consumer Base of Amputees Drives U.S. Lower Extremity Prosthetics Market: 2007 Sept 26; Available from: http://www.allbusiness.com/medicine-health/diseases-disorders-endocrine/5281879-1.html.

[Butter, 2008] Butter M., et al.,"Robotics for Healthcare-Final Report", 2008.

[Cadoret 1996] G. Cadoret, and A. M. Smith, "Friction, not texture, dictates grip forces during object manipulation", J. Neurophysiol., vol. 75(5), pp. 1963–1969, May 1996.

[Carrozza, 2002] M. C. Carrozza, et al. "The development of a novel prosthetic hand -ongoing research and preliminary results," IEEE/ASME Trans Mech Vol. 7, No 2, pp.108-114, 2002.

[Carrozza, 2006] M.C. Carrozza, G. Cappiello, S. Micera, B.B. Edin, L. Beccai, C. Cipriani, "Design of a cybernetic hand for perception and action", Biological Cybernetics, vol. 95, no. 6, pp. 629-644, Dec. 2006.

[Charles and Williams, 1989] Charles, S., and Williams, R. (1989). Measurement of hand dynamics in a microsurgery environment: Preliminary data in the design of a bimanual telemicro-operation test bed. Proc. of the NASA Conf. on Space Telerobotics, 109-118.

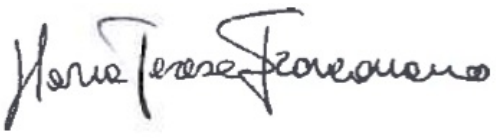

[Cipriani, 2008] Cipriani C, Zaccone F, Micera S, Carrozza MC, On the shared control of an EMG controlled prosthetic hand: analysis of user-prosthesis interaction, IEEE Trans Robot 2008;24(1):170-184.

[Cipriani, 2009] C. Cipriani, M. Controzzi, and M. C. Carrozza, "Objectives, Criteria and Methods for the Design of the SmartHand Transradial Prosthesis," Robotica, available online doi:10.1017/S0263574709990750, 2009.

[Clark, 1985] Clark, F. J., Burgess, R. C., Chapin, J. W., and Lipscomb, W. T. (1985). Role of intramuscular receptors in the awareness of limb position. Journal od Neurophysiology, 53, 1529-1540.

[Clement, 2011] R. G. E. Clement, K. E. Bugler, and C.W. Oliver, "Bionic prosthetic hands: a review of present technology and future aspirations", The Surgeon, vol. 9(6), pp. 336–340, Dec. 2011.

[Dahiya, 2010] R. S. Dahiya, G. Metta, M. Valle, and G. Sandini, "Tactile Sensing—from Humans to Humanoids", IEEE Trans. Robot., vol. 26(1), pp. 1-20, Feb. 2010.

[Dandekar, 2003] K. Dandekar, B. I. Raju, and M. A. Srinivasan, "3-D finite-element models of human and monkey fingertips to investigate the mechanics of tactile sensing", J. Biomech. Eng., vol. 125(5), pp. 682–691, 2003.

[Darian-Smith, 1984] The sense of touch: Performance and peripheral neural processes. In I. Darian-Smith (Ed.), Handbook of physiology: the nervous system. Sensory processes, vol. III, pp. 739-788. Bethesda, MD.: American Physiological Society.

[Flanagan, 1993] J. R. Flanagan, and A. M. Wing, "Modulation of grip force with load force during point-to-point arm movements", Exp Brain Res., vol. 95, pp. 131–143, July 1993.

[Flanagan, 2000] J. R. Flanagan, and M. A. Beltzner, "Independence of perceptual and sensorimotor predictions in the size-weight illusion", Nat. Neurosci., vol. 3, pp. 737-741, July 2000.

[Flanagan, 2001] J. R. Flanagan, D. M. Wolpert, and R. S. Johansson, "Sensorimotor prediction and memory in object manipulation", Canadian Journal of Experimental Psychology, vol. 55(2), pp. 89-97, June 2001.

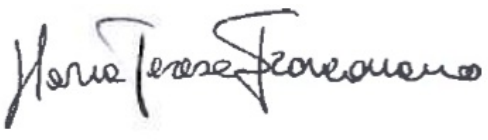

[Flanagan, 2006] J. R. Flanagan, M. C. Bowman, and R. S. Johansson, "Control strategies in object manipulation tasks", Curr. Opin. Neurobiol., vol. 16(6), pp. 650-659, Dec. 2006.

[Fite, 2008] Fite KB, Withrow TJ, Shen X, Wait KW, Mitchell JE, Goldfarb M. A Gas-Actuated Anthropomorphic Prosthesis for Transhumeral Amputees. IEEE Trans Robot 2008; 24(1):159-169.

[Hermsdorfer, 2003] J. Hermsdorfer, E. Hagl, D. A. Nowak, and C. Marquardt, "Grip force control during object manipulation in cerebral stroke", Neurophysiol Clin., vol. 114(5), pp. 915–929, May 2003.

[Ishikawa, 2000] Ishikawa Y, Yu W, Yokoi H, Kakazu Y. Development of robotic hands with an adjustable power transmitting mechanism. In Intelligent Engineering Systems Through Neural Networks, vol. 10, C. H. Dagli, et al., Ed. New York: ASME, pp. 631-636, 2000.

[Johansson and Birznieks, 2004] R. S. Johansson and I. Birznieks, "First spikes in ensembles of human tactile afferents code complex spatial fingertip events", Nat. Neurosci., vol.2(7), pp. 171-177, 2004.

[Johansson and Flanagan, 2008] R. S. Johansson, and J. R. Flanagan, "Tactile sensory control of object manipulation in humans", in The senses, a comprehensive reference: Somatosensation Vol 6, edited by E. Gardner and J. H Kaas. Amsterdam: Elsevier, 2008, pp. 67-86.

[Johansson and Flanagan, 2009] R. S. Johansson and J. R. Flanagan, "Coding and use of tactile signals from the fingertips in object manipulation tasks", Nat. Rev. Neurosci., vol. 10, pp. 345-359, 2009.

[Johansson and LaMotte, 1983] R. S. Johansoon and R. H. La Motte. Tactile detection thresholds for a single asperity on an otherwise smooth surface. Somatosensory Research. 1(1):21-31, 1983.

[Johannson and Vallbo, 1979] R. S. Johannson, and A. B. Vallbo, "Tactile sensibility in the human hand: relative and absolute densities of four types of mechanoreceptive units in glabrous skin", J Physiol., vol. 286, pp. 283–300, Jan. 1979

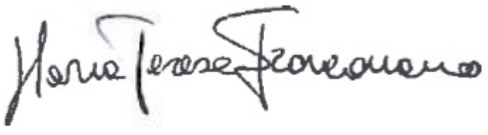

[Johansson and Westling, 1984] R. S. Johansson, and G. Westling, "Roles of glabrous skin receptors and sensorimotor memory in automatic control of precision grip when lifting rougher or more slippery objects", Exp Brain Res., vol. 56, pp. 550–564, Oct. 1984.

[Johansson and Westling, 1988] R. S. Johansson, and G. Westling. Signals in tactile afferents from the fingers eliciting adaptive motor responses during precision grip. Experimental Brain Researche. 71:72-86, 1988.

[Jones, 1997] Jones L., Dextrous hands: human, prosthetic, and robotic, Presence (Camb). 1997 Feb;6(1):29-56.

[Kyberd, 1993] P. J. Kyberd et al., "The MARCUS intelligent hand prosthesis," in Rehabilitation Technology: Strategies for the European Union, E. Ballabio et al., Eds. Amsterdam IOS press, 1993, pp. 98-102.

[Kyberd, 1995] Kyberd PJ, Holland OE, Chappel PH, Smith S, Tregdigo R, Bagwell PJ, Snaith M. Marcus: A two degree of freedom hand prosthesis with hierarchical grip control. IEEE Trans Rehabil Eng 1995;3(1):70-76.

[Kaneko, 1991] M. Kaneko, M. Wada, H. Maekawa, and K. Tanie. A new consideration on tendon-tension control system of robotic hands. In Proc. 1991 IEEE International Conference on Robotics and Automation, pp. 1028-1033, Sacramento, CA, USA, 1991.

[Kyberd, 2001] P.J. Kyberd, C. Light, P. H. Chappell, J. M. Nightingale, D. Whatley and M. Evans, "The design of anthropomorphic prosthetic hands: A study of the Southampton Hand," Robotica, vol. 19, pp. 593– 600, 2001.

[Lebedev and Nicolelis,2006] Lebedev MA, Nicolelis MA. Brain-machine interfaces: past, present and future. Trends Neurosci. 2006 Sep;29(9):536-46.

[Light, 2000] C. M. Light and P. H. Chappell, "Development of a lightweight and adaptable multiple-axis hand prosthesis," Med Eng Phys, vol. 22, pp. 679–684, 2000.

[Light, 2002] Light CM, Chappell PH, Hudgins B, Engelhart K. Intelligent multifunction myoelectric control of hand prostheses. Journal of Medical Engineering & Technology 2002;26(4):39-46.

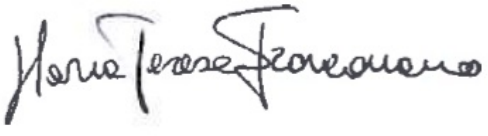

[Maeno, 1998] T. Maeno, K. Kobayashi, and N. Yamazaki, "Relationship between the structure of human finger tissue and the location of tactile receptors", Bull. JSME Int. J., vol. 41(1), pp. 94–100, 1998.

[Matthews, 1988] Matthews, P. B. C. (1988). Proprioceptors and their contribution to somatosensory mapping: Complex message require complex processing. Canadian Journal of Physiology and Pharmacology, 66, 69-74.

[Pasumarty, 2011] S. M. Pasumarty, S. A. Johnson, S. A. Watson, and M. J. Adams, "Friction of the human finger pad: influence of moisture, occlusion and velocity", Tribol. Lett., vol 44, pp. 117–137, Nov. 2011.

[Phillips, 1981] J. R. Phillips, and K. O. Johnson, "Tactile spatial resolution. III. A continuum mechanics model of skin predicting mechanoreceptors responses to bars, edges, and gratings", J Neurophysiol., vol. 46, pp. 1204–1225, 1981.

[Pons, 2004] J.L. Pons, E. Rocon, R. Ceres, D. Reynaerts, B. Saro, S. Levin and W. Van Moorleghem, "The MANUS-HAND Dextrous Robotics Upper Limb Prosthesis: Mechanical and Manipulation Aspects," Autonomous Robots, vol. 16, pp. 143-163, 2004.

[Popov, 1993] Popovic DB, Stein RB, Jovanovic KL, Dai R, Kostov A, Armstrong WW, 1993. Sensory nerve recording for closed-loop control to restore motor functions. IEEE Trans Biomed Eng 40(10):1024–31.

[Pylatiuk, 2004] C. Pylatiuk, S. Schulz, A. Kargov and G. Bretthauer, " Two Multiarticulated Hydraulic Hand Prostheses," Artificial Organs, vol. 28, no. 11, pp. 980-986, 2004.

[Sabatini, 1989] Sabatini, A. M., Bergamasco, M., and Dario, P. (1989). Force feedback-based telemanipulation for robot surgery on soft tissues. Proc. of the Annual Int. Conf. of the IEEE Engineering in Medicine and Biology Society, 3, 890-891.

[Salthouse, 1984] Salthouse, T. A. (1984). Effect of age and skill in typing. Journal of Experimental Psychology: General, 113, 345-371.

[Sadava, 2007] D. Sadava, H. C. Heller, G. H. Orians, W. K. Purves, D. M. Hillis, "Life: The Science of Biology", W. H. Freeman, 2006 - 1121 pp.

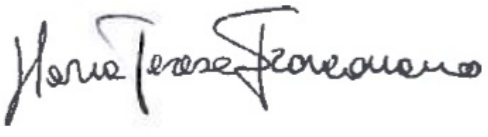

[Srinivasan, 1990] M. A. Srinivasan, J. M. Whitehouse, and R. H. LaMotte, "Tactile detection of slip: surface microgeometry and peripheral neural codes", J Neurophysiol., vol. 63(6), pp. 1323-1332, June 1990.

[Thurston, 2007] A. J. Thurston, "Paré and prosthetics: the early history of artificial limbs", ANZ J Surg, vol. 77(12), pp. 1114-1119, Dec. 2007.

[UK Prosthetic Services, 2006] UK Prosthetics Services, "Upper Limb amputations" Amputee Statistical Database for the United Kingdom : 2005/06.

[Weinstein, 1969] Weinstein S. Intensive and extensive aspects of tactile sensitivity as a function of body part, sex, and laterality. In The Skin Senses, D.R.Kenshalo, Ed. Springfield, IL: Charles C. Thomas: 195–218 (1969).

[Westling and Johansson, 1987] G. Westling, and R. S. Johansson, "Responses in glabrous skin mechanoreceptors during precision grip in humans", Exp Brain Res., vol. 66, pp. 128–140, March 1987.

[Wiste, 2009] T. E. Wiste, S. A. Dalley, T. J. Withrow, M. Goldfarb, "Design of a Multifunctional Anthropomorphic Prosthetic Hand with Extrinsic Actuation," In Proc. Intl. Conf. on Rehabilitation Robotics, Kyoto, Japan, June 23-26, 2009.

[Zecca, 2002] Zecca M, Micera S, Carrozza MC, Dario P, 2002. Control of multifunctional prosthetic hands by processing the electromyographic signal. Crit Rev Biomed Eng 30(4-6):459-85.

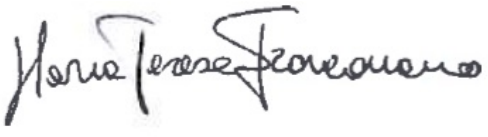

Chapter 3

Neural Interfaces

Neural interfaces for the Peripheral Nervous System (PNS), that are recognized to be less invasive than cortical ones (for an overview see: [Navarro, 2005; Micera, 2008]), are investigated for their potential of establishing a natural communication channel between the nervous system (NS) and the prosthesis, thus minimizing the cognitive burden inflicted to the subject.

Such interfaces should necessarily be able to selectively stimulate afferent channels of the PNS in order to provide a realistic sensory feedback, as needed by fine motion control (Figure 3.1).

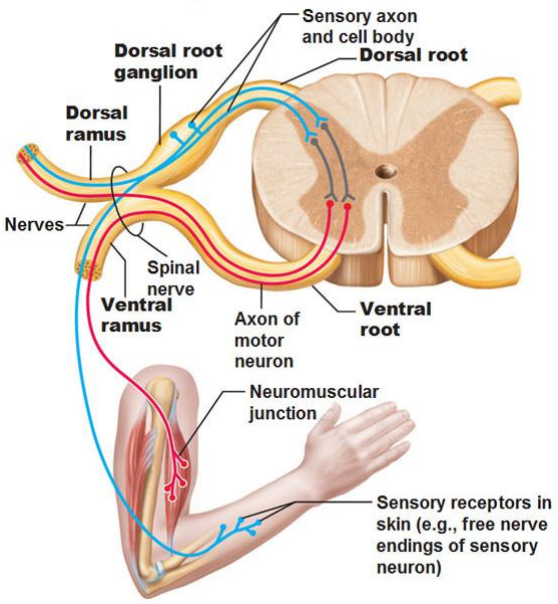

Figure 3.1: Spinal nerves of the upper limb [McKinley, 2009].

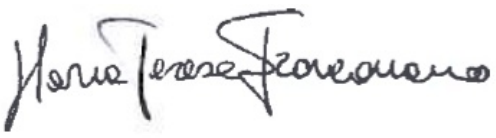

3.1. Organization of the PNS

The PNS is constituted by neurons whose cell bodies are located in the spinal cord or within spinal ganglia, while their central connections (nerve roots) and their axons extend through peripheral nerves to reach target organs.

Peripheral nerves contain several types of nerve fibers. Afferent sensory fibers can be unmyelinated or myelinated, the latter ranging from 2 to 20 mm in diameter, and terminate at the periphery either as free endings or in various specialized sensory receptors.

Efferent motor fibers originate from motoneurons in the spinal cord and end in neuromuscular junctions in skeletal muscles.

Most of the somatic peripheral nerves are mixed, providing both motor and sensory innervations to the corresponding area.

Nerve fibers, both afferent and efferent, are grouped in fascicles surrounded by connective tissue [Peters, 1991].

The peripheral nerves are folded by three sheaths (Figure 3.2): *epineurium*, *perineurium*, and *endoneurium*.

The epineurium is the outer layer, including loose connective tissue and blood vessels. The perineurium surrounds each fascicle in the nerve and it is made of inner layers of flat perineurial cells and an outer layer of collagen fibers. The endoneurium, located between nerve fibers within the fascicle, is composed of fibroblasts, collagen, reticular fibers, and extracellular matrix.

The natural actions of the body are controlled using the efferent neural signals going from the CNS to the PNS, recruiting different muscles. At the same time, the information transduced by the natural sensors (mechanoreceptors, proprioceptors, etc.) are conducted to the CNS by activation of the afferent nerve fibers.

Signals are transmitted by the corresponding axons in series of impulses or action potentials, with intensity of the signal mainly coded in impulse frequency along the peripheral axon.

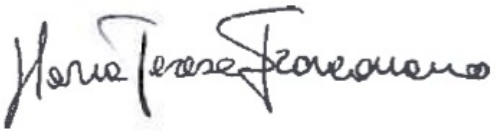

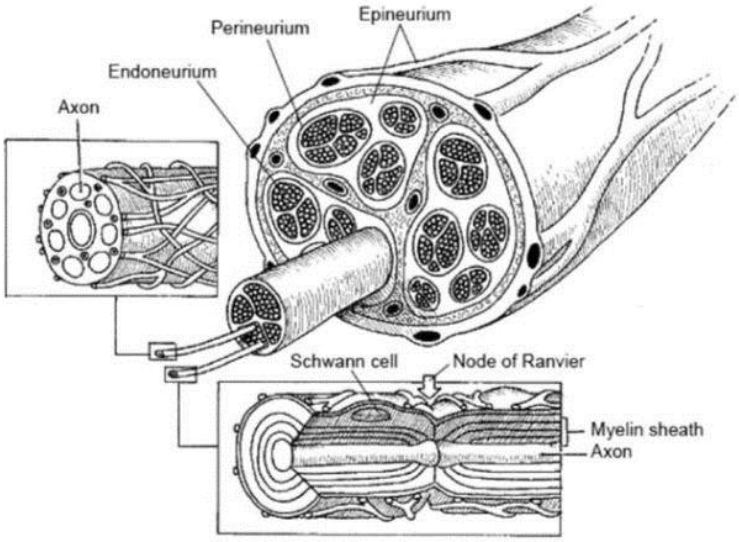

Figure 3.2: Peripheral nerve structure [McKinley, 2009].

3.2. Peripheral neural interfaces: State of the Art[3]

A number of interfaces with peripheral nerves for neuroprosthetic purposes have been developed [Navarro, 2005].

The neural interface is a bidirectional transducer, establishing a neuro-mechanical contact between the device and the tissue, for stimulating neurons as well as for recording their responses.

From a biological point of view, such interface is a foreign body, therefore it is mandatory to take into account also biocompatibility issues [Heiduschka and Thanos, 1998; Stieglitz, 2004].

There are different methods for coupling the electronic implants (i.e. neural interfaces) to the PNS, depending on the type of biological signal (chemical, mechanical, magnetic or electrical) [Navarro, 2005].

[3] This work has been partly published by the author (*D. Accoto, M. T. Francomano, A. Rainer, M. Trombetta, P. M. Rossini, E. Guglielmelli, "An implantable neural interface with electromagnetic stimulation capabilities", Medical Hypothesis, accepted, January, 2013*; paper n. 3 of *List of Publications*).

Maria Teresa Francomano

There are two basic classes of interfaces: invasive and non-invasive (Table 3.1). The latter includes surface and muscular electrodes that can record EMG signals and stimulate the underlying muscles.

Microelectrodes contacting peripheral nerves or muscles are the most common devices, although this coupling method is normally associated with some degree of invasiveness.

High selectivity and low invasiveness are usually conflicting requirements (Figure 3.3) [Navarro, 2005; Micera, 2008].

Among existing invasive interfaces to PNS, intrafascicular electrodes offer a good compromise between selectivity and invasiveness [Micera, 2008].

NON-INVASIVE INTERFACES	**INVASIVE INTERFACES**
Surface electrodes	*Muscle electrodes* (epimysial and intramuscular electrodes)
Non electrical interfaces	*Extraneural electrodes* (epineural and helicoidal electrodes; book electrodes; cuff electrodes; flat interfaces nerves electrodes; interfascicular electrodes)
	Intraneural electrodes (intrafascicular electrodes; penetrating microelectrodes; regenerative electrodes)

Table 3.1: Peripheral neural interfaces classification [Navarro, 2005].

An experiment on intrafascicular electrodes, implanted in a volunteer amputee for the bidirectional control of a cybernetic prosthesis, shows that the capability of the afferent channel to elicit tactile sensations decreases over time, while the efferent channel (for neural signals recording) is comparatively more stable [Rossini, 2010].

The reasons for this are not completely understood yet, as they may arise from a number of physiological factors, including progressive habituation of the subject and the occurrence of fibrosis around implanted electrodes [Rossini, 2010].

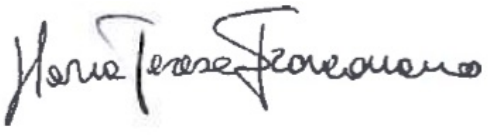

A sound strategy for improving the quality of the neuron-electrode interface resorts to advanced electrodes coatings. For example, it has been recently demonstrated that carbon nanotubes or conductive polymers coatings over sharped gold electrodes significantly reduce the electrical impedance, as well as the r.m.s. noise level [Keefer, 2008]. However, the biocompatibility and stability of such coatings have not been tested yet for chronic implants.

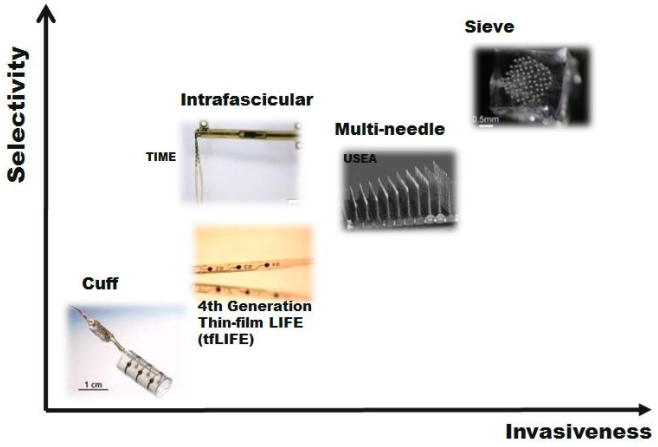

Figure 3.3: Invasive interface classification (adapted from [Micera, 2008]).

Of note, in spite of the variety of specific designs (e.g. cuff, intrafascicular thin film multichannel electrodes, array of microneedles, sieve) and potential applications, all existing invasive neural interfaces use electric signals for both stimulation and recording [Micera, 2008; Cogan, 2008].

3.3. A novel implantable peripheral interface: The concept[4]

Well-established techniques, such as Transcranial Magnetic Stimulation (TMS), show that electromagnetic (EM) stimuli can be used to elicit neural responses, even without a direct contact between the source of scalp stimulation (coil) and the underlying nervous tissue within the brain.

[4] This work has been partly published by the author (*D. Accoto, M. T. Francomano, A. Rainer, M. Trombetta, P. M. Rossini, E. Guglielmelli, "An implantable neural interface with electromagnetic stimulation capabilities", Medical Hypothesis, accepted, January, 2013*; paper n. 3 of *List of Publications*).

Maria Teresa Francomano

According to these considerations, as detailed in the following, a novel strategy has been proposed, based on the use of micro- and nano- technologies, for improving peripheral nerve stimulation capabilities, as well as for reducing the effects of fibrotic reactions.

Studies on the electrical properties of the fibrotic tissue, encapsulating the electrodes after implantation, showed that fibrosis may have a negative impact on the stimulation capabilities of chronically implanted electrodes [Grill, 1994] and may affect the signal-to-noise ratio [Lefurge, 1991].

To address these issues, a novel microprobe is proposed, able to:

- *in situ* implement a TMS-like approach for electromagnetically stimulating peripheral nerves;
- release functionalized (ferro- or superpara-) magnetic nanoparticles (NPs), that selectively bind to neurons, for local intensification and focusing of EM waves;
- release anti-fibrotic drugs for reducing foreign body reaction at the implant site.

The proposed neural interface (Figure 3.4) includes:

- an array of microcoils patterned on a flexible substrate;
- functionalized ferromagnetic or superparamagnetic NPs, released during the biodegradation of a coating (see next item), capable to selectively bind to neurons and to locally focus EM waves thanks to their high magnetic permeability;
- a biopolymer coating, releasing functionalized NPs as well as locally active drugs to impede fibrotic reaction.

The microprobes arrangement can either be intra- or epi- neural (Figure 3.5) in order to achieve the expected stimulus performance in terms of intensity and selectivity.

The excitation of the array of microcoils with time-varying currents generates EM waves, which stimulate neuron membranes without the need for an electric contact between cells and sites of stimulation. This approach, in which

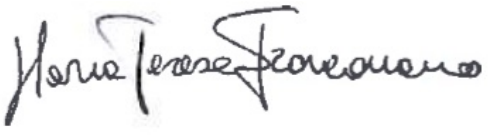

stimulation is mediated by EM waves, is expected to circumvent or reduce the effect of the fibrotic tissue on stimulation.

In case of intra-neural configuration, the microprobe would be inserted into the fascicles (Figure 3.5), while in the epi-neural arrangement the substrate would be wrapped around the nerve (Figure 3.6).

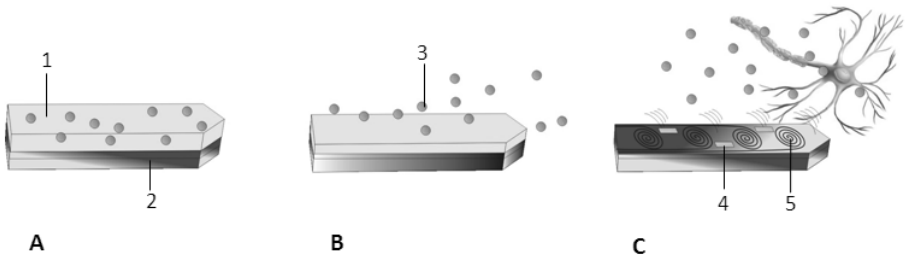

Figure 3.4: Concept of the novel PNS interfaces. (A): a biopolymeric coating (1), spread on a flexible substrate (2) on which microcoils for stimulation (5) and electrodes for registration (4) are micropatterned, holds the functionalized NPs (3); (B): the bioabsorption of the coating causes a controlled release of NPs, which diffuse towards surrounding tissues; (C): NPs specifically bind on neurons, locally intensifying the gradient of electric field along the axon direction. The biopolymer also releases an antifibrotic drug.

The fabrication of the EM microprobes can be based on metallization and passivation layers on a polymeric substrate (e.g. Polyimide, SU-8 and Cycloolefin (COC)). The metal microcoils fabrication can be approached by means of microlithographic technologies. A biocompatible polymeric dielectric film (not bioabsorbable, e.g. SU-8, polyimide), micropatterned on the electrically active elements (microcoils and electrodes) would insulate and protect them from the environment.

For the inhibition/reduction of fibrotic scar formation, an absorbable biopolymeric layer, deposited on the above mentioned dielectric layer, would topically release anti-fibrotic drugs.

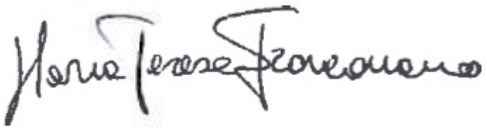

The same polymeric coating would also be responsible for the controlled release of magnetic NPs. Such magnetic NPs should be surface-functionalized with antibodies directed toward axon-specific membrane markers [Dickson, 2002].

With their effective size not exceeding 15-30 nm, NPs would diffuse through tissues with predictable and size-dependent behavior [Florence, 2012; Golneshan, 2011] and selectively bind to neuron axons.

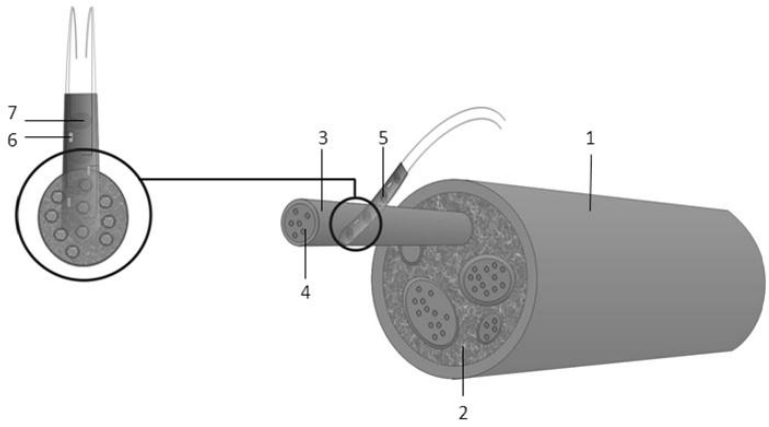

Figure 3.5: Microprobes intra-neural configuration. The microprobe is inserted in the fascicle [epineurium (1), fascicle (2), perineurium (3), axons (4), EM microprobe (5), electrode (6), microcoil (7)].

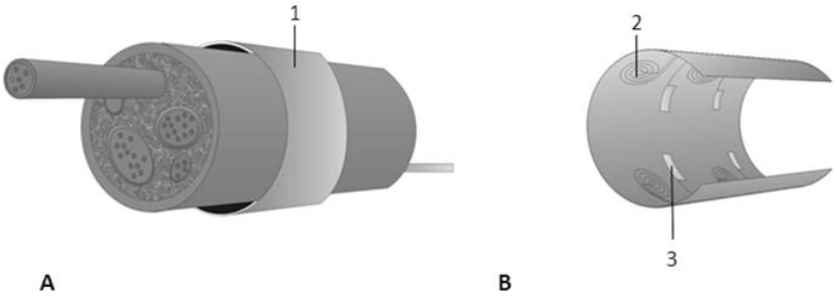

Figure 3.6: Microprobes Cuff configuration. (A): The epi-neural microprobe is wrapped around the nerve (1); (B): The cuff EM microprobe includes microcoils (2) and electrodes (3).

Maria Teresa Francomano

Given their magnetic properties, they would locally focus and intensify the EM field, helping achieving the excitation threshold without the need for a very intense EM field.

The proposed concept has a direct potential application whenever a controlled micro-stimulation of peripheral nerves is necessary, e.g. in prosthetics and assistive technologies for controlling robotic or mechatronic devices, treatment of neurogenic pain, either of peripheral (i.e. diabetic neuropathy, phantom limb syndrome in amputees in its peripheral component) or central (i.e. thalamic, phantom limb syndrome in amputees in its central component) origin, symptomatic treatment of spasticity, dystonia and tremor.

3.3.1. Electromagnetic Stimulation of PNS

Magnetic stimulation of neural tissue has advantages over electrical stimulation in terms of biocompatibility, bioresistance, and operational biotoxicity. Rather than creating an electric field via the injection of a current through biological tissues, as it occurs in electrical stimulation, magnetic stimulation results from the induced EM fields created within the tissue.

Magnetic stimulation in the macro-scale is quite common in neurophysiology. For instance, Transcranial Magnetic Stimulation (TMS, [Barker, 1985; Basser, 2000; Barker, 1999; Geddes, 1991; Hallett, 2000; George, 2003; Hallett, 2007]) has been widely used in the past three decades [Barker, 1985; Rossini, 2007] to depolarize or hyperpolarize neurons in the brain. Nonetheless, EM stimulation of the PNS is a research field still in its infancy. In 1993, Maccabee et al. [Maccabee, 1993] proposed the magnetic stimulation of PNS by means of external devices. Other authors investigated different coils configurations for external EM stimulation, including partially occluded coils [Davey, 1993; Davey, 1998], open coils [Ruohonen, 1998] and multichannel coils [Ruohonen, 1999].

Miniaturized implantable coils represents an alternative to the electrodes currently used for invasive neural interfaces. However, the possibility of generating an effective stimulus by means of implantable microcoils presents several issues, mainly related to technological and thermal constraints. Although preliminary in vitro studies on EM stimulation [Basham, 2008], using microcoils

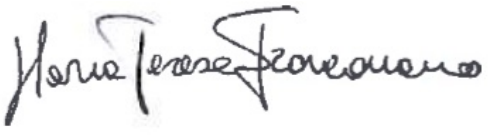

for electrophysiological applications, reported advantages related to the absence of a direct contact between the stimulator and the tissue, till now investigations on implantable EM microprobes used as neural interfaces have not been reported.

3.4. Feasibility analysis of the proposed approach[5]

Rattay et al. [Rattay, 1986] presented an elegant approach for evaluating the response of an axon to extracellular stimulation, by adding a source term to the cable equation [Hodgkin and Rushton, 1946].

An expression adapted to magnetic stimulation was presented in [Roth and Basser, 1990]:

$$\lambda^2{}_m \frac{\partial E_x(x,t)}{\partial x} = -\lambda^2{}_m \frac{\partial^2 V_m(x,t)}{\partial x^2} + \tau \frac{\partial V_m(x,t)}{\partial t} + V_m(x,t) \qquad (3.1)$$

where E_x is the component of the electric field in the same direction of the neuron axon (x), λ_m and τ respectively are the space and time constants of the neural membrane; while V_m is the transmembrane potential.

The left member in eq. (3.1) is the electromagnetic activation function: a neuron response is elicited when this term exceeds a threshold γ (i.e. when $\frac{\partial E_x(x,t)}{\partial x} > \gamma$, for a suitable γ), depending on the myelination state of the nerve.

The electric component of the EM field generated by a microcoil can be calculated by numerical means or, for specific shapes, analytically.

For instance, in [Basham, 2009] the analytical expression of $\partial E_x/\partial x$ is reported for a planar square coil (side length: a; the bottom left corner should be imagined as centered on the origin of the coordinate frame in use). The expression of $\partial E_x/\partial x$ is:

[5] This work has been partly published by the author (*D. Accoto, M. T. Francomano, A. Rainer, M. Trombetta, P. M. Rossini, E. Guglielmelli, "An implantable neural interface with electromagnetic stimulation capabilities", Medical Hypothesis, accepted, January, 2013*; paper n. 3 of *List of Publications*).

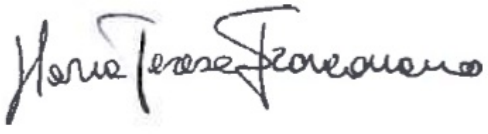

$$E_x = N\frac{dI}{dt}f(x,y,z)^{6} \tag{3.2}$$

where N is the number of turns and f a function of the three coordinates.

Figure 3.7 shows the typical spatial distribution of $\partial E_x/\partial x$ for a square coil, calculated by deriving eq. (3.2) with respect to x.

It can be observed that the depolarization of the nerve fiber is localized at the corners $(a,0)$ and $(0,a)$, while hyperpolarization occurs at the corners $(0,0)$ and (a,a).

Taking into account eq. (3.2), the condition for stimulation becomes: $N\frac{dI}{dt}\frac{\partial}{\partial x}f(x,y,z) > \gamma$. Since the geometry of the coil is fixed, this condition requires sufficiently rapid current ramps $\left(\frac{dI}{dt}\right)$.

A current ramp through a resistance R for a time ΔT dissipates a thermal power (q) given by:

$$q(t) = \frac{R}{3}\left(\frac{dI}{dt}\right)^2 \Delta T^2 \tag{3.3}$$

Equation (3.3) shows that thermal power is proportional to ΔT^2: in order to keep tissue heating low, ΔT must be sufficiently small.

Therefore, a high frequency (i.e. small ΔT) saw-tooth current profile, characterized by a sequence of ramps with constant $\frac{dI}{dT}$, should be used for excitation.

The maximum acceptable value of q depends on temperature rise, which can be evaluated using several models.

For simplicity sake, we adopted a cautionary simplified model, where: *i)* the cooling effect, provided by blood circulation in surrounding tissues, is neglected; *ii)* heat conduction is assumed to be mono-dimensional (1D), i.e. heat is

[6] $f(x,y,z) = -\frac{\mu_0}{4\pi}\cdot\ln\left[\frac{\left(x-a+\sqrt{(x-a)^2+y^2+z^2}\right)\left(x+\sqrt{x^2+(a-y)^2+z^2}\right)}{\left(x+\sqrt{x^2+y^2+z^2}\right)\left(x-a+\sqrt{(x-a)^2+(a-y)^2+z^2}\right)}\right]$

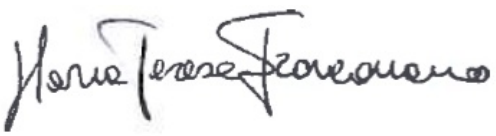

considered to flow away from the source (coil) only in the direction perpendicular to the coil surface; this assumption is cautionary because, by restricting the real 3D heat transfer problem to a 1D geometry, the maximum temperature achieved in the nervous tissue is overestimated.

Let's consider a square microcoil with outer sides 500 um long and 10 turns (N=10). Let each winding be 10 um wide and 10 um thick, and fabricated in Cu (electrical resistivity: $\rho=1{,}69\times10^{-8}\Omega m$). The total resistance of the coil is $R=1\Omega$.

For myelinated fibers the excitation threshold is $\gamma = 365\ mV/cm^2$ [Basser, 1991], which requires $\frac{dI}{dt} \approx 5\ 10^5\ A/s$. For $\Delta T \approx 10^{-6}$s, the maximum temperature raise in the tissue is less than 1.8°C, a value low enough to avoid local hyperthermia [Pisa, 2004].

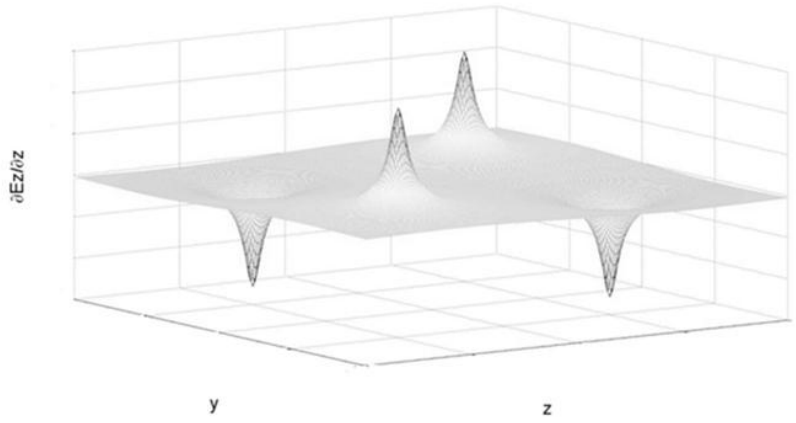

Figure 3.7: Typical spatial distribution of $\partial E_x/\partial x$ generated by a square coil.

A cuff configuration poses less dimensional constraints on the coil dimensions. Indeed, the availability of a relatively large area allows the tiling of several coils, which can be addressed one by one.

In this way, the generated EM field is the vector sum of the field generated by each coil.

Using such configuration, the excitation model predicts stimulation depths up to 1 mm beneath unmyelinated fibers surface, and up to 0.25 mm for myelinated fibers.

Maria Teresa Francomano

3.5. Discussion

An innovative approach to overcome common problems related to PNS stimulation by means of implantable devices has been described.

The proposed solution resorts to microcoils, fabricated on a flexible substrate, for electromagnetically stimulating –*in situ*– the nerves. Recording is carried out by conventional means (i.e. microelectrodes).

The use of flexible substrates allows both epi- and intra-neural configurations. The compliance of the microprobes is also useful in mitigating the effects associated to the mechanical mismatch between the microprobes and the nervous tissue (Chapters 5, 7).

Neurons-specific functionalized magnetic nanoparticles are used as a means to focus EM waves, thus helping the elicitation of membranes depolarization.

Upon implantation, the controlled degradation of an absorbable coating layer, covering the electrode, accompanies the release of functionalized magnetic NPs, which diffuse in the surrounding tissues —in virtue of their small dimensions— and target the axons membranes. At the same time, the coating contributes to mitigate foreign body reaction at the implant site by actively eluting an anti-fibrotic drug.

A preliminary analysis, taking into account thermal constraints, provided evidence of the feasibility of the EM stimulation using implanted microcoils.

Indeed, the evaluations reported in the previous section show that the stimulation threshold can be reached, even without the need of NPs, with a sufficiently small temperature increase.

The depth of the effective stimulation (0.25–1 mm) is not negligible compared to typical (linear) dimensions of peripheral nerves (few mm).

NPs, bound to the surface of the neurons, would increase the excitation depth thanks to their high magnetic permittivity. Conversely, they could ease the requirements for the power supply system, e.g. by reducing the intensity of the current needed to elicit a response, while keeping temperature raise below acceptable thresholds.

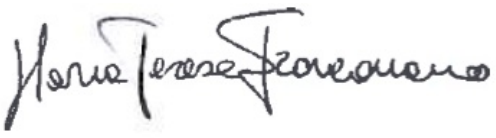

The proposed approach combines technological solutions from such fields as micro- and nano-engineering, neural engineering, and tissue engineering, to develop an implantable device for EM stimulation, capable of overcoming the issues related to purely electric stimulation, thus assuring a stable communication channel with the PNS.

The novel neural interface has an impact in several fields, different from the voluntary control of prostheses, where a stable bi-directional communication channels with the PNS is central: *i)* neurogenic pain treatment, either of peripheral or central origin; *ii)* spasticity, focal dystonia and tremor selective treatment; *iii)* treatment of phantom limb pain.

Moreover, the outcomes of the research may open new avenues for the minimally invasive stimulation of the CNS and for neuroprotective therapies (e.g. oncology and neural regeneration).

Neverthless, complementary works should be performed for validating the hypothesis, by means of *in silico* and *ex vivo* experiments.

In particular, the necessary steps for testing and validate the hypothesis can be summarized as follows:

- Design of the excitation circuit for the generation of the current ramps;
- Set-up of a multiphysics simulation environment for modeling:
    i. the physical interaction between EM field, NPs and neurons, taking into account thermal constraints;
    ii. the diffusion of NPs through tissues;
    iii. the degradation/swelling of the bioactive coating;
    iv. the anti-fibrotic drug release process.
- Developing *in vitro* and *ex vivo* set-ups in order to perform electrophysiological measurements on biological samples (e.g. neurons and nerves explants) subject to EM stimulation.

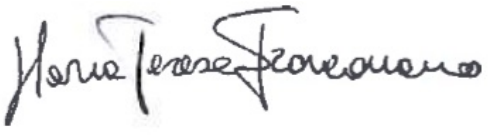

- Addressing biocompatibility issues by means of *in vitro* tests, in order to assess the chemical stability and biocompatibility of the functionalized NPs and the bioactive coating.
- Addressing safety issues, with special regards to EM stimulation. The Specific Absorption Rate index (SAR, expressed in W/Kg) measures the energy absorbed by the tissues during time varying electric fields exposure. The measured SAR index should be compared to those reported in safety protocols.

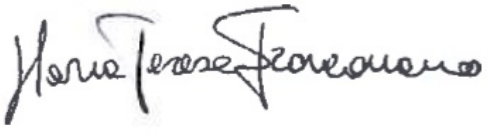

Bibliography

[Barker, 1985] A.T. Barker, R. Jalinous, I.L. Freeston, Non-Invasive magnetic stimulation of human motor cortex, The Lancet, May 11 1985,1105-1106.

[Barker, 1999] A.T. Barker, The history and basic principles of magnetic nerve stimulation, Electroencephalogr. Clin. Neurophysiol. Suppl., 1999, 51, 3–21.

[Basham, 2008] E. Basham, W. Liu, Z. Yang, In vitro magnetic stimulation of unmyelinated nerves, 30th Annual International IEEE EMBS Conference Vancouver, British Columbia, Canada, August 20-24, 2008.

[Basham, 2009] E. Basham, Z. Yang, N. Tchemodanov, W. Liu, Magnetic Stimulation of Neural Tissue: Techniques and System Design, Implantable Neural Prostheses 1, Biological and Medical Physics, Biomedical Engineering, 2009, 293-351.

[Basser, 1991] B. Basser, P J; Roth, Stimulation of a myelinated nerve axon by electromagnetic induction, Medical Biologicial Engineering Computing, 1991, 29, 261-268.

[Basser, 2000] P.J. Basser and B.J. Roth, New currents in electrical stimulation of excitable tissues, Annual Review of Biomedical Engineering, 2000, 2(1), 377–397.

[Cogan, 2008] S.F. Cogan, Neural Stimulation and Recording Electrodes, Ann. Rev. of Biomed. Eng., 2008, 10, 275-309.

[Davey, 1993] K. Davey, L. Luo and D. Ross, Towards Function Magnetic Stimulation (FMS) Theory and Experiment, IEEE Transactions on Biomedical Engineering, 1993.

[Davey, 1998] K. R. Davey, C. Epstein, Magnetic nerve stimulator for exciting peripheral nerves, 1998, US. Pat. No. 5725471.

[Dickson, 2002] Dickson T. C., Mintz C. D., Benson D.L., Salton S. R. J. Functional binding interaction identified between the axonal CAM L1 and members of the ERM family, J Cell Biol 2002, 157, 1105–1112.

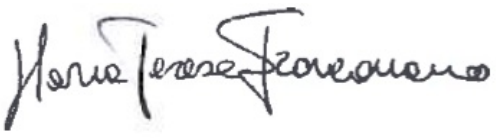

[Florence, 2012] Florence A. T. "Targeting" nanoparticles: The constraints of physical laws and physical barriers, J Control Release 2012 doi: 10.1016/j.jconrel.2012.03.022.

[Geddes, 1991] L.A. Geddes, History of magnetic stimulation of the nervous system, J. Clin. Neurophysiol., 1991, 8(1), 3–9.

[George, 2003] M.S. George et al., Transcranial magnetic stimulation, Neurosurgery Clinics of North America, 2003, 14(2), 283–301.

[Golneshan, 2011] Golneshan A. A., Lahonian M. Diffusion of magnetic nanoparticles in a multi-site injection process within a biological tissue during magnetic fluid hyperthermia using lattice Boltzmann method, Mech Res Commun 2011;38, 425–430.

[Grill, 1994] W.M. Grill, J. T. Mortimer, Electrical properties of implant encapsulation tissue, Ann. Biomed. Eng., 1994, 22, 23-33.

[Hallett, 2000] M. Hallett, Transcranial magnetic stimulation and the human brain, Nature, 2000, 406(6792), 147–150.

[Hallett, 2007] M. Hallett, Transcranial magnetic stimulation: a primer, Neuron, 2007, 55(2), 187–199.

[Heiduschka and Thanos, 1998] Heiduschka P, Thanos S (1998). Implantable bioelectronic interfaces for lost nerve functions. Prog Neurobiol 55:433–461.

[Hodgkin and Rushton, 1946] A.L. Hodgkin and W.A.H. Rushton, The electrical constants of a crustacean nerve fibre, Proceedings of the Royal Society of London. Series B, Biological Sciences (1934–1990), 1946, vol. 133(873), 444–479.

[Keefer, 2008] E.W. Keefer, B.R. Botterman, M.I. Romero, A.F. Rossi, G.W. Gross, Carbon nanotube coating improves neural recordings, Nature Nanotechnology, 2008, 3, 434–439.

[Lefurge, 1991] T. Lefurge, E. Goodall, K. Horch, L. Stensaas, A. Schoenberg, Chronically implanted intrafascicular recording electrodes, Ann. Biomed. Eng., 1991, 19, 197– 207.

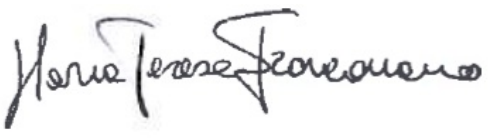

[Maccabee, 1993] P. J. Maccabee, V. E. Amassian, L. P. Eberle and R. Q. Cracco, Magnetic coil stimulation of straight and bent amphibian amphibian and mammalian peripheral nerve in vitro: locus of excitation, Journal of Physiology, 1993, 460, 201-219.

[McKinley, 2009] M. McKinley, V. O'Loughlin, "Human Anatomy", McGraw-Hill Companies, Incorporated, Aug 7, 2009 - 874 pages.

[Micera, 2008] S. Micera, X. Navarro, J. Carpaneto et al., On the use of longitudinal intrafascicular peripheral interfaces for the control of cybernetic hand prostheses in amputees, IEEE Trans. Neural Syst. Rehabil. Eng., 2008, 16(5), 453-72.

[Micera, 2009] S. Micera and X. Navarro, Bidirectional interfaces with the peripheral nervous system, Int. Rev. Neurobiol., 2009, 86, 23–38.

[Navarro, 2005] X. Navarro, T. B. Krueger, N. Lago, S. Micera, T. Stieglitz, P. Dario, A critical review of interfaces with the peripheral nervous system for the control of neuroprostheses and hybrid bionic systems, Journal of Peripheral Nervous System, 2005, 10, 229-258.

[Peters, 1991] Peters A., Palay S. L., Webster H. F. (1991). The Fine Structure of the Nervous System: Neurons and Their Supporting Cells, 3rd Edn. Oxford University Press, New York.

[Pisa, 2004] S. Pisa, M. Cavagnaro, E. Piuzzi, P. Bernardi, J. Lin, Power density and temperature distribution produced by an interstitial array of sleeved slot antennas for hyperthermic cancer therapy, Microwave Theory and Techniques, IEEE Transactions on, 2004, 51(12), 2418-2426.

[Rattay, 1986] F. Rattay, Analysis of models for external stimulation of axons, IEEE Transactions on Biomedical Engineering, 1986, 33, 974-977.

[Rossini, 2007] P. M. Rossini, S. Rossi, Transcranial magnetic stimulation. Diagnostic, therapeutic and research potential, Neurology, 2007, 68 (7), 484-488.

[Rossini, 2010] P.M. Rossini, S. Micera S, A. Benvenuto et al., Double nerve intraneural interface implant on a human amputee for robotic hand control, Clin. Neurophysiol., 2010, 121, 777-783.

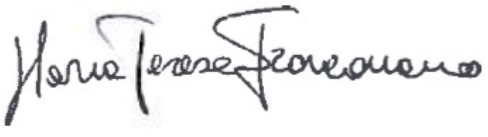

[Roth and Basser, 1990] B. J. Roth and P. J. Basser, A model of the stimulation of a nerve fiber by electromagnetic induction, Biomedical Engineering, IEEE Transactions on, 1990, 37(6), 588–597.

[Ruohonen, 1998] J. Ruohonen, P. Ravazzini, F. Grandori, Functional magnetic stimulation: theory and coil optimization, Bioelectrochemistry and Bioenergetics, 1998, 47, 213-219.

[Ruohonen, 1999] J. Ruohonen, P. Ravazzini, F. Grandori, R.J. Ilmoniemi, Theory of multichannel Magnetic Stimulation: Toward Functional Neuromuscolar Rehabilitation, IEEE Transactions on Biomedical Engineering, 1999, 46 (6), 646-651.

[Stieglitz, 2004] Stieglitz T., Schuttler M., Koch K. P. (2004). Neural prostheses in clinical applications–trends from precision mechanics towards biomedical microsystems in neurological rehabilitation. Biomed Tech (Berl) 49:72–77.

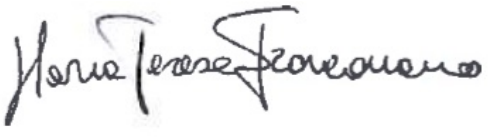

Chapter 4

The artificial sense of touch

4.1. The importance of the tactile feedback

Together with the ability to grasp and manipulate objects, a hand amputee loses the capability to perceive and explore the surrounding world through the sense of touch. A direct sensory feedback to the amputee implies a direct connection between the prosthesis and the nervous afferent channels.

Hence, the attention is mainly paid to the development of a rich tactile sensory feedback for the low-level force control.

Dexterous manipulation requires forces and motions control at the contact between the fingers and the environment, which can only be accomplished through touch (Chapter 2). Indeed, people become clumsy when deprived of reliable tactile information through numbness of anesthetized or cold fingers [Johansson and Westling, 1984].

It is also important to know the position of the object in the space, its size and shape in order to adequately configure the fingers during grasping: a precision grip involves the thumb and the index finger, whereas a power grip the palm and all the fingers.

Since tactile sensing is central in manipulation, robotics research on manipulation stimulated the investigation on the *artificial sense of touch* to endow robots with manipulation capabilities similar to those of humans.

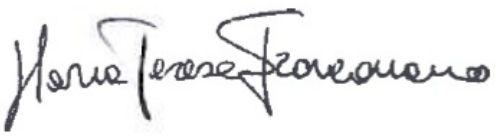

4.2. Main Requirements for Tactile Sensory Systems

A tactile sensor should detect a contact event and information related to the contact areas (e.g., exerted forces, object properties, occurrence of slip events, etc.).

Having in mind the final aim of integrating the sensory system on robotic fingers/hands, it is high desirable to have compliant sensors, which should be compact, made on a flexible/stretchable substrate and robust with regards to possible interferences from other devices as well as to mechanical vibrations due to fast movements of the robotic fingers or to the actuation system of the robotic phalanxes.

The sensory system should also be resilient and resistant to chemical stresses.

Furthermore, in order to achieve performances comparable with those of humans, the tactile sensors should *i)* have an adequate response time (i.e. <<100 ms), thus saving enough computation time to the control system for the grasping forces adaptation and *ii)* be insensitive to grasped object properties, thus allowing to operate in unstructured environment. Linearity and low hysteresis are also desired requirements.

Table 4.1 lists the above mentioned requirements and other main features for tactile sensors. A subdivision in technical and bio-inspired requirements is also reported.

Moreover, it appears desirable to reproduce the varied nature and distribution of human receptors, by developing multimodal array of miniaturized sensors, able to detect different contact parameters. Tactile sensory systems, arranged in skin-like configuration, are therefore required.

Human skin is a *multilayered, nonlinear, nonhomogeneous, and viscoelastic* medium [Dahiya, 2010].

In vivo examinations of the mechanical behaviour of the human skin demonstrated that, in a normal state of hydration, its Young's Modulus is in the range 4.6-20MPa under tension [Manschot and Brakkee, 1986] and 420-850kPa

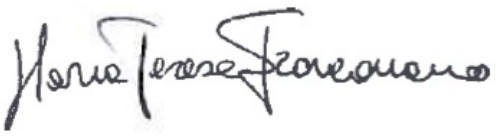

under torsion [Agache, 1980]. During uniaxial deformation the maximum stress tolerable by the skin is about 21MPA.

Technical requirements		**Bio-inspired requirements**
• High sensibility • Good accuracy and repeatability • Low temperature drift • High robustness (with respect to EM and mechanical disturbances)	• Lightweight • Low cost • Low power consumption • Low number of electrical connections • Integrability on compliant and robust packaging	• Maximum spatial resolution: 1 mm • High force sensibility (1-100 N) • Sensing elements density comparable with mechanoreceptors (Table 2.2) • Response time << 100ms

Table 4.1: Main tactile sensors requirements for prosthetic robotic hands.

But the skin is not a homogeneous medium. In fact, it comprises layers with different thicknesses and mechanical properties. Skin biomechanics is bound to play an important role in the tactile perception, allowing, for example, to convert contact indentation into stresses/strains signals. Moreover, the interlocking layer between the *epidermis* and *dermis* creates a filtering mechanism that distributes forces and stresses from their point of application, with a modulated spatial resolution, depending on the density distribution of the mechanoreceptors [Quilliam, 1978]. Finally skin ridges magnify mechanical signals and therefore the tactile acuity [Maeno, 1998].

Taking inspiration from nature, an ideal artificial tactile sensory systems should be embedded into elastic materials, mimicking the human skin features, especially its conformability, which increases the size of the contact area and allows biological receptors to derive such information as detailed contours of objects.

The aforementioned requirements are high desirable for the specific application but some of them are still technologically challenging, especially in terms of

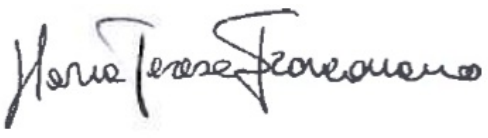

manufacturability and scalability (e.g. for issues related to the type and number of interconnections) as well as in terms of response times and reproducibility.

4.3. Artificial tactile sensors

Tactile transduction techniques are mainly based on capacitive, piezoresistive, piezoelectric, inductive and optical methods [Tiwana, 2012].

There are several advantages and disadvantages for each working principle, which are well established [Najarian, 2009; Dahiya, 2010, Tiwana 2012] and summarized in Table 4.2 [Tiwana, 2012].

Transduction technique	Modulated parameter	Advantages	Disadvantages
Capacitive	Change in capacitance	Excellent sensitivity Good spatial resolution Large dynamic range	Stray capacitance Noise susceptible Complexity of measurement electronics
Piezoresistive	Changed in resistance	High spatial resolution High scanning rate in mesh Structured sensors	Lower repeatability Hysteresis Higher power consumption
Piezoelectric	Strain (stress) polarization	High frequency response High sensitivity High dynamic range	Poor spatial resolution Dynamic sensing only
Inductive LVDT	Change in magnetic coupling	Linear output Uni-directional measurement High dynamic range	Moving parts Low spatial resolution Bulky Poor reliability More suitable for force/torque measurement applications
Optoelectric	Light intensity/spectrum change	Good sensing range Good reliability High repeatability High spatial resolution Immunity from EMI	Bulky in size Non-conformable
Strain gauges	Change in resistance	Sensing range Sensitivity Low cost Established product	Calibration Susceptible to temperature changes Susceptible to humidity Design complexity EMI induced errors Non-linearity Hysteresis
Multi-component sensors	Coupling of multiple intrinsic parameters	Ability to overcome certain limitations via combination of intrinsic parameters	Discrete assembly Higher assembly costs

Table 4.2: Main advantages and disadvantages of tactile force sensors. Adapted from [Tiwana, 2012].

4.3.1. Capacitive tactile sensors

A capacitive sensor includes two, usually parallel, conductive plates with a dielectric material between them. The capacitance, C, can be expressed as: $C = \varepsilon_0 \varepsilon_r \frac{A}{d}$, where A is the overlapping area of the two parallel plates, whereas ε_0 and ε_r are the permittivity of the vacuum and the relative permittivity of the dielectric material, respectively. Finally, d is the distance between the two plates.

Maria Teresa Francomano

If the dielectric is a compliant material, an applied force changes the distance (d) between the two plates, thereby varying the capacitance.

Capacitive tactile sensors generally show a good frequency response, high spatial resolution, and have a large dynamic range.

Anyhow, they are more affected by noise, due to field interactions and fringing capacitance, thus requiring relatively complex readout electronics for noise filtering.

One of the major advantages of capacitive sensors refers to their technological flexibility. Indeed during the years they have been developed implementing different strategies: e.g. on flexible [Mannsfeld, 2010] and stretchable substrates [Cotton, 2009] as well as using carbon nanotubes [Lipomi, 2011], nanofibers [Pang, 2012] and paper [Mazzeo, 2012].

4.3.2. Piezoresistive tactile sensors

Piezoresistive sensors have a pressure sensitive unit, which changes its resistance if forces are applied. The resistance of a resistor having length l, cross-sectional area A and resistivity ρ, is: $R = \rho\frac{l}{A}$. For a piezoresistive material, resistance changes are mainly due to variations of resistivity occurring when a force is applied, rather than to changes of the linear dimensions.

Usually the sensing element is a conductive rubber, an elastomer, or a specific conductive ink.

This kind of sensors can be easily manufactured. Compared to capacitive sensors, they require simpler electronic circuits, being the changes in resistance easy to be detected.

Moreover, they are less susceptible to noise. Conversely, piezoresistive sensors may be affected by hysteresis and may exhibit a lower frequency response compared to capacitive sensors.

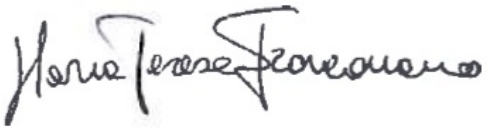

4.3.3. Piezoelectric tactile sensors

Some materials, if deformed, generate an electric potential [Jaffe, 1971; Skoog, 1985], directly proportional to the applied stimulus (e.g. force, pressure or strain). There are two differential equations governing the behaviour of a piezoelectric continuum: Newton's laws of motion and the quasistatic approximation Maxwell's equation.

The generated voltage, V, from a piezoelectric material can be calculated as: $V = S_v PD$, where S_v is the voltage sensitivity of the material [Vm/N], P is the applied pressure [N/m^2], and D is the thickness of piezoelectric material [m].

Voltage sensitivity values are provided by the manufacturer and depend on the specific material and its geometry. Depending on their internal structure, piezoelectric materials allow distinguishing transverse, longitudinal and shear forces.

These sensors exhibit a very good frequency response, which makes them an ideal choice for measuring vibrations.

4.3.4. Inductive tactile sensors

The working principle of these transducers is based on the modulation of the mutual inductance between two coils, one of which (the primary one) carries ac excitation (V_{ref}) that induces a steady ac voltage in the secondary coil. The movement of a ferromagnetic object within the flux path alters the coupling between the coils. The magnetic flux coupling between two coils is converted into a voltage, according to: $V=-NdBA/dt$, where N is the number of turns, B is the intensity of the magnetic field, and A is the area of the coil.

These sensors are bulky in size and require complex readout electronics.

4.3.5. Optoelectric tactile sensors

Optoelectric sensors consist of a light source, a transduction medium and a photodetector. The working principle lies in detecting changes in the light transmission/reflectance intensity or in the light spectrum, when forces are applied.

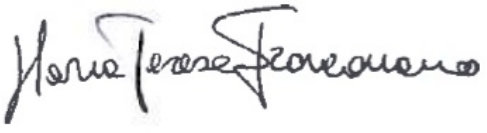

Although they have many benefits, their size, rigidness and high power demand are the major disadvantages.

4.3.6. Strain gauges

Strain gauges are very sensitive, low cost sensors able to detect mechanical strain causing a change in their resistance [Window, 1992]. The reference equation for strain gauges is: $\frac{\Delta R}{R} = G\varepsilon$, which expresses the resistance variation (ΔR) as a function of the applied strain (ε).The parameter G is the *gauge factor*. Unlike piezoresistive sensors, the mechanotransduction properties of strain gauge devices are dominated by form factors, rather than by variations in resistivity.

These sensors have been widely used, however, they are highly susceptible to humidity and temperature changes.

Moreover, usually they have high hysteresis and often non-linear responses.

4.4. Slip sensors[7]

Slip sensors can be considered as a sub-set of tactile sensors. Over the years additional strategies have been investigated for developing slip sensors, as demonstrated by an increasing number of related publications (Figure 4.1).

The basic slip sensor is a binary device able to detect slip absence. Some sensors detect slip at its incipience, other only total slip (see section 2.2.2.2). More elaborated sensors can provide information about slip direction and speed.

Even if most of tactile sensors are bioinspired [Dahiya, 2010; Tiwana, 2012], humans' "slip sense" is hard to emulate because there is not a single specific receptor devoted to slip detection to be mimicked (Chapter 2).

The lack of a clear biological model to take inspiration from generated a varied landscape of approaches, that differ from each other in terms of: *i)* parameters to be monitored (e.g. object displacement, microvibrations, normal and shear

[7] This work has been partly published by the author (*M. T. Francomano, D. Accoto, and E. Guglielmelli, "Artificial Sense of Slip–A Review", IEEE Sensors Journal, 2013, DOI:10.1109/JSEN.2013.2252890*; paper n. 4 of *List of Publications*).

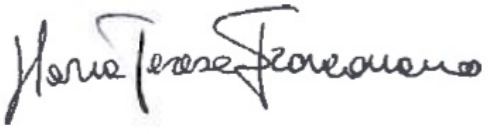

forces, thermal flows), *ii)* transduction mechanisms (e.g. piezoresistive, piezoelectric, capacitive, optical, magnetic, thermal), and *iii)* technological solutions (e.g. soft/flexible materials, MEMS).

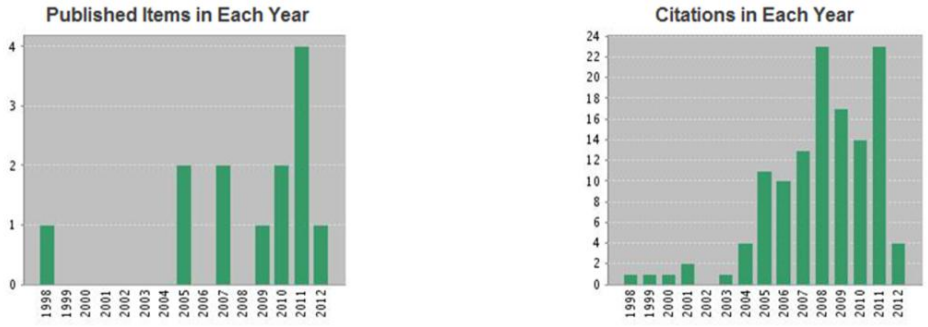

Figure 4.1: Number of publications (on the left) and citations (on the right) (by ISI Web of Knowledge); research keywords: "Slip sensor prosthetic" OR "slide sensor prosthetic" OR "slippage sensor prosthetic".

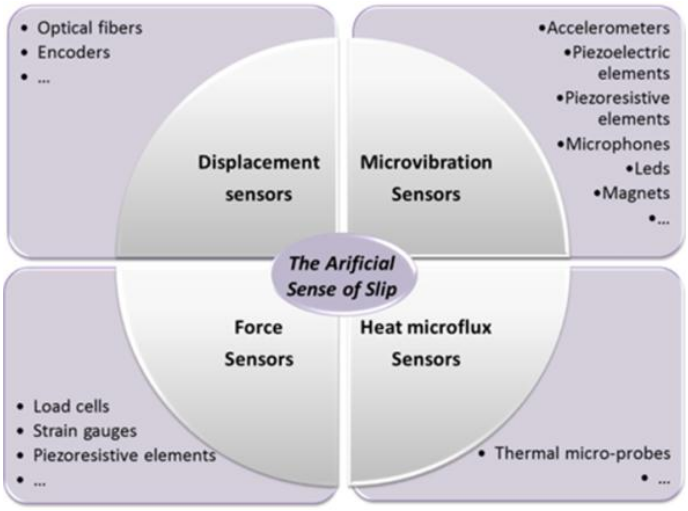

Figure 4.2: Slip sensors: a taxonomy based on the detected physical quantity associated to slip.

A possible taxonomy of slip sensors is shown Figure 4.2, where four main classes of sensors are proposed according to the physical quantity monitored. Each class encompasses sub-categories characterized by different transduction means.

Maria Teresa Francomano

Specific devices in the sub-categories differ for their technological implementation.

4.4.1. Displacement sensors

Displacement-based slip sensors detect the relative motion between finger tips and the object (Figure 4.3).

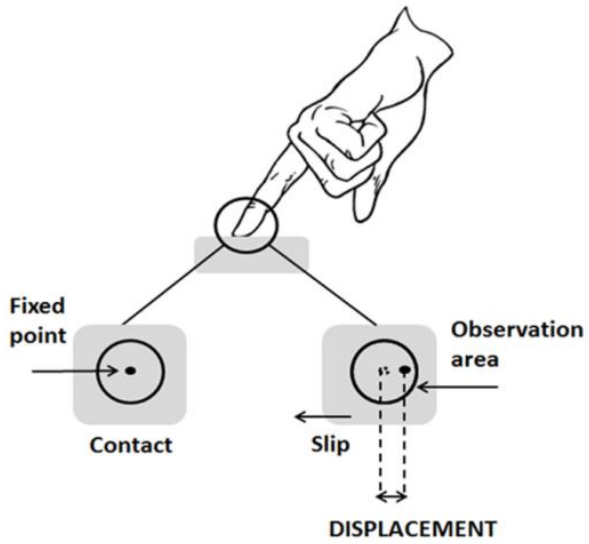

Figure 4.3: Slip detection by displacement monitoring. Slip causes the motion of a point within the contact area.

Such displacement may cause the motion of mechanical parts, e.g. discs or balls, connected to magnetic or optical transducers [Yuan, 2001]. Since mechanical parts are prone to the accumulation of impurities, more recent sensors have no external moving mechanism, and detect relative displacement by comparing a sequence of images captured by a CMOS sensor at each flashing of a light-emitting diode (LED). Both mechanical and optical embodiments may provide information about slip speed and direction.

These classes of sensors have been mainly mounted on the end-effectors of industrial manipulators. Despite their low cost and insensitivity to object roughness, their application to hand prostheses is hindered by their difficult integrability into cosmetic gloves. Moreover, moving mechanical parts, mediating the contact between the robotic finger pad and the object, may negatively affect grasp stability.

Maria Teresa Francomano

A few attempts have been reported integrating optical and pressure sensors. The data flow generated by these multimodal sensors was managed by bioinspired algorithms [Hosoda, 2002], [Ikeda, 2004].

The integration of a vision system and a displacement tactile sensor is computationally demanding, requiring both image processing and soft computing (e.g., Hebbian artificial neural networks [Hosoda, 2002]) algorithms. The high computational cost, nonetheless, is compensated by the good reliability of the whole slip sensor, deriving from its intrinsic redundancy [Hosoda, 2002].

4.4.2. Microvibration transducers

The onset of slip produces small vibrations at the contact surface between the fingertip and the object (Figure 4.4). In humans the "slip sense" is mainly based on detecting vibrations ranging from 50 to 1000 Hz. Microvibrations detection has been the most pursued approach so far in bioengineering. Evidences have also been provided about the capability of this strategy of detecting incipient slip [Dahiya, 2010; Tiwana, 2012].

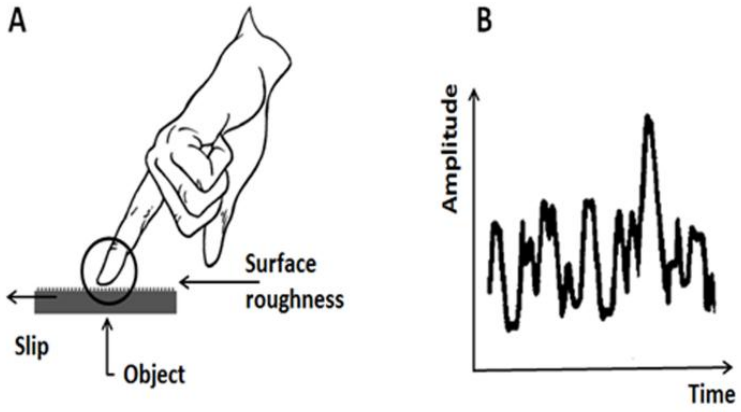

Figure4.4: Slip detection by microvibrations monitoring. A: onset of vibrations during slipping due to the roughness of the surfaces in contact; B: an example of typical vibration signal.

Vibrations have multiple harmonic components, with different frequencies and phases. Theoretically, vibrations can be monitored by measuring the displacement of a seismic mass and calculating its first and second time

Maria Teresa Francomano

derivatives. Displacement measures emphasize the amplitude of low frequency harmonics (<1 Hz), while acceleration emphasizes high frequencies (> 100 Hz).

Vibration can be detected directly (by measuring the intensity and frequency of the vibration) or indirectly (by characterizing the excitation source, i.e. forces/ torques applied to the vibrating system). Direct vibration transducers are accelerometers or acoustic microdevices. Indirect transducers are usually based on load sensors.

In both cases, due to the nature of the signal, a Fourier analysis is usually performed. Different algorithms [Holweg, 1996] are developed for scanning the FFT signal. The analyzed parameters can then be compared with a proper threshold value, using an offline elaboration [Holweg, 1996, Cotton, 2007], or they can be evaluated online using an artificial neural network [Cotton, 2007].

4.4.2.1. Accelerometers

Accelerometers are a well-established sensor technology, characterized by a small footprint and low power consumption. Over the years they found several applications in hand prosthetics. Pioneering works in the field of slip sensing resorted to one single accelerometer embedded in a robotic fingertip and covered by a foam [Cutkosky, 1989; Tremblay, 1993]. The detection technique has been later improved by adding a second accelerometer for enhancing the signal-to-noise ratio [Tremblay, 1993]. In line with the same approach, more recently three-axis accelerometers have also been used [Lowe, 2010].

Accelerometers have also been integrated in sensorized skins as part of a network of multimodal sensor modules. In the HEX-O-SKIN [Mittendorfer, 2011], impact, slip, and roughness are inferred from a cost-effective, small-size, and low-power digital 3-D accelerometer (BOSCH BMA150, also embedding a temperature sensor). This solution, currently applied to humanoid robots [Mittendorfer, 2011], looks plausibly applicable to prosthetics.

4.4.2.2. Acoustic detectors

MEMS microphones can detect the ultrasound (from 50 kHz to 1 MHz) Acoustic Emission (AE) at the contact area associated to slip [Wang, 2009]. AE has been

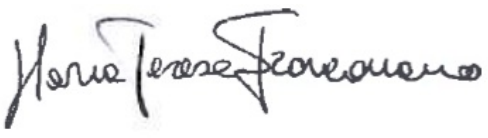

exploited since 1987 in the field of robotic manipulation to detect slip [Dornfeld, 1987]. Unfortunately, acoustic transducers are sensitive to external disturbances [Kyberd, 1992]. In order to improve the signal-to-noise ratio, the microphone can be isolated suspending it in a foam-filled chamber contacting to the finger surface through an elastomeric membrane [Kyberd, 1992]. In this way the microphone is mechanically decoupled from the external environment as well as from the possible vibrations generated by motors. This detection strategy is highly dependent from object surface roughness, though. Shinoda et al. in 2000 proposed an acoustic resonant tensor cell (ARTC) including a cavity inside an elastic body and an ultrasound detector. The proposed sensor is capable of detecting slip direction by analyzing the resonant frequency of ultrasonic waves [Shinoda, 2000].

Recently, a Bayesian exploration algorithm has been developed and implemented using an acoustic slip sensor (BioTac, by SynTouch [Fishel and Loeb, 2012]). The algorithm allows to adaptively select the optimal explorative movements for characterizing and identifying the touched objects [Fishel and Loeb, 2010]. Tests have shown that the exploratory movements allows the slip sensor to be used to discriminate similar textures with a success rate exceeding that of humans.

4.4.2.3. Piezoelectric materials

Being capable of directly converting mechanical energy into electric energy, piezoelectric materials have been widely used for detecting slip-induced vibrations [Cranny, 2005]. Polyvinylidene Fluoride (PVDF) is a flexible polymer, available in film, with a good dynamic response. PVDF has been used for developing multi element-stress-rate sensors embedded in robotic fingertips made of silicone rubber and foam [Yamada, 2002]. PVDF strips can be placed at different depths beneath the surface of a soft robotic fingertip, allowing the detection of the three components of the subsurface stresses [Cotton, 2007; Hosoda, 2006; Howe, 1993].

In order to evaluate the friction coefficient, strain sensors have also been used, monitoring the local deformations in the stick/slip regions of the contact area [Yamada, 2002; Fujimoto, 2003].

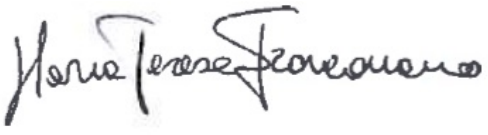

PZT (Lead Zirconate Titanate) is a ceramic perovskite material, with sensitivity about one order of magnitude higher than that of PVDF (130 pC N-1 for typical PZT, compared to 20–30 pC N-1 of PVDF) [Cotton, 2007]. Also Fluorocarbon PVF2 has been used for dynamic measurements and friction estimation [Tremblay, 1993]. In order to amplify the reading from the sensor, both cantilever [Cranny, 2005] and bimorph arrangements [Nishihara, 1996] have been used.

4.4.2.4. Piezoresistive materials

Piezoresistive materials are largely used in force sensors, but a few examples exist of slip sensors employing these materials [Dario, 1996]. Recently a MEMS-based technology, named Micro-Force/Moment-Sensing (MFMS), has been presented [Ho, 2011]. The sensory system consists of four crossed beams embedding piezoresistors. Experiments have shown that the sensor response time should allow to reach performance comparable to those of humans (i.e. forces adaptation in less than 100 ms) [Dahiya, 2010; Flanagan, 1993].

4.4.2.5. Photoelastic materials and photoelectric devices

Some photoelastic materials, exhibiting birefringence at low strain, can be exploited in slip sensing [Dubey, 2006]. Early prototypes resorted to a camera and dedicated image processing techniques to infer slip. The computational cost of this sensors increases with the desired spatial resolution, which typically is of about 0.1 mm [Hopkins, 1992].

Gofuku et al. (2000), embedded a slip sensor, comprised of photo-reflectors and a conductive rubber, in an artificial hand [Gofuku, 2000]. Slip detection was limited to objects with a patterned surface (e.g. color or roughness changes over the contact area), thus precluding its effectiveness in case of smooth or monochromatic objects.

In another work, by Chen et al. (2010), slip-induced microvibrations were detected by a photoelectric apparatus, comprising LEDs and photodiodes, coupled to a vibrating rubbery sensing element [Chen, 2010]. A fuzzy logic controller successfully modulated grasping forces according to slip signals.

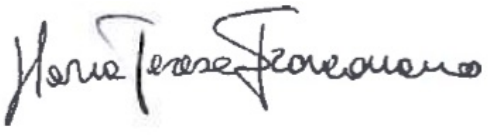

4.4.2.6. Others

In addition to those already outlined, other, less common, transduction principles have also been exploited over the years.

A Hall vibration detector has been used in [Kyberd, 1993]. Here, an elastomer, deformed by external forces, displaces a magnet, whose position is detected by the Hall sensor.

Also pressure sensitive conductive rubbers, coupled to Center of Pressure (CoP) tactile sensors, have been employed for robotic hands [Teshigawara, 2011] in order to detect high frequency vibration components due to object slipping.

4.4.3. Force sensors

Force sensors can be used to infer slip occurrence, provided that all force and torque components at the contact point are measured [Melchiorri, 2000] (Figure 4.2). Conversely, not all force/torque components are needed if the detection is limited to: *i)* vibrations induced by stick-slip phenomena [Tremblay, 1993]; *ii)* changes in pressure distribution [Holweg, 1996]; or *iii)* surface deformations [Fujimoto, 2003].

One of the simplest control methods for avoiding slip events is to estimate in real time the normal grip force needed to balance the tangential force (Figure 2.2). Such calculation may be directly performed if the friction coefficient is known and it may take into account the mechanical properties of the fingertip through a contact model, e.g. Hertz model [Melchiorri, 2000].

Three-axis force sensors have been the most used, because they allow to simultaneously detect normal and shear forces [Hackwood, 1983]. Wettels et al. in 2009 presented a grasp control algorithm for anthropomorphic prosthetic hands [Wettels, 2009], employing a biomimetic tactile sensor based on a compliant three-axis force sensing mechanism [Wettels, 2008]. The sensor consists of a rigid central core with electrodes distributed over its surface; a conductive fluid and a silicone elastomeric skin covering the whole system. By applying an alternating current to each electrode, the impedance of each volumetric flow path (from a fixed external point to a reference electrode) can be

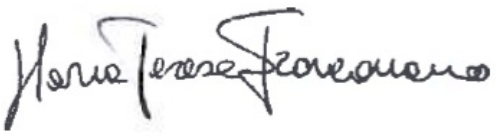

characterized. Once external forces are applied, the impedance pattern changes according to force magnitude and direction, contact point location and object shape [Wettels, 2009]. A similar approach has been implemented using MEMS strain gauges on a flexible substrate [Engel, 2003]. MEMS technology has also been adopted for developing a 1.4 mm^3 3D silicon microsensor embedded in a soft, compliant packaging [Beccai, 2005; Valdastri, 2005]. The microsensor consists of a high aspect ratio silicon structure (625 um thick), an integrated silicon mesa, transmitting forces to a flexible tethered structure, and four piezoresistors used independently to detect normal and shear contact forces [Beccai, 2008]. Slip experiments, focused on the transitions between static and dynamic friction conditions at the finger-object interface, have been performed. Sensor signals have been processed using a cumulative summation algorithm. Results show response times in slip detection between 24.5 ms and 44 ms [Beccai, 2008].

4.4.4. Heat microfluxes detectors

Thermal sensors have been mainly used in robotics hands for measuring objects thermal properties, such as temperature, heat capacity and thermal diffusivity [Engel, 2005; Monkman, 1993; Russell, 1985]. The first example of a thermal slip detector, where the temperature change induced by the motion of the touched object was recorded, was presented in 1986 for the detection of gross slip phenomena in industrial robotics application [Video-tape on SRI Sensor Research, 1986]. Accoto et al. presented in 2008 a slip microsensor where the sensing element is a planar gold microheater, kept at a constant temperature, slightly above room temperature (isothermal sensor), by a dedicated current control [Accoto, 2008]. Slip increases the heat flow from the heater (warmer) to the object (cooler), as shown in Figure 4.5. A slip signal is fired, typically in less than 60 ms, when the increase of the current, needed for keeping the microheater in isothermal condition, overcomes a given threshold. The sensor, with no moving parts, is not affected by spurious vibrations and its performance does not depend on object roughness. The first prototype has been later optimized [Accoto, 2010] and fabricated on a flexible substrate to ease its integration over curved robotic fingertips [Francomano, 2012].

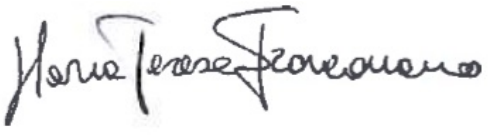

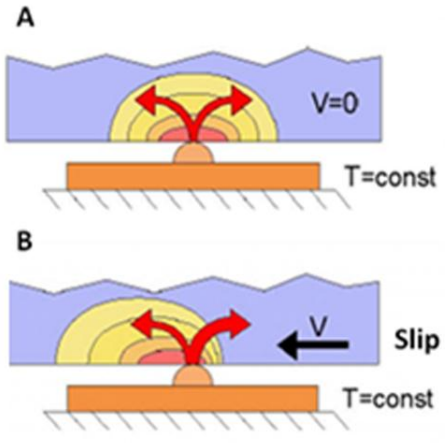

Figure 4.5: Slip detection by monitoring thermal changes in thermal microfluxes. When a microheater is in thermal contact with an object, with zero relative speed, only heat conduction occurs (A). During object motion, also a convective heat transfer occurs (B).

4.4.5. Discussion

A slip sensor is intended to detect the occurrence or incipience of slip, although it may also provide additional information, such as slip speed and direction. The acknowledgement of the importance of slip sensors in prosthetic devices dates back to the 1970-80s [Childress, 1985]. Since then, the research effort spent on the field is steadily growing (Figure 4.1).

In the case of prosthetics applications it is desirable the sensor to be compact (small size and with few parts, for an easier integration), mechanically compliant (i.e. flexible or stretchable to better adapt to curved surfaces, such as fingertips), and robust against electrical and magnetic interferences, spurious vibrations (e.g. caused by moving mechanical parts), impacts, abrasion and wear.

Slip sensors are often integrated into curved and soft fingertips. In fact, it has been demonstrated that the use of compliant fingertips is beneficial for the effectiveness of grasping [Inoue, 2006; Inoue, 2007]. As it regards the response time, it should be smaller than that of the human sensors (i.e. <100 ms) regardless of the properties of the grasped object. This requirement arises from the need of allowing sufficient time to the prosthesis control to adapt grasp in a time window compatible with the generation of smooth, human-like motions. Finally, the sensor should not be too power demanding and costly.

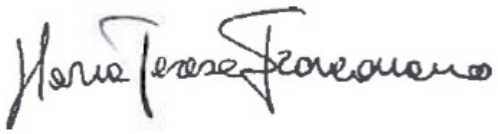

Even if the need of slip sensing has been addressed since the dawn of robotic manipulation, still there is not a dominant, well-established technology, and the existing ones do not meet all the above mentioned requirements.

For comparison purposes, in Tables 4.3 and 4.4 the main advantages/disadvantages of the reviewed technologies, together with their qualitative evaluation, are summarized.

The observation of the relative displacement of two surfaces in contact (e.g. object and fingertip), is probably the most intuitive approach for detecting the occurrence of slip. However, this strategy does not allow the detection of incipient slip, which, if timely detected, would at least theoretically enable the adaptation of grasping just before any undesired motion of the object occurs. Under this regard, vibrations-based sensors are probably the most promising, although quite complex.

Among vibrations transducers, piezoelectric materials are appealing, because they offer a direct transduction from the mechanical domain into the electrical domain, with minor wiring problems, quick response times and low power consumption. Unfortunately, their performance is affected by object surface properties (e.g. a high surface roughness helps vibrations generation), mechanical noise and damping effects due to the viscoelastic properties of the elastomeric materials usually employed as covers.

Also accelerometers look very promising for the development of incipient slip sensors. The tremendous advancement of MEMS technology in the last two decades made these devices extremely sensitive, compact, reliable and cheap.

As it regards other technologies (force sensors, photoelectric devices and acoustic transducers), a large amount of work should be devoted not just to the development of novel hardware but also to the development of efficient computational techniques able to manage in a very short time the large amount of data produced. The expected important side-benefit, especially in the case of multi-axis force sensor, is related to the capability of the sensor not only to detect (incipient) slip, but also to fully characterize interaction forces at the site of contact. This approach, in a sense, is more bioinspired than others.

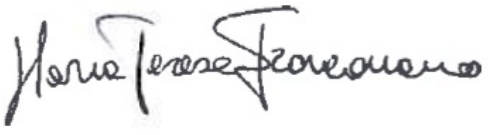

As explained in Chapter 2, the sense of slip in humans emerges from the combined analysis of a wealth of different tactile information, collected by several distributed sensors. One might expect that the investigation of artificial multimodal sensory fusion techniques, aiming at detecting incipient slip, may even shed light on some aspect of the neurophysiology of slip sensing in humans.

From a strict engineering viewpoint bioinspiration is not a must. For instance, slip sensors based on thermal phenomena (i.e. detection of convective heat transfer associated to slip) are based on a transduction principle exploited in several technical fields (e.g. hot wire anemometry) but not in nature. Such sensors, requiring a small but finite slip speed, are intrinsically not capable of detecting incipient slip. Nonetheless, they can be easily micro-manufactured using lithographic techniques. Since thermal capacity is directly proportional to mass, response time scales very positively with miniaturization, without any theoretical lower bound. One can expect that research in this field may lead to sensors responding in a few milliseconds (compared to the current 40-50 ms), a time short enough to make the displacement of the handled object before grasp regulation quite small.

In the following a qualitative comparison of different transduction strategies for slip detection is reported. It is based on the following performance indices:

- **Robustness**: evaluates the capability of detecting incipient slip rejecting external disturbances;
- **Integrability**: evaluates how simple the integration of the sensor on a robotic fingertip is. This parameter increases if the sensor can be manufactured using flexible or stretchable technologies and diminishes in case, e.g., complex wiring or high power are needed;
- **Simplicity**: increases if manufacturing process and/or computational demands are small.

Figure 4.6 shows two bidimensional projections of a 3D plot where the reviewed technological solutions for slip detection are qualitatively compared in terms of the three defined indices (Robustness, Integrability, Simplicity). Here, force and

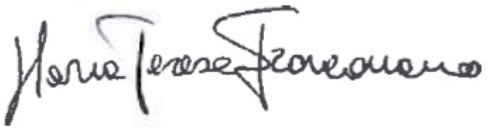

thermal sensors are considered to be the most promising for application in prosthetic hands.

Transduced physical slip-related quantity	**Transduction technology**	**Advantages**	**Disadvantages**
Displacement	Optical	Low cost components; Possibility of implementing learning procedures based on artificial vision	Bulky readout system; No incipient slip detection; Possible optical path occlusion
(Micro) Vibrations	Piezoelectric	Wide dynamic range; Good response time; Simple design	Sensibility and stability limited by technology; Possible damping by elastomeric materials (e.g. skin material); Performance depending from object surface finishing; Affected by external mechanical vibrations
	Acoustic		
	Piezoresistive		
	Photoelastic		
	Magnetic		
Forces	Capacitive	Good sensitivity; Wide dynamic range; additional information provided about object shape and contact conditions (forces/pressure)	Complex; Susceptible to noise
	Conductive elastomers		
	Piezoelectric		
	Piezoresistive		
	Strain gauge		
Heat transfer	Resistance temperature detectors (RTD)	Insensitive to object surface finishing; Robustness with respect to external noise (including mechanical vibrations); Easy manufacturability;	Slip occurrence is not distinguished from contact

Table 4.3. Main advantages and disadvantages of the reviewed slip sensors.

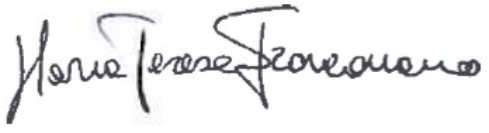

Transduced parameter	Power consumption	Compliance	Sensitivity to external noise	Manufacturability	Computational cost	Incipient slip detection
Displacement	**	-	*	**	***	-
Microvibrations	**	**	**	*	**	***
Forces	*	***	*	*	**	**
Thermal microflux	*	***	-	***	*	-

Table 4.4. Qualitative evaluation of slip sensors; symbols legend: '-': none '*': minor; '**': medium; '***': high.

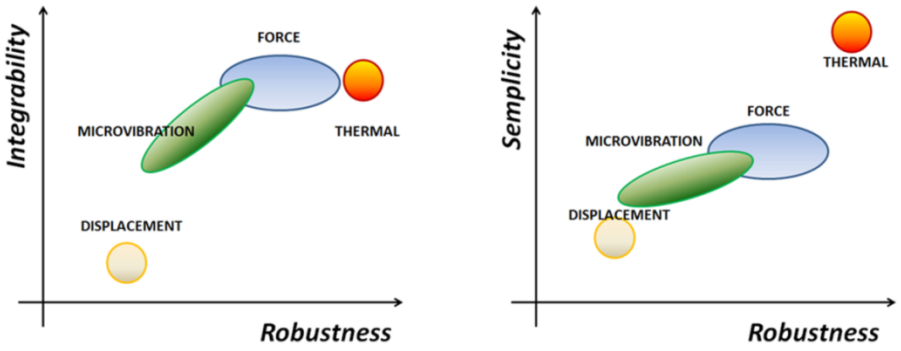

Figure 4.6: Comparison of slip detection strategies.

4.5. Artificial tactile skins

Artificial skins can be classified in three groups: *i)* fully-synthetic; *ii)* bio-hybrid; and *iii)* fully-biological [Lucarotti, 2013].

The first ones are based on MEMS technologies and are assembled in array configurations. Packagings used for these skins are mainly based on polymeric materials, such as silicone elastomers (e.g., polydimethylsiloxane, PDMS) and polyurethane rubbers (e.g., toluene diisocyanate and polyols) Lucarotti, 2013.

In bio-hybrid skins the transduction mechanism is demanded to synthetic sensors immersed in a bulk of biological/bio-engineered macromolecules and/or tissues. The biological component works as a packaging matrix, with no active role in the transduction. Some bio-hybrid devices include polymeric and elastomeric materials providing a substrate for cell adhesion and proliferation.

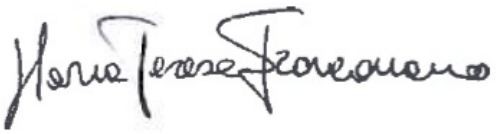

Polymers, such as polydimethylsiloxane (PDMS), polymethylmethacrylate (PMMA), polycarbonate, polyurethane and polyester, are often employed.

Fully-biological tactile sensors use biologically-grounded transduction mechanisms, with cells used as active elements [Lucarotti, 2013]. Although microfabricated systems provide an excellent platform for cell cultures and are useful for the investigation of cellular responses to various external stimuli [Lucarotti, 2013], currently the development of bioartificial receptors is far from maturity, and few successful attempts have been reported, such as those employing Merkel's cells [Fradette, 2003].

4.6. Conclusion

Dexterous manipulation capabilities are rooted in the sense of touch. Indeed, tactile receptors provide essential information regarding contact conditions.

The availability of such information would be of paramount importance for the user of a robotic prosthetic hand.

In order to amend the lack of a rich sensory feedback on prosthetic hands, especially in the detection of incipient slip, several types of sensors have been proposed over the years.

Most of existing slip sensors are still *i)* affected by external disturbances; *ii)* technologically demanding, *iii)* expensive; or *iv)* not embeddable on top of robotic finger pads.

Microtechnologies played a central role in enabling the development of novel components and devices, and in improving their performance, especially in terms of faster response, reduced complexity and encumbrance, and smaller cost.

The design of tactile sensors is often inspired by human detection/control mechanisms, which are multilevel and integrated: the fusion of sensory information from multiple sources is the key for a robust perception, as it maximizes the amount of information acquired from the (unstructured or unknown) environment.

For this reason, it is expected that in the near future we will assist to an increased interest to multimodal array of tactile sensors (including slip detectors), possibly

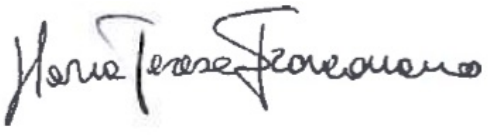

fabricated using compliant (flexible and/or stretchable) packagings [Kim, 2012; Sun, 2006], which can be better integrated into artificial skins. In particular, the heterogeneous nature of the human skin can be mimicked using multilayered structures, with each layer offering different mechanical properties (as the epidermis, dermis and subcuties in the skin), or a single non-homogeneuous layer with tuned parameters.

Another example of bioinspiration is demonstrated by the tendence of channeling the sensory information, possibly originated from neuromorphic sensors [Oddo, 2011], to a bidirectional neural interface, e.g. exploiting biohybridized microsystems. This solution will enlarge the reach of prosthetics towards the promises of bionics.

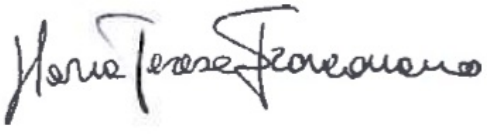

Bibliography

[Accoto, 2008] D. Accoto, et al., "A slip sensor for biorobotic applications using a hot wire anemometry approach", Sens. Actuators A, DOI:10.1016/j.sna.2008.07.030.

[Accoto, 2010] D. Accoto, M. Francomano, A. Benvenuto, C. Luccarelli, and E. Guglielmelli, "Optimization of a thermal slip sensor using FEM and dimensional analysis", in Proc. 3rd IEEE RAS/EMBS Int. Conf. Biomed. Robot. Biomechatronics, Tokyo, 2010, pp. 855-860.

[Agache, 1980] Agache P G, Monneur C, Leveque J L, and De Rigal J (1980) Mechanical properties and Young's Modulus of human skin in vivo. Archives of Dermatological Research 269: 221-232.

[Beccai, 2005] L. Beccai, et al., "Design and fabrication of a hybrid silicon three-axial force sensor for biomechanical applications", Sens. Actuators A, vol. 120, pp. 370-382, May 2005.

[Beccai, 2008] L. Beccai, et al., "Development and experimental analysis of a soft compliant tactile microsensor for anthropomorphic artificial hand", IEEE Trans. Mechatron., vol. 13(2), pp. 158–168, Apr. 2008.

[Chen, 2010] W. Chen, Y. Dong, and Y. Chen, "Experiment and research of a new tactile and slip sensor", Piezoelectrics and Acoustooptics, vol. 32 (4), pp. 571-577, 2010.

[Childress, 1985] D. S. Childress, "Historical aspects of powered limb prosthesis", Clin. Prosth. Orthot., vol. 9, pp. 2-13, 1985.

[Cotton, 2007] D. P. J. Cotton, P. H. Chappell, A. Cranny, N. M. White, and S. P. Beeby, "A novel thick-film piezoelectric slip sensor for a prosthetic hand", IEEE Sens. J., vol. 7(5), pp. 752-761, May 2007.

[Cotton, 2009] D. P. J. Cotton, I. M. Graz, and S. P. Lacour, "A Multifunctional Capacitive Sensor for Stretchable Electronic Skins", IEEE Sensors Journal, vol. 9 (12), pp. 2008-2009, December 2009.

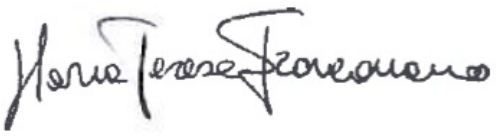

[Cranny, 2005] A. Cranny, D. P. J. Cotton, P. H. Chappell, S. P. Beeby, and N. M. White, "Thick-film force and slip sensors for a prosthetic hand", Sens. Actuators A, vol. 123–124, pp. 162–171, Sep. 2005.

[Cutkosky, 1989] M. R. Cutkosky, and R. D. Howe, "Sensing skin acceleration for slip and texture perception", in Proc. IEEE Int. Conf. Robot. Autom., Scottsdale, vol. 1, pp. 145–50, 1989.

[Dahiya, 2010] R. S. Dahiya, G. Metta, M. Valle, and G. Sandini, "Tactile Sensing—from Humans to Humanoids", IEEE Trans. Robot., vol. 26(1), pp. 1-20, Feb. 2010.

[Dario, 1996] P. Dario, R. Lazzarini, R. Magni, and S. R. Oh, "An integrated miniature fingertip sensor", in Proc. 7th Int. Symp. Micro Machine and Human Science, Nagoya, pp. 91-97, 1996.

[Dornfeld, 1987] D. Dornfeld, and C. Handy, "Slip detection using acoustic emission signal analysis", in Proc. IEEE Int. Conf. Robot. Autom., Raleigh, vol. 4, pp. 1868-1875, 1987.

[Dubey, 2006] V. N. Dubey, and R. M. Crowder, "A dynamic tactile sensor on photoelastic effect", Sens. Actuators A, vol. 128(2), pp.217–224, Apr. 2006.

[Engel, 2003] J. Engel, J. Chen, and C. Liu, "Development of polyimide flexible tactile sensor skin", J. Micromech. Microeng., vol. 13, pp. 359-366, May 2003.

[Engel, 2005] J. Engel, J. Chen, Z. Fan, and C. Liu, "Polymer micromachined multimodal tactile sensors", Sens. Actuators A, vol. 117(1), pp. 50-61, Jan. 2005.

[Fishel and Loeb, 2012] J. A. Fishel and G. E. Loeb, "Bayesian exploration for intelligent identification of textures", Front. Neurorob., vol. 6(4), pp. 1-20, June 2012.

[Fradette, 2003] Fradette, J.; Larouche, D.; Fugere, C.; Guignard, R.; Beauparlant, A.; Couture, V.; Caouette-Laberge, L.; Roy, A.; Germain, L. Normal human Merkel cells are present in epidermal cell populations isolated and cultured from glabrous and hairy skin sites. J. Invest. Dermatol. 2003, 120, 313–317.

[Francomano, 2012] M. Francomano, D. Accoto, E. Morganti, L. Lorenzelli, and E. Guglielmelli, "A microfabricated flexible slip sensor", in Proc. 4th IEEE RAS/EMBS Int. Conf. Biomed. Robot. Biomechatronics, Roma, 2012, pp. 1919-1924.

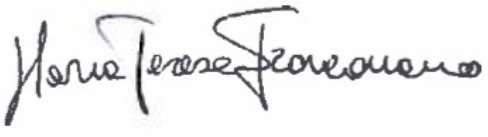

[Fujimoto, 2003] I. Fujimoto, Y. Yamada, and T. Maeno, "Development of artificial finger skin to detect incipient slip for realization of static friction sensation", in Proc. IEEE Multisensor Fusion and Integration for Intelligent Systems, Tokyo, pp. 15-21, 2003.

[Gofuku, 2000] A. Gofuku, Y. Tanaka, and J. Tsubot, "Development of a flexible artificial hand system equipped with a slip sensor", JSME Int Journal. Ser C. Mech Systems, Mach Elem Manuf., vol. 43(2), pp.378-386, 2000.

[Hackwood, 1983] S. Hackwood, G. Beni, L. A. Hornak, R. Wolfe, and T. J. Nelson, "A torque-sensitive tactile array for robotics", Int. J. Robotics Res., vol. 2(2), pp. 46–50, June1983.

[Ho, 2011] V. A. Ho, D. V. Dao, S. Sugiyama, and S. Hirai, "Development and analysis of a sliding tactile soft fingertip embedded with a microforce/moment sensor", IEEE Trans. Robot., vol. 27(3), pp. 411-424, June 2011.

[Holweg, 1996] E. G. M., Holweg, et al., "Slip detection by tactile sensors: algorithm and experimental results", in Proc. IEEE Int. Conf. Robot. Autom., Minneapolis, vol. 4, pp. 3234–3239, 1996.

[Hopkins, 1992] S. H. Hopkins, F. Eghtedari, and D. T. Pham, "Algorithms for processing data from a photoelastic slip sensor", Mechatronics, vol. 2(1), pp. 15-28, Feb. 1992.

[Hosoda, 2002] K. Hosoda, Y. Tada, and M. Asada, "Internal representation of slip for a soft finger with vision and tactile sensors", in Proc. IEEE/RSJ Int. Conf. Intell. Robots Syst., Lausanne, vol. 1, pp. 111-115, 2002.

[Hosoda, 2006] K. Hosoda, Y. Tada, and M. Asada, "Anthropomorphic robotic soft fingertip with randomly distributed receptors", Robot. Auton. Syst., vol. 54, pp. 104-109, Feb. 2006.

[Howe, 1993] R. D. Howe, and M. R. Cutkosky, "Dynamic tactile sensing: perception of fine surface features with stress rate sensing", IEEE Trans. Robot. Autom., vol. 9(2), pp. 140–151, Apr. 1993.

[Inoue, 2006] T. Inoue, and S. Hira, "Elastic model of deformable fingertip for soft fingered manipulation", IEEE Trans. Robot., vol. 22(6), pp. 1273–1279, Dec. 2006.

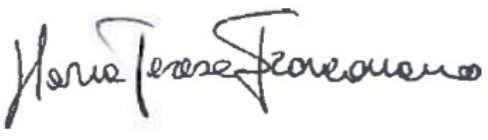

[Inoue, 2007] T. Inoue, and S. Hirai, "Dynamic stable manipulation via soft-fingered hand", in Proc. IEEE Int. Conf. Robot. Autom., Roma, pp. 586–591, 2007.

[Ikeda, 2004] A. Ikeda, Y. Kurita, J. Ueda, Y. Matsumoto, and T. Ogasawara, "Grip force control for an elastic finger using vision-based incipient slip feedback", in Proc. IEEE/RSJ Int. Conf. Intell. Robots Syst., Sendai, vol. 1, pp. 810-815, 2004.

[Jaffe, 1971] B. Jaffe, W. Cook, H. Jaffe, et al., Piezoelectric Ceramics, vol. 1, Academic Press, London, 1971.

[Johansson and Westling, 1984] R. S. Johansson, and G. Westling, "Roles of glabrous skin receptors and sensorimotor memory in automatic control of precision grip when lifting rougher or more slippery objects", Exp Brain Res., vol. 56, pp. 550–564, Oct. 1984.

[Kim, 2012] D. H. Kim, R. Ghaffari, N. Lu, and J. A. Rogers, "Flexible and Stretchable Electronics for Biointegrated Devices", Annu. Rev. Biomed. Eng., vol. 14, pp. 113-128, Aug. 2012.

[Kyberd, 1992] P. J. Kyberd, and P. H. Chappell, "Characterization of an optical and acoustic touch and slip sensor for autonomous manipulation", Meas. Sci. Technol., vol. 3, pp. 969-975, Oct. 1992.

[Kyberd, 1993] P. J. Kyberd, and P. H. Chappell, "A force sensor for automatic manipulation based on the Hall effect", Meas Sci Technol., vol. 4, pp. 281-287, March 1993.

[Lipomi, 2011] D. J. Lipomi, M. Vosgueritchian, B.C-K. Tee, S. L. Hellstrom, J. A. Lee, C. H. Fox, and Z. Bao, "Skin-like pressure and strain sensors based on transparent elastic films of carbon nanotubes", Nature Nanotechnology, vol. 6, pp. 788- 792, December 2011.

[Lowe, 2010] R. J. Lowe, P.H. Chappell, and S.A. Ahmad, "Using accelerometers to analyze slip for prosthetic application", Meas Sci Technol., vol. 21(3), 035203(7pp), March 2010.

[Lucarotti, 2013] C. Lucarotti, C. M. Oddo, N. Vitiello, and M. C. Carrozza, "Synthetic and Bio-Artificial Tactile Sensing: A Review", Sensors, 13, 1435-1466, 2013.

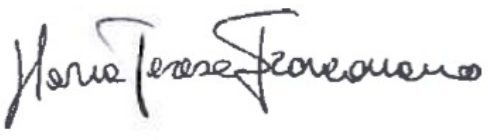

[Maeno, 1998] T. Maeno, K. Kobayashi, and N. Yamazaki, "Relationship between the structure of human finger tissue and the location of tactile receptors", Bull. JSME Int. J., vol. 41(1), pp. 94–100, 1998.

[Mannsfeld, 2010] S. C. B. Mannsfeld et al., "Highly sensitive flexible pressure sensors with microstructured rubber dielectric layers", Nature Materials, 9,pp.859–864, 2010.

[Manschot and Brakkee, 1986]Manschot J F M, and Brakkee A J M (1986) The measurement and modelling of the mechanical properties of human skin in vivo-I. The measurement. Journal of Biomechanics 19: 511-515.

[Mazzeo, 2012] A. D. Mazzeo, W. B. Kalb, L. Chan, M. G. Killian,J.-F. Bloch, B. A. Mazzeo, and G. M. Whitesides, "Paper-Based, Capacitive Touch Pads", Adv. Mater. 2012, 24, 2850–2856.

[Melchiorri, 2000] C. Melchiorri, "Slip Detection and Control using tactile and force sensors", IEEE/ASME Trans. Mechatron., vol. 5(3), pp. 235-243, Sep. 2000.

[Mittendorfer, 2011] P. Mittendorfer, and G. Cheng, "Humanoid multimodal tactile-sensing modules", IEEE Trans. Robot., vol. 27(3), pp. 401-410, June 2011.

[Monkman, 1993] G. J. Monkman, and P. M. Taylor, "Thermal tactile sensing", IEEE Trans. Robot. Autom., vol. 9(3), pp. 313–318, June 1993.

[Najarian, 2009] S. Najarian, J. Dargahi, A. Mehrizi, Artificial Tactile Sensing in Biomedical Engineering, McGraw-Hill Biophotonics, McGraw-Hill, 2009.

[Nishihara, 1996] K. Nishihara, S. Komiya, N. Okuma, and H. Otsuka, "Slip sensor using a piezoelectric bimorph element", Trans. JSME C., vol. 62(598), pp. 2244-2249, 1996.

[Oddo, 2011] C. Oddo, et al., "Roughness encoding in human and biomimetic artificial touch: spatiotemporal frequency modulation and structural anisotropy of fingerprints", Sensors, vol. 11(6), pp.5596-5615, May 2011.

[Pang, 2012] C. Pang, G.-Y. Lee, T. Kim, S. M. Kim, H. N. Kim, S.-H. Ahn, and K.-Y. Suh, "A flexible and highly sensitive strain-gauge sensor using reversible interlocking of nanofibres", DOI: 10.1038/NMAT3380, 2012.

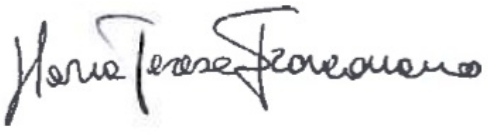

[Quilliam, 1978] T. A. Quilliam, "The structure of fingerprint skin," in Active Touch: The Mechanisms of Recognition of Objects by Manipulation, G. Gordon, Ed. London, U.K.: Pergamon, 1978, pp. 1–18.

[Russell, 1985] R. A. Russell, "A thermal sensor array to provide tactile feedback for robots", Int. J. Robotics Res., vol. 5(3), pp. 35–39, Sep. 1985.

[Shinoda, 2000] H. Shinoda, S. Sasaki, and K. Nakamura, "Instantaneous evaluation of friction based on ARTC tactile sensor", in Proc. IEEE Int. Conf. Robot. Autom., San Francisco, vol. 3, pp. 2173-2178, 2000.

[Skoog, 1985] D. Skoog, D. West, Principles of Instrumental Analysis, vol. 4, Saunders College Publishing, New York, 1985.

[Sun, 2006] Y. Sun, W. M. Choi, H. Jiang, Y. Y. Huang, and J. A. Rogers, "Controlled buckling of semiconductor nanoribbons for stretchable electronics", Nature Nanotech., vol. 1, pp. 201.-207, Dec. 2006.

[Teshigawara, 2011] S. Teshigawara, T. Tsutsumi, S. Shimizu, Y. Suzuki, A. Ming, M. Ishikawa, and M. Shimojo, "Highly sensitive sensor for detection of initial slip and its application in a multi-fingered robot hand", in Proc. IEEE Int. Conf. Robot. Autom., Shanghai, pp. 1097-1102, 2011.

[Tiwana, 2012] M. I. Tiwana, S. J. Redmond, and N. H. Lovell, "A review of tactile sensing technologies with applications in biomedical engineering", Sens. Actuators A, vol. 179, pp. 17-31, June 2012.

[Tremblay, 1993] M. R. Tremblay, and M. R. Cutkosky, "Estimating friction using incipient slip sensing during a manipulation task", Atlanta, in Proc. IEEE Int. Conf. Robot. Autom., vol. 1, pp. 429–434, 1993.

[Valdastri, 2005] P. Valdastri, et al., "Characterization of a novel hybrid silicon three-axial force sensor", Sens. Actuators A, vol. 123-124, pp. 249-257, Sep. 2005.

[Video-tape on SRI Sensor Research, 1986] Video-tape on SRI Sensor Research, ACE Instructional Network, Menlo Park, CA, Sep. 1986.

[Wang, 2009] Y. Wang, and J. Chen, "Research of touch-slide sensor based theory of acoustic", Chin. J. Sens. Actuators, vol. 22(12), pp. 1701-1703, 2009.

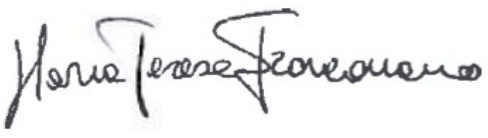

[Wettels, 2008] N. Wettels, V. J. Santos, R. S. Johansson, and G. E. Loeb, "Biomimetic tactile sensor array", Adv. Robot., vol. 22(7), pp. 829–849. 2008.

[Wettels, 2009] N. Wettels, A. R. Parnandi, J.-H. Moon, G. E. Loeb, and G. S. Sukhatme, "Grip control using biomimetic tactile sensing systems", IEEE/ASME Trans. Mechatron., vol. 14(6), pp. 718-723, Dec. 2009.

[Window, 1992] A. Window, Strain Gauge Technology, Springer, 1992.

[Yamada, 2002] D. Yamada, T. Maeno, and Y. Yamada, "Artificial finger skin having ridges and distributed tactile sensors used for grasp force control", J. Robot. Mechatron., vol. 14(2), pp. 140–146, Oct. 2002.

[Yuan, 2001] L. Yuan, "A novel fiber-optic slide-sensing scheme", Optical Fiber Technology, vol. 7(4), pp. 340-349, Oct. 2001.

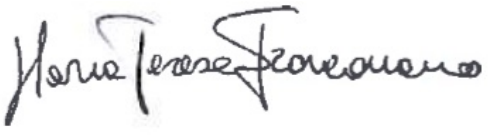

Chapter 5

Flexible sensors for prosthetic hands[8]

As discussed in the previous Chapter, despite the wide variety of technological solutions for tactile sensors, often their application to hand prostheses is hindered by integration-related issues.

Currently most of tactile sensors present in robotic hands are embedded in the mechanical case of fingers or of the palm.

However, in some cases it is required the sensor to be in contact with the manipulated object, as it happens, for example, for the thermal slip sensor presented in section 4.4.4; in other cases it is necessary to integrate the sensing elements into covering gloves or skins, which usually are made of elastic materials.

In the examples above it is highly desirable that the tactile sensors can be freely bent without any negative effects on their performance. Indeed, flexibility would allow their folding around the surface of robotic devices.

Recent advances in materials and manufacturing technologies enabled the development of *flexible* microdevices, which are light weight, with reduced package sizes and good mechanical reliability during deformations.

[8]This work has been partly published by the author (*M. T. Francomano, D. Accoto, and E. Guglielmelli, "Experimental characterization of a flexible thermal slip sensor", Sensors, 12(11), 15267-15280, 2012*; paper n.2 of *List of Publications*).

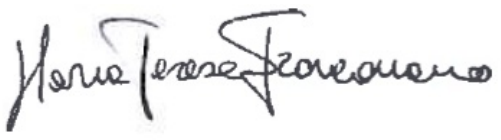

Such devices are usually ultrathin, with the active parts embedded between two polymeric layers (e.g. polyimide), resulting in a cheap package with a total thickness usually not exceeding 100 um.

The application fields of such technology are multiple, including: automotive, computers and consumer electronics, aerospace and defense, telecommunication, and medical (implantable) instruments.

Flexible, skin-like electronic sensors have been introduced for robotic applications, based on various transduction principles, such as mechanical, chemical, thermal and optical, with multiscale architectures [Engel, 2003; Engel, 2005; Mannsfeld, 2010; Lipomi, 2011; Francomano, 2012; Pang, 2012].

5.1. Flexible technologies and materials

Since 1970s, when advancements of semiconductor processing allowed the development of $2D^{1/2}$ and 3D microgeometries [Senturia, 2001; Madou, 2002], the microsystems arena has evolved extensively.

The predominant substrate material was silicon, whereas the most used thin film surface was silicon dioxide (mainly employed in the MOS process). Anyhow, over the years, other materials (e.g. compound semiconductors [Adachi, 1983; Zhang, 1993], diamond [Shibata, 2000; Wur, 1995; Zhu, 2004] and ceramics [Fonseca, 2002; Chen, 2001]) have been tested.

Starting from 1990s, polymer materials have been increasingly used for microsystems development [Liu, 2010], mainly for the following motivations:

- they can sustain larger deformations than silicon;

- many polymer materials, as well as their fabrication processes, are inexpensive, with most processes do not requiring cleanrooms;

- they allow to enlarge the standard portfolio of microfabrication processes to new ones, including casting and molding, embossing [Shen, 2002; Cui, 2005], spraying, screen printing, thick film processing [Yoon, 2006].

Polymer materials have been used for flexible technologies as substrates, structural/functional thin films, coatings and for compliant packaging [Kim, 2001].

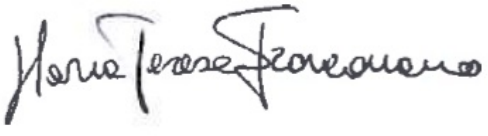

To make the structure flexible, all components must accommodate bending to some degree without losing their function. To this aim, two basic approaches have been pursued [Fjelstad, 2011]:

1. transfer and bonding of completed rigid circuits on a flexible substrate;

2. fabrication of the circuits directly on the flexible substrate.

During the design phase, it is important to consider the flexibility limitations of the device not only for the final product geometry and functional life, but also for all prior assembly, adjustment, and repair procedures to avoid yielding problems and functional life failures [Fjelstad, 2011].

Several materials combinations of thinned rigid substrates (e.g. silicon or glass) or plastic films with metal/polymer foils and/or adhesives have been used.

The main substrates employed are [Fjelstad, 2011]:

- Fluoropolymer films, such as Teflon®;
- Aramid fiber-based papers and cloths, such as Nomex®;
- Formable composites, such as those represented by Bend/Flex®;
- Various flexible epoxy-based composites;
- Thermoplastic films, such as polyethylene, polyvinyl chloride, polyvinyl fluoride, and polyetherimide;

The most commonly used ones as flexible base materials are polyester (PET) and polyimide (PI).

In particular, polyimide films exhibit good reliability, excellent flexibility at all temperature and chemical resistance (with the exception to hot alkaline solutions). Moreover, polyimide shows good electrical properties and tear resistance [Fjelstad, 2011]. Trade names includes: Kapton®, Apical® and Upilex®.

5.2. A thermal slip sensor

Taking into account the state of the art of flexible technologies, and considering the outcomes of the review of current slip sensors for prosthetic hands (Chapter 4), a miniaturized thermal slip sensor has been developed on a flexible substrate to be easily integrated on robotic finger pads.

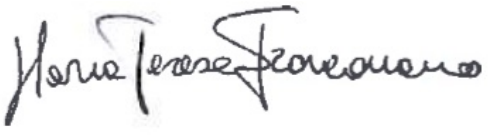

The sensor described in the following has no moving parts and exploits a thermo-electrical transduction principle [Accoto, 2008], briefly outlined in section 5.2.1. Since the sensor does not rely on the detection of vibrations, mechanical noise, e.g. produced by motors, does not affect its performance. Moreover, it is equally effective on rough and smooth objects.

Starting from an existing rigid prototype [Accoto, 2008] (section 5.2.2), whose design has been optimized [Accoto, 2010], as reported in section 5.2.3, a flexible sensor has been developed, as detailed in section 5.2.5 [Francomano, 2012; Francomano, 2012b]. The characterized flexible prototype has been then further miniaturized and arranged in an array design with the final aim of developing a sensor capable of detecting not only the occurrence of slip, but also its direction, as it would be useful for adequately adapting the configuration of the robotic fingers. The control algorithm, implemented for the array, is detailed in section 5.3.

Finally, aiming at integrating the readout electronics on the same substrate of the sensing elements, a design optimization study has been performed for developing flexible devices using thinned silicon as substrate (Section 5.4).

5.2.1. Working principle

The sensing element of the thermal slip sensor is a patterned thin metal film with a positive thermal coefficient (α), working as a microheater. The metal film is warmed up by Joule effect.

By measuring its electrical resistance (R), direct information on its temperature (T) can be retrieved without the need for a dedicated temperature sensor, by inverting the following equation (R_0 is the resistance at the reference temperature, T_0):

$$R(T)=R_0+[\alpha(T-T_0)] \quad (5.1)$$

The microheater is kept at a constant temperature by a dedicated control. When the sensor is in contact with an object with zero relative speed (v=0, no slip condition), only heat conduction occurs, according to Fourier's law:

$$\partial T/\partial t=k\nabla^2 T+q(x) \quad (5.2)$$

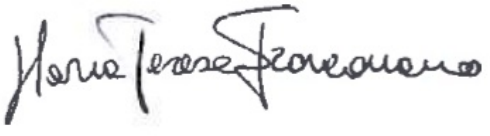

where q(x) is the power generation term (Joule effect), and k is the thermal diffusivity [m^2/s], defined by:

$$k=K/(C_p\rho) \tag{5.3}$$

In eq. (5.3) K, C_p and ρ respectively are the thermal conductivity [W/m K], the specific heat [J/kg K] and the density [kg/m^3] of the medium through which heat conduction occurs. If a slip event occurs ($v\neq0$), a convective heat transfer term ($\mathbf{v}\cdot$grad T) adds to the left member of eq. (5.2):

$$\partial T/\partial t+\mathbf{v}\cdot\text{grad}T=k\nabla^2T+q(x) \tag{5.4}$$

The additional convective term requires a higher current to keep the microheater at the desired temperature. The slip detection strategy consists in firing a signal whenever such current overcomes a threshold.

It is therefore evident that the proposed detection strategy is inherently incapable of detecting slip incipience: a finite slip velocity is indeed necessary to build up a convective heat transfer term, responsible for the increase of the absorbed current.

Nonetheless, it is possible to demonstrate that the sensitivity of the sensor to slip velocity is maximum for very small velocities, because the additional convective term quickly increases when slip velocity goes from zero to a given finite value (section 5.2.3.4.).

5.2.2. The rigid prototype

A schematic (not to scale) of sensor structure is shown in Figure 5.1.

The active element is a planar gold resistor (gold temperature coefficient is $0.0034°C^{-1}$ [Serway, 1998]). The sensor includes four connections: two for measuring the voltage drop across the micro-heater and two for applying the current. The widths of the two sets of leads are different: the two outer leads, used for supplying current, are wider than the inner ones, used for sensing. Hence, a reduced voltage drop occurs across the powering leads.

Electrical parts have been fabricated on a glass substrate (25 mm×25 mm, 960 um thick) and the microheater has been patterned implementing a standard lift-off process (Figure 5.2).

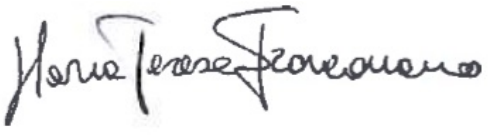

The deposited thin metal films are Cr (5 nm), used as adhesion layer, and Au (16 nm). The electrical contacts, patterned implementing a second lift-off process, consist of a 10 nm of Ti, as adhesion layer, a 100 nm of Au, and 20 nm of Ti oxide as protective layer.

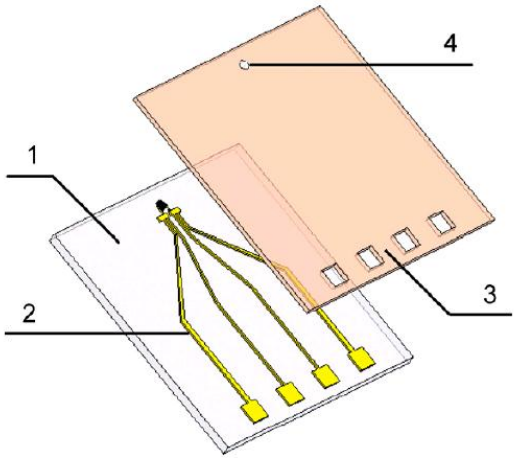

Figure 5.1: Schematic of the slip sensor. 1: glass substrate; 2: electrical parts; 3: protective layer; 4: contact layer [Accoto, 2008].

The two-step lift-off process, which gives the heater a lower thickness, together with the choice of developing larger widths for the powering leads, give the microheater a higher electrical resistance compared to that of the electrical connections. In this way a lower voltage drop occurs across the leads.

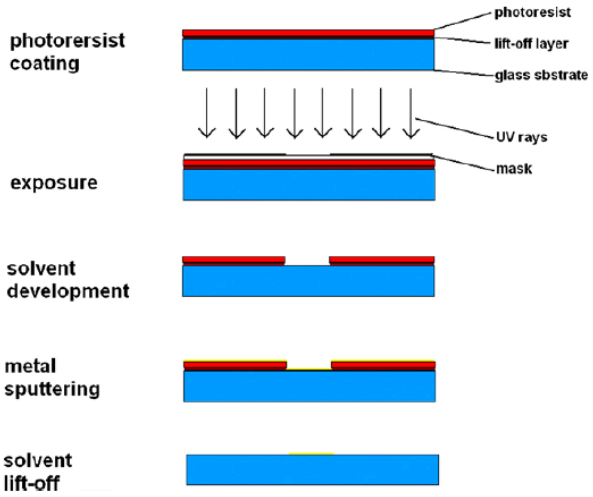

Figure 5.2: Steps of the lift-off process [Accoto, 2008].

Maria Teresa Francomano

The electrical parts have been covered by a layer of polyimide (10 um thick; PI 2731, from HD MicroSystems TM), while the pads have been opened by implementing a photolithographic process.

Finally, a cyanoacrylate glue drop (1mm wide and 40um tick) has been deposited over the microheater with a twofold function: 1. to increase the mechanical resistance of the sensor against wear; 2. to localize the thermal contact with the object over the resistor.

A photo of the resulting device is in Figure 5.3.

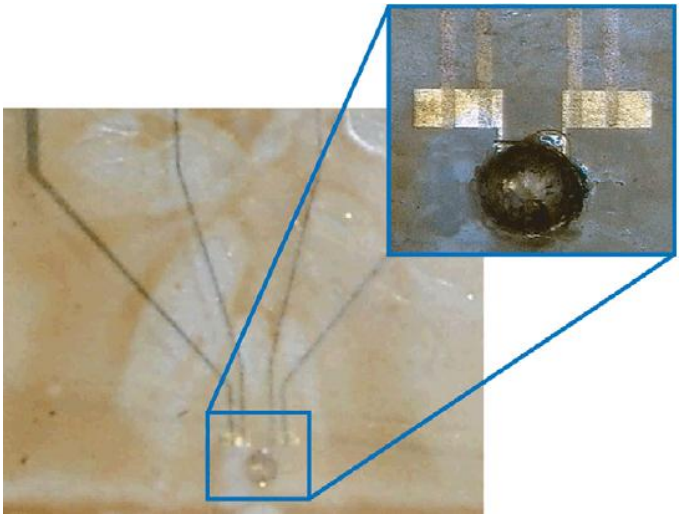

Figure 5.3: Snapshot of the fabricated slip sensor [Accoto, 2008].

The sensor has been characterized using a control system consisting of two external electronic circuits and a National Instruments DAQ card E6062 connected to a PC (Figure 5.4).

One of the external circuits is for generating a constant current, proportional to an input voltage provided by the DAQ analog output (AO).

This current is the one is used to warm up the resistor. Note that, given that the current supplied to the sensor is known, the resistance can be calculated as R=V/I, where V is the measured voltage drop. Electrical resistance can then be converted into a temperature according to eq. (5.1).

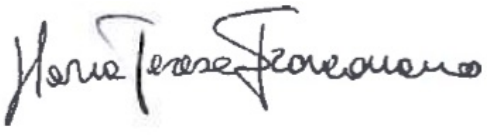

The other external circuit is a differential amplifier that converts the measured voltage from the sensor to a voltage within the limits of the DAQ analog input (AI) (+10 V and −10 V) and also separates the device from the ground of the DAQ.

An Agilent E3634A power supply provides power for both of the circuits.

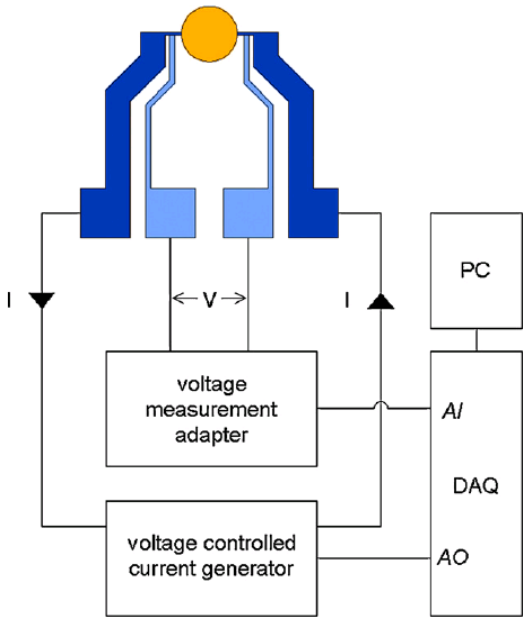

Figure 5.4: Control scheme of the rigid slip sensor [Accoto, 2008].

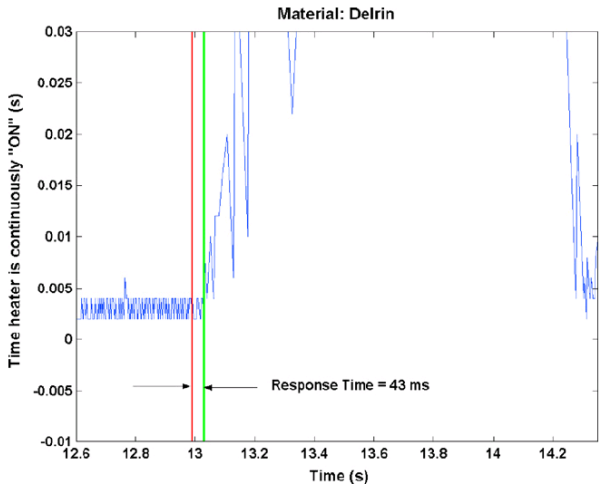

Figure 5.5: Sensor response time. The test has been performed using a bar of delrin [Accoto, 2008].

An example of obtained results during experiments is reported in Figure 5.5, where the red line refers to the time a bar starts slipping and the green line refers

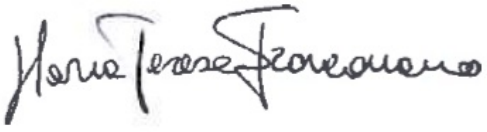

to the time when the sensor detect the slip event. The time difference between the two lines indicates the sensor's response time.

The average response time obtained using as sampling period 6 ms is 154 ms, while by sampling with a period of 2 ms, the average response time drops to 68 ms.

5.2.3. Optimization design

As detailed in section 2.2, the tactile information provided to the human NS elicits the motor response, leading to the adaptation of forces, in less than 100ms.

To equal such performance, we must take into account the computation time necessary to adapt the grasp of the robotic fingers. Therefore, the target slip detection time should be sufficiently smaller than 100 ms. The target value of 50 ms has been selected as appropriate.

A model-based analysis of the thermal slip sensor has been performed [Accoto, 2010] for optimizing both sensor geometry and materials in order to increase the heat flux and thereby to obtain a reduction of sensor response times in the identification of slip.

The optimization requires a model of the heat transfer associated to object movements (Q_c). To this aim, an analytical model, where unknown parameters have been determined using FEM analysis, has been developed (Sections 5.2.3.1-5.2.3.4). A sensitivity analysis performed on the model led to the definition of the optimal geometry and materials choice, with special regard to the contact layer, which greatly influences the performance of the sensor (Section 5.2.3.5).

5.2.3.1.Geometrical model

Some geometrical simplifications have been made with respect to the structure of the sensor reported in Figure 5.1, in order to reduce the computational cost of the model, while preserving its accuracy.

By considering the small thickness of the layers, compared to their longitudinal extension (about 1:1000), each layer can be approximated to a plane, with heat flowing perpendicularly to it.

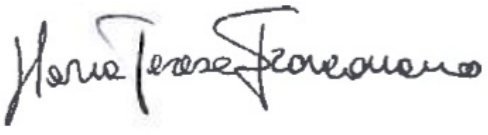

Moreover, the heat flow through the glass substrate, being constant (57.34 mW, [Accoto, 2008]), can be neglected, and simulations can be focused on the analysis of the heat flow from the isothermal resistor surface to the object surface.

The contact layer, made in cyanoacrylate, has been modeled as a 40 μm thick cylinder, with radius 0.5 mm.

In Table 5.1 geometrical data of the different layers are reported.

Layer	**Material**	**Shape**	**Dimensions**
Substrate	Glass	Square	12x12x1 mm^3
Protective	Polyimide	Square	12x12x0.01 mm^3
Heating	Gold	Square	1x1 mm^2
Contact	Cyanocrilate	Cylinder	R=0.5 mm Thickness=40 μm
Moving bars	Polystirene Delrin Teflon Pine Wood	Rectangle	15x12x2 mm^3

Table 5.1: Sensor layers geometrical data.

5.2.3.2. FEM Thermal Analysis

A FEM thermal analysis has been carried out in stationary conditions, with a convective term added to the outer surface of the protective layer. Such analysis allows calculating the heat flux from the sensor to the touched object.

FEM simulations have been carried out by considering the touched object made out of four different materials (Polystirene, Delrin, Teflon and Pine Wood). Slip speeds from 5 mm/s up to 70 mm/s have been considered.

The results of FEM simulations are shown in Figure 5.6, where power versus slip velocity is reported for the four materials taken into consideration.

5.2.3.3. Dimensional Analysis

Figure 5.6 shows that, as expected, the thermal power exchanged with the touched object, depends on the thermal properties of the object itself.

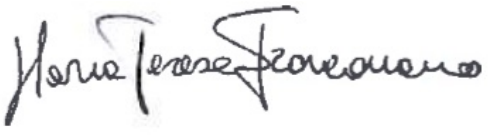

In order to obtained analytical expressions, that can be better handled for optimization purposes, dimensional analysis has been used to relate the convective thermal flux Q_c to K (thermal conductivity), S (surface), ΔT (temperature drop between contact layer and touched object), ρ (object density), C_p (specific heat) and v (slip speed).

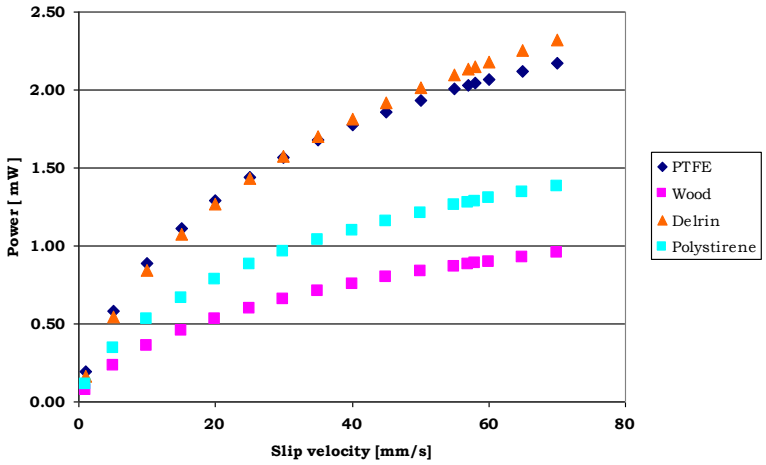

Figure 5.6: FEM simulations relating the power dissipation and different slip speeds.

Buckingham's theorem assures that the thermal problem can be described by means of 3 dimensionless groups, since the 7 above-listed thermal and geometric parameters can be expressed in terms of four fundamental quantities: M (mass), L (length), T (time), K (temperature).

Moreover, by considering that the simulations shown in Figure 5.7 indicate a quadratic relation between slip velocity and power and that the heat flux is directly proportional to ΔT, one gets:

$$Q_c = A\, S^{3/4}\, \Delta T \sqrt{v\, K\, \rho\, C_p} \tag{5.5}$$

where A is an (unknown) dimensionless coefficient. By introducing the *thermal diffusivity*, α, eq. (5.5) can be expressed as follows:

$$Q_c = A\, S^{3/4}\, K\, \Delta T \sqrt{\frac{v}{\alpha}} \tag{5.6}$$

Maria Teresa Francomano

The value of A can be easily obtained by fitting of FEM simulations data. To this aim, the Fourier number (F_o), given in (5.7), has been taken into account. F_o is a dimensionless group obtained from the product of the time and the thermal diffusivity, divided by the heat flux surface:

$$F_o = \frac{\alpha}{R\, v} \tag{5.7}$$

By fitting the power values in Figure 5.6 with eq. (5.6), and expressing the parameter A in terms of $1/F_o$, one gets the plot reported in Figure 5.7.

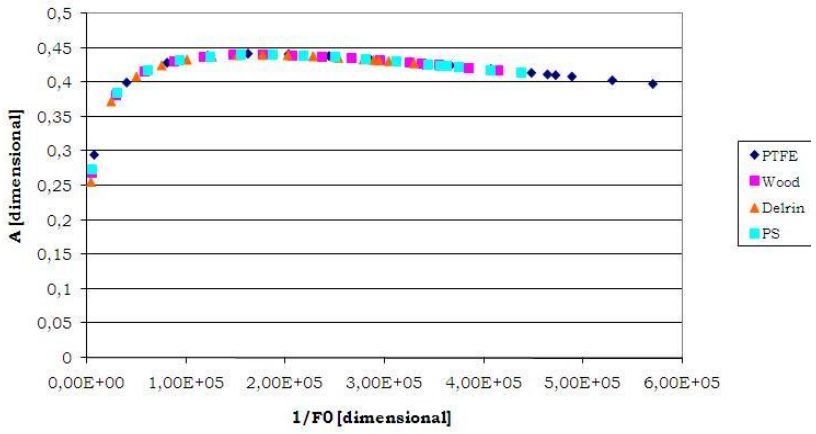

Figure 5.7: Relation between A and $1/F_o$.

The graph in Figure 5.8 shows that for speeds below 0.02 m/s A is variable, while for higher speeds it is nearly constant for all materials. Moreover, a good linear fitting between A and $1/F_o$ can be found in the slip speed range between 35 and 70 mm/s, as shown in Figure 5.8.

The linear interpolation of A can be inserted in (5.6), which in turn can be used to determine the thermal resistance, R_h, associated to the convective heat flux from the contact layer to the touched object:

$$R_h = \frac{\Delta T}{Q_c} \tag{5.8}$$

As it regards conduction, the heat generated by the resistor encounters two serial thermal resistances, represented by the contact layer (R_{cont}) and the protective layer (R_{prot}).

Maria Teresa Francomano

Because of the small dimensions, the thermal capacitances of the layers of the sensors are about three orders of magnitude smaller than the thermal capacitance of the touched object. This allows the development of a thermal model comprising only thermal resistances.

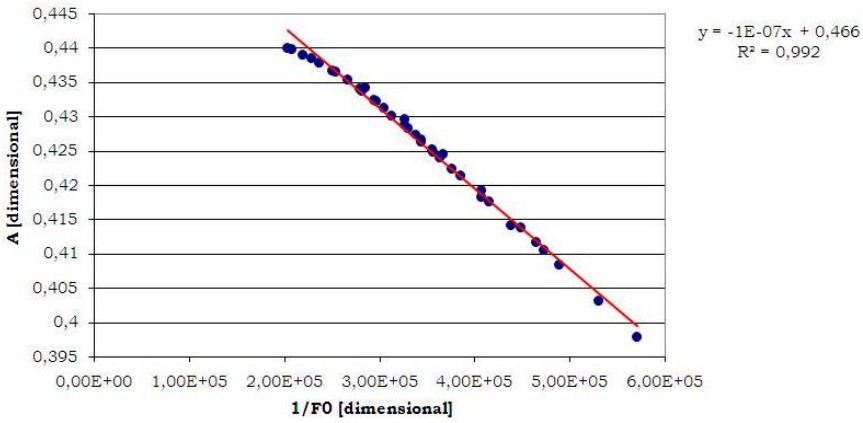

Figure 5.8: Linear relation between A and $1/F_o$.

Since the thermal resistances are in series, we have:

$$R_{TOT} = R_h + R_{cont} + R_{prot} = \frac{\sqrt{\alpha}}{\frac{A}{F_o} K S^{3/4}\sqrt{v}} + \frac{\delta_{cont}}{k_{cont} S_{cont}} + \frac{\delta_{pi}}{k_{prot}} \quad (5.9)$$

Finally eq. (5.10) allows calculating the analytical expression for the total heat flux (Q^*), simply given by:

$$Q^* = \frac{\Delta T^*}{R_{TOT}} \quad (5.10)$$

where ΔT^* is the temperature difference between microheater and touched object.

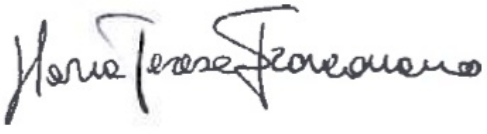

5.2.3.4. Thermal model

As mentioned in section 5.2.1, the thermal slip sensor is unable to detect incipient slip: a finite slip velocity is indeed necessary to build up a convective heat transfer term, responsible for the increase of the absorbed current.

According to (5.6), it is possible to demonstrate that the sensitivity of the sensor to slip velocity is maximum at very small velocities, because the additional convective term quickly increases when slip velocity goes from zero to a given finite value.

Let consider the sensitivity of Q_c to slip velocity ($\partial Q_c/\partial v$) is singular when v=0:

$$\partial Q_c/\partial v = A\, S^{3/4} \rho C_p \Delta T/2\sqrt{v/\alpha} \qquad (5.11)$$

In conclusion, although the sensor is not capable of detecting incipient slip, its responsiveness at low slip speeds is just limited by the resolution of the readout electronics used to calculate T through the measure of R, according to (5.1), being the additional convective term very sensitive to slip speed during the very initial instants of slip occurrence.

5.2.3.5. Sensitivity Analysis

The thermal model developed in Sections 5.2.3.3 and 5.2.3.4 provides the starting point for the design of the optimized sensor. In particular, the analytical expressions allow carrying out a sensitivity analysis with regards to the following parameters:

- Area of the contact layer;
- Thickness of the contact layer;
- Thermal conductivity of the contact layer;
- Surface of the protective layer;
- Thickness of the protective layer;
- Thermal conductivity of the protective layer.

The sensitivity of a quantity f_i with regards to parameter x_i is defined as:

$$S_i = \frac{\partial f_i}{\partial x_i}\frac{x_i}{f_i}$$

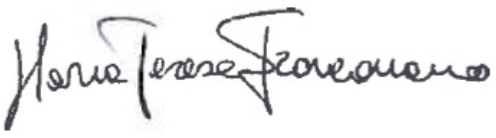

The sensitivity analysis aims at pointing out the parameters to which thermal flux is maximally sensitive. The analysis performed has shown that the parameters which mainly influence Q^* are: the contact layer surface (S), thickness (δ) and thermal conductivity (k), as reported in Table5.2.

Parameter	Sensitivity (adimensional)
Contact layer surface	1
Contact layer thickness	$-9\ 10^{-2}$
Contac layer thermal conductivity	$5\ 10^{-2}$
Protective layer surface	$8\ 10^{-2}$
Protective layer thickness	$-4\ 10^{-2}$
Protective layer thermal conductivity	$5\ 10^{-2}$

Table 5.2: Sensitivity analysis outcomes.

A higher sensitivity on thermal conductivity leads to the choice of Cu for the contact layer, because its thermal conductivity is about 120 times greater than that of cyanoacrylate, used in the former model. Moreover, the surface of the heater has been increased to 2 mm^2.

5.2.4.Optimized sensor development

On the basis of FEM and dimensional analysis, a new design has been implemented and the optimized prototype has been microfabricated in order to check the technological viability of the design choices.

A schematic of the geometry of the electrical parts of the sensor is shown in Figure 5.9.

The heater serpentine has a width of 130 μm and its surface is 2 mm^2. The sensor has four connections: two inner ones for sensing the voltage drop across the micro-heater and two outer ones for current supply. Different widths for the two sets of leads have been designed, in order to reduce the voltage drop occurring across the powering leads, by implementing an unique fabrication process. The inner connections width is 1.3 mm; the outer connections width is 3.62 mm; inner and outer pads dimensions are 3.5x3.5 mm^2 and 5.12x3.5 mm^2 respectively.

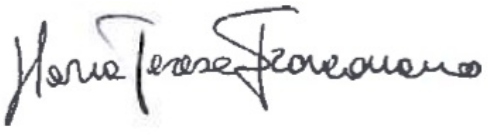

SU-8 has been chosen as a protective layer (thickness: 15 µm). A 30 um thick Cu foil has been used as contact layer, as suggested by the sensitivity analysis.

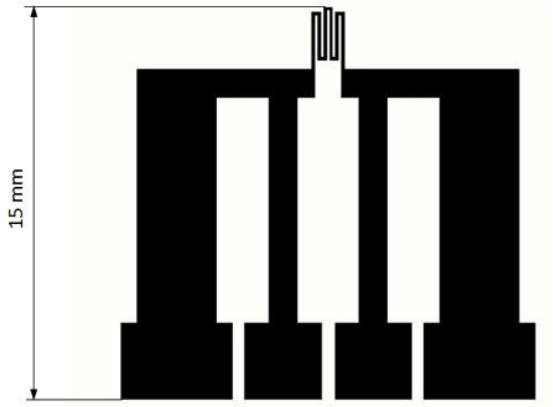

Figura 5.9: Footprint of the optimized sensor metal part.

The main fabrication steps (shown in Figure 5.10) are:

a) Cr/Au Lift-off (photolithography and sputtering);

b) Deposition and patterning of the protective layer;

c) Assembling of the Cu layer.

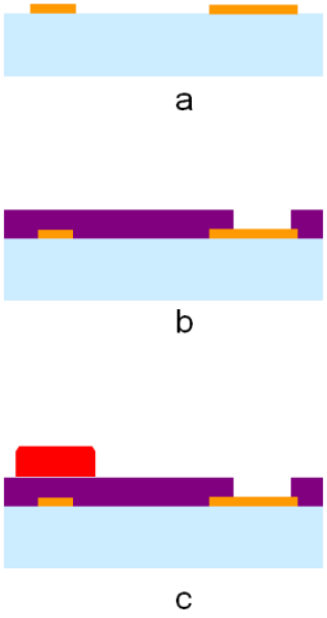

Figure 5.10: Fabrication process of the optimized sensor.

Maria Teresa Francomano

The design of the flexible thermal slip sensor (section 5.2.5) has been based on the outcomes of the optimization analysis, including some further improvements, as detailed in the following section.

5.2.5. Thermal slip sensor on flexible substrate

Compared to the previous prototype [Accoto, 2008], described in section 5.2.2, the sensor described in the following paragraphs has been microfabricated on a flexible substrate and the contact layer has been removed in order to improve the heat flux exchanged between the microheater and the object surface.

The design and microfabrication are reported in section 5.2.5.1, while the characterization set-up and the detection strategy are detailed in section 5.2.5.2-5.2.5.3. Experimental results, which extend and detail the preliminary ones reported in [Francomano, 2012b], are discussed in section 5.2.5.4.

5.2.5.1 Fabrication and thermal characterization

The multilayered structure, shown in Figure 5.11, includes a polyimide substrate, a thin metal film layer and a protective polyimide coat.

The metal film is sandwiched between the two polyimide layers, which have the same thickness, thus lying on the neutral plane of the structure. This configuration preserves the metal from possible structural failures caused by tensile stresses that may arise during bending. Indeed the *neutral plane* is the surface where the stresses caused by bending moments are zero. Metal layers deposited on the neutral plane could theoretically undergo unlimited bending.

The active area of the sensor is an Au microheater, 25 nm thick, shaped as a serpentine, 130 μm wide, with a total length of 15.5 mm and a surface area of 2 mm^2 (Figure 5.11).

The microfabrication of the sensors includes standard photolithographic and lift-off processes, the main steps being as follows:

- **Substrate**: 15 um of polyimide (Duramide 115A) has been spun on a sacrificial 4'' silicon wafer. A soft (at 100°C for 120s) and hard bake (at 350°C for 1h 30') processes have also been performed.

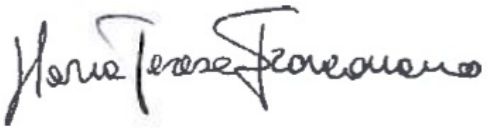

- **Metal Layer**: A lift-off process has been made by using a negative photoresist (ma-N 400 Microresist), patterned by means of a photolithographic process. In order to allow the adhesion between the Au and the polyimide layers, a multilayer metal film, Cr/Au/Cr (thickness: 2,5 nm/25 nm/2 nm) has been evaporated.
- **Protective layer**: 15 um of photodefinable polyimide has been patterned in order to cover the metal layer, while keeping open the pads for electrical connections. Finally, in order to avoid pads oxidation, the 2nm Cr layer has been etched.

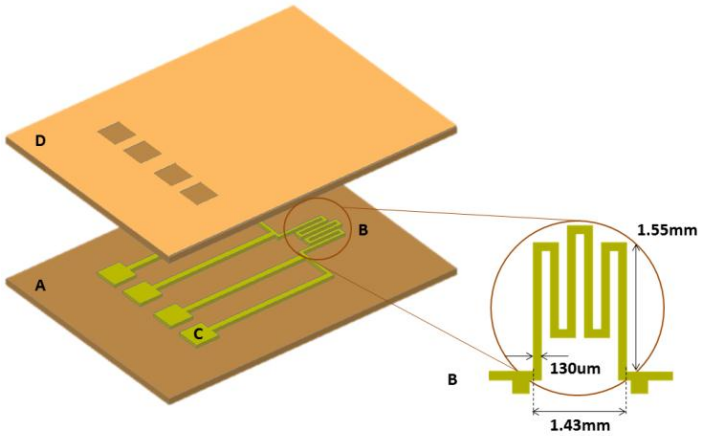

Figure 5.11: A 3D schematic of the flexible sensor; (**A**) polyimide substrate; (**B**) microheater; (**C**) pads; (**D**) polyimide covering layer.

The complete structure (polyimide/metals/polyimide) has been removed from the Si sacrificial substrate by using a Tetra-Methyl Ammonium Hydroxide (TMAH) attack.

Figure 5.12 shows a schematic of the microfabrication process. A picture of the actual sensor is in Figure 5.13.

The temperature-resistance characteristic of the sensor has been obtained using a Type-K thermocouple (Model 80BK-A, by Fluke) and an OHM meter (Model 189, by Fluke).

Maria Teresa Francomano

As shown in Figure 5.14, data can be fitted linearly (σ^2=0.9995): R=1.4602 T+585.39, where the resistance R is in [Ω] and the temperature in [°C].

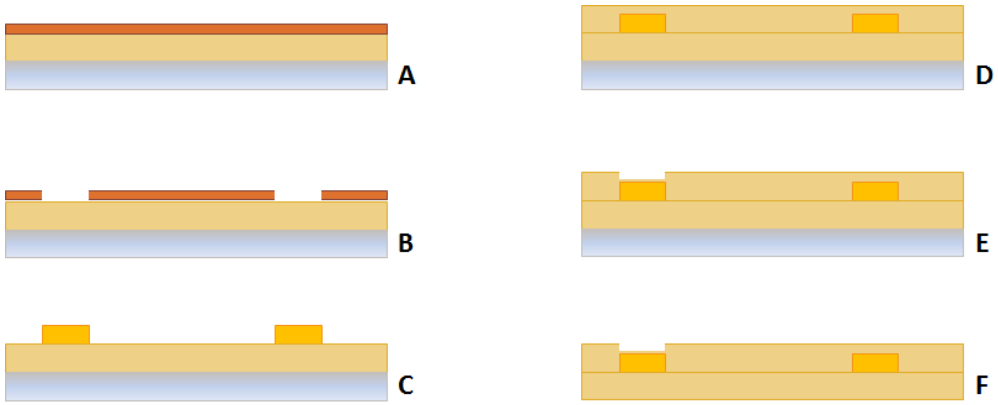

Figure 5.12: Microfabrication process. (**A**) Deposition of 15 um of polyimide on a Si wafer; spin coating of a negative resist; (**B**) patterning of the negative resist; (**C**) metals deposition; (**D**) 15 um polyimide deposition; (**E**) pads opening (photolithography); (**F**) Si sacrificial layer removed by TMAH attack.

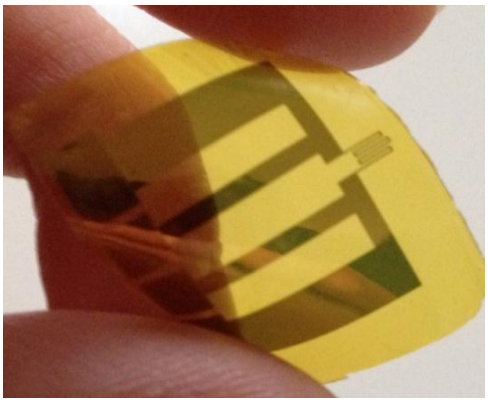

Figure 5.13: Picture of a bent slip sensor.

The maximum temperature, which the sensor can safely withstand, has been determined experimentally to be above 75°C.

Since the temperature of the microheater increases with the increase of the current supplied, it is necessary to keep the current below a safety threshold. When a constant current is provided, the temperature reached by the microheater depends on all those factors affecting the boundary conditions of the

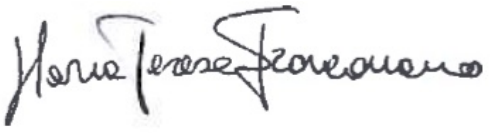

thermal problem, including the mounting/packaging of the sensor and the thermal and geometric properties of the touched objects. A simplifying and cautionary approach for evaluating the maximum current, which can be safely fed to the sensor, consists in limiting its heat exchanges with the environment, e.g. by having it suspended in air.

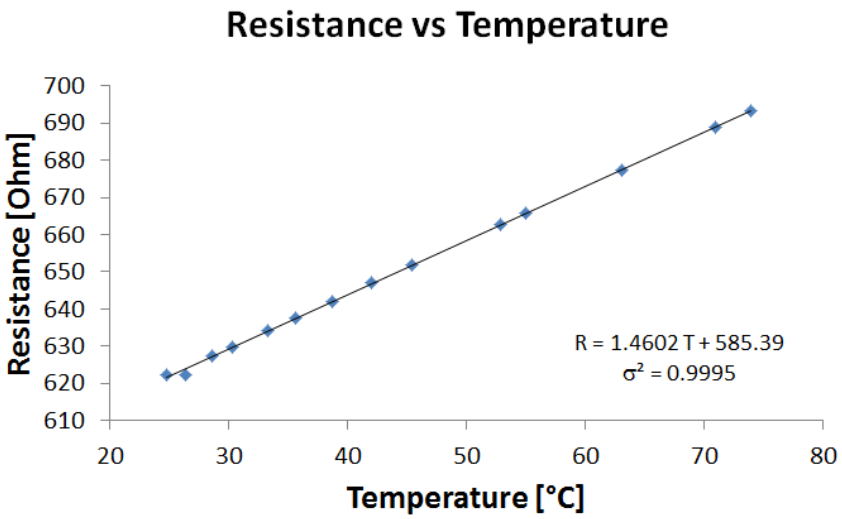

Figure 5.14: Thermal characterization of the flexible sensor.

In this configuration, different current values, ranging from 1 mA to 15 mA have been provided to the microheater. Figure 5.15 shows the data obtained, which can be fitted by a quadratic relation (σ^2=0.9949): R=328535 I^2+14.482 I+620.98, where the resistance R is in [Ω] and the current in [A].

Finally, the electromechanical performance of the sensors has been characterized under bending.

Resistance was measured with the sensor wrapped around cylinders with different radii, aligned along both principal radii of curvature.

Figure 5.16 reports example experimental data. Each measurement has been repeated three times. As expected, the sensor resistance does not vary significantly under bending.

Maria Teresa Francomano

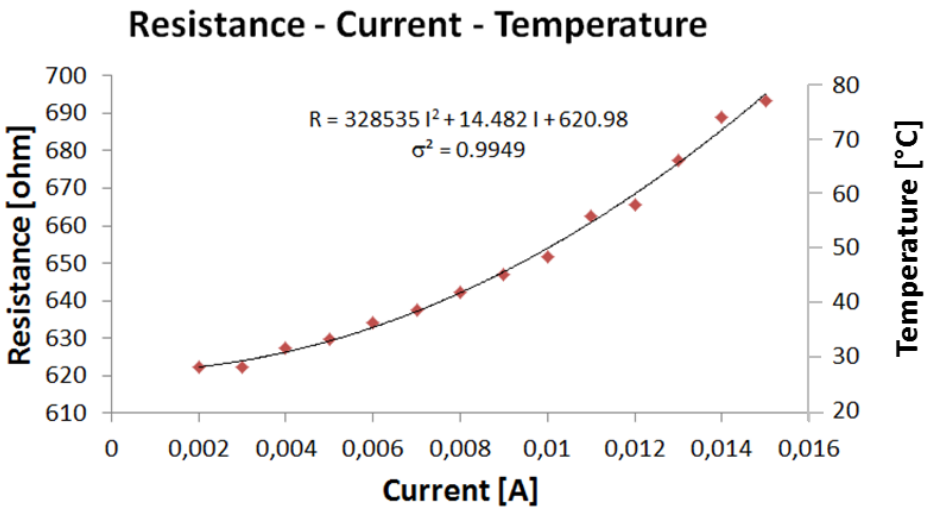

Figure 5.15: Experimental relation between the current supplied to the sensing element and its resistance variations when the sensor is suspended in air.

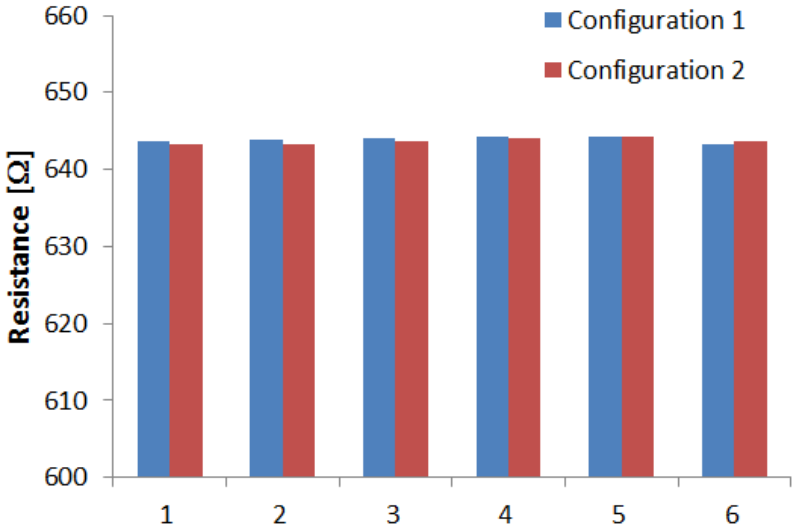

Figure 5.16: Electromechanical performance of the thermal slip sensor during bending. Configuration 1 refers to first principal curvature $1/r_i$, whereas Configuration 2 refers to second principal curvature 0. Classes 1-5 correspond, respectively, to cylinders with radii, r_i, of 3.3 cm, 1.8 cm, 1.5 cm, 0.5 cm and 0.3 cm. Class 6 refers to the measurements obtained by posing the sensor on a flat surface.

5.2.5.2. Experimental set-up

A custom set-up, capable of providing controlled slip speeds, has been developed.

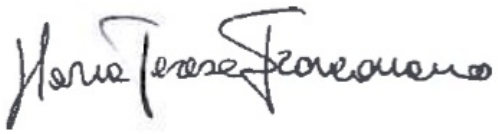

A Scotch-Yoke mechanism (Figure 5.17 A), in the following named "slip generator", has been assembled for converting the constant rotary motion of a crank into the linear harmonic oscillation of slipping bars.

The slip sensor has been coupled to a fixed frame through an elastic element (Figure 5.17 B), which compensates for possible geometric irregularities of the touched surface.

The crank is moved by a DC gearmotor (Maxon Motor EC 45 Flat 50 W; reduction ratio: 26:1) with an embedded incremental encoder (2000 pulses/turn).

Measurements of the microheater resistance and the motor position have been performed using two DAQ cards, the NI9205 and the NI9401, respectively, while current has been supplied by another DAQ card, the NI9265. All the DAQ cards (by National Instruments) have been connected to a programmable automation controller (NI CompactRIO, by National Instruments).

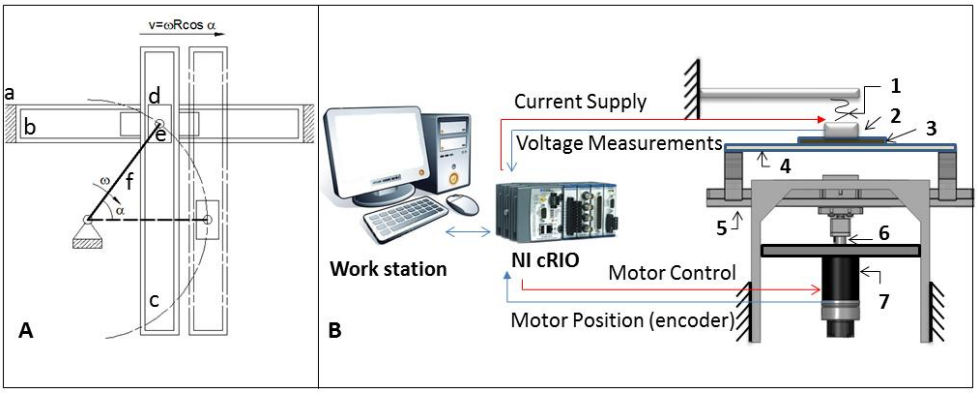

Figure 5.17: Experimental set-up. **(A)** Schematic of the Scotch-Yoke mechanism; **a**. Frame; **b**. Horizontal linear guide; **c**. Vertical linear guide; **d**. Slider; **e**. Pivot; **f**. Crank. (**B**) The whole experimental set-up, including *i)* a workstation, running Labview RT (by National Instruments); *ii)* a programmable automation controller (NI CompactRIO, by National Instruments); and *iii)* the custom made mechanical set-up. **1**. Elastic element; **2**. Thermal slip sensor; **3**. Slipping bar; **4**. Plate; **5**. Linear guide; **6** Crankshaft; **7**. DC Motor.

Both temperature control and motor rotation control have been implemented on a workstation, using LabviewRT (by National Instruments).

The whole experimental set-up is shown in Figure 5.17 B.

Maria Teresa Francomano

Bars of different materials (polyvinyl chloride-PVC, polytetrafluoroethylene-Teflon, and pinewood) with a rectangular cross-section (25 mm x 70 mm; thickness: 3 mm) and similar surface roughness (2.5÷4 μm Ra) have been fixed on the frame, with one side in contact with the sensor.

5.2.5.3. Detection strategy

In order to keep the microheater temperature at a constant value, a two-state bang-bang control has been implemented, with only two current intensities supplied to the microheater: I_L and I_H ($I_L<I_H$).

Let's consider a target temperature T_T and let R_T be the related resistance measured across the sensing element. Once T_T is reached, the voltage drop across the microheater can assume two reference values: $V_L=R_T I_L$ or $V_H=R_T I_H$.

According to (5.1), when a constant current is supplied, changes in the microheater temperature cause proportional variations to V_L and V_H. Therefore, after each sampling period, T_s, the voltage drop across the microheater is compared to the reference voltage (i.e. to V_L if the supplied current is I_L; to V_H if the supplied current is I_H).

Let's define S_0 and S_1 as the states when I_L and I_H are supplied, respectively.

Starting from the initial state S_0, if the measured voltage is lower than the reference voltage V_L (i.e. $R<R_T$), it is necessary to heat up the microheater. Therefore a transition from S_0 to the S_1 is required ($S_0 \rightarrow S_1$). Otherwise, (i.e. $R>R_T$), no transition occurs. Once in S_1, if the measured voltage is lower than the reference voltage V_H, it is necessary to keep heating the sensing element, and no state transition occurs. On the contrary, if the measured voltage overcomes V_H, it is necessary to cool down the microheater by switching to I_L ($S_1 \rightarrow S_0$).

All the possible state transitions are summarized in Table 5.3 and graphically shown in Figure 5.18. By using the symbols in Table 5.4, the truth table associated to the state diagram can be built (Table 5.5).

The corresponding control algorithm can be implemented using a logical multi-level network (Figure 5.19), simplified using Karnaugh's maps [Kratz, 1998].

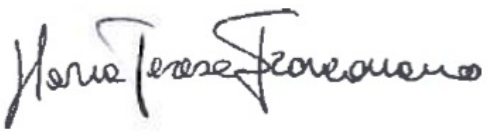

Binary values can be used to represent the two possible values of the supplied currents: "1" stands for I_H and "0" for I_L. The values of supplied currents are stored in a binary string (**I**). During an experimental session a value ("1" or "0") is appended to **I** every T_s seconds.

Input	Description	Transition
IN_1	$V<V_L$	$S_0 \rightarrow S_1$
IN_2	$V \geq V_L$	$S_0 \rightarrow S_0$
IN_3	$V<V_H$	$S_1 \rightarrow S_1$
IN_4	$V \geq V_H$	$S_1 \rightarrow S_0$

Table 5.3. Table of States.

Symbol	Condition	Logical Value
A	$V<V_L$	1
B	$V<V_H$	1
C	$I=I_H$	1

Table 5.4. Logical conditions.

The analysis of **I** is sufficient to detect slip: when slip occurs, the increase of the average current provided to the microheater corresponds to an increase in the average length of the substrings of **I** made of consecutive "1"s.

Alternative indices, able to detect a (statistically) significant increase of the number of "1"s in any substring A of **I** containing a Δ-uple of binary values, can be used.

For example, it is possible to use of the coefficient of variation [Francomano, 2012; Francomano; 2012b], defined as:

$$CV = \sigma/\mu \tag{5.12}$$

where σ and μ respectively are the standard deviation and the mean of the values in A. It is easy to show that, for a binary string, σ is not independent from μ, since: $\sigma=\sqrt{\mu-\mu^2}$.

Therefore, the coefficient of variation can be equivalently written as:

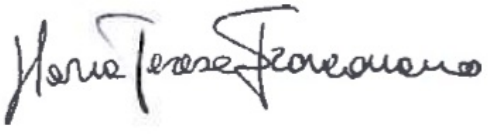

$$CV=\sqrt{(1/\mu)-1} \tag{5.13}$$

A	B	C	Output
0	0	0	0
0	0	1	0
0	1	0	0
0	1	1	1
1	0	0	N.V.*
1	0	1	N.V.*
1	1	0	1
1	1	1	1

Table 5.5. Truth table.
*N.V.: Not verifiable.

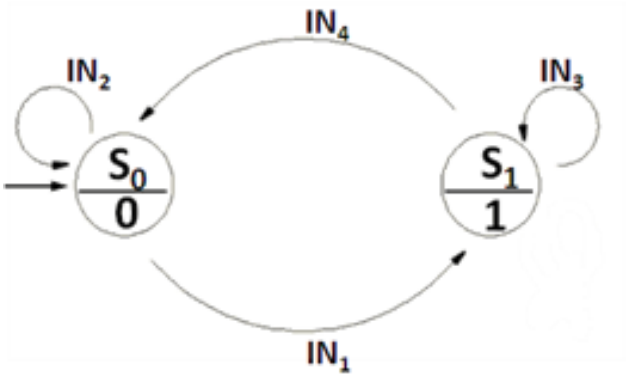

Figure 5.18: States diagram.

Maria Teresa Francomano

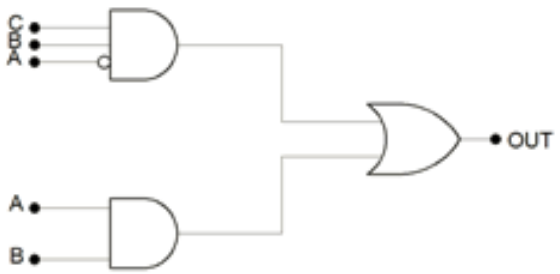

Figure 5.19: Simplified logical circuit, implementing the bang-bang temperature control.

If n_1 is the number of "1"s in A, $\mu=n_1/\Delta$, and

$$CV=\sqrt{(\Delta/n_1)-1} \tag{5.14}$$

CV approaches 0 (its minimum) when μ tends to 1 (its maximum), i.e. when $n_1 \rightarrow \Delta$. Let CV_T be a threshold value, defined experimentally during tests performed in pure conduction conditions (i.e. no slip).

The sensor would fire a slip signal when:

$$CV<CV_T \tag{5.15}$$

The value of CV_T can be set by performing tests in pure conduction conditions (no slip).

Once the electrical parameters are fixed (i.e. I_L, I_H, R_T), a binary string **I** (length: N) is stored during each test. Fixing the length Δ of the substrings (Δ was set to 10 in our experiments), a coefficient of variation is calculated for each of the N-Δ substrings [$\mathbf{I}_k$-Δ, $\mathbf{I}_k$], with $k \in (\Delta+1,N)$. CV_T is obtained as the mean of the N-Δ coefficients of variations previously calculated.

During slip tests, every T_s seconds, the current value of CV, CV_t, is calculated considering the last Δ values stored in **I**.

The one-tailed Student's t-test is implemented to evaluate if CV_T is significantly higher than CV_t, eq. (5.15). If so, a slip signal is fired.

5.2.5.4. Results and Discussion

Bars of different materials (i.e. polyvinyl chloride-PVC, polytetrafluoroethylene-Teflon, and pinewood) have been used.

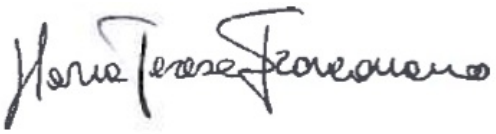

The bars have been fixed onto the slip generator, with one side in contact with the sensor (Figure 5.17 B).

Table 5.6 summarizes the values of the experimental parameters, while the thermal properties of the selected materials are reported in Table 5.7.

Power dissipation

In first instance, pure conduction tests have been performed on the three materials (Table 5.7) to set the values of CV_T, according to the methodology described in section 5.2.5.3.

During the same tests, also the average dissipated power over a time window of 60 s, in steady conditions, with I_L=1mA, I_H=13mA and R_T=616Ω, has been measured.

Figure 5.20 shows that the CV_T decreases with thermal conductivity. Indeed, by keeping the electrical parameters (i.e. I_L, I_H and R_T) constant, when the sensor is in contact with an object with a higher thermal conductivity, a higher heat exchange occurs, which requires more power for maintaining the constant temperature (Figure 5.21).

Symbol	Description	Value
I_L	Current (low)	1 mA
I_H	Current (high)	13 mA
R_0	Microsensor resistance at room temperature	595 Ω
R_T	Microsensor target resistance	616 Ω
α	Au thermal coefficient [Serway, 1998]	0.0034°C^{-1}
ω	Motor velocity	150 rpm
τ	Reduction ratio	26:1
T_S	Sampling time	1 ms
R_m	Crank radius	25 mm

Table 5.6: Parameters set during trials.

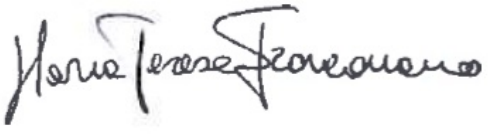

Material	Thermal conductivity at 25°C, k [W/m K]	Specific heat, cp [J/kg K]	Density, ρ [kg/m3]
PVC [Chakrabarti, 2004]	0.19	900	1400
Teflon [Steinhagen, 1977]	0.245	1172	2180
Pinewood [Steinhagen, 1977]	0.12	1674	540

Table 5.7: Thermal properties of bars materials.

The dissipated power, i.e. the power absorbed in absence of slip, is significantly lower than that reported in [Accoto, 2008], thanks to the design optimization [Accoto, 2010] and the removal of the contact layer.

Response time

When the motor rotates at constant speed (ω = 150 rpm, Table 5.6), slip velocity varies in time as described by the solid blue line in Figure 5.22.

The peak speed of the bars during their harmonic oscillations (peak slip velocities), calculated taking into account the reduction ratio of the gear head (τ) and the length of the crank (R_m), is 1.5 cm/s.

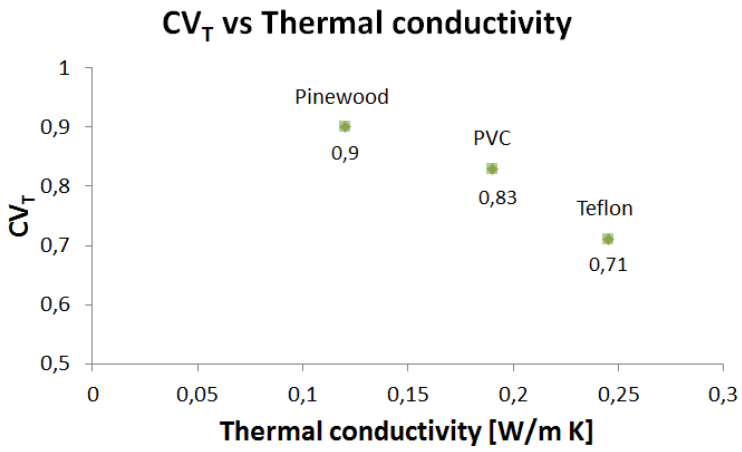

Figure 5.20: CV_T vs. Thermal conductivity for the tested materials.

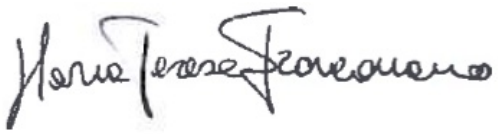

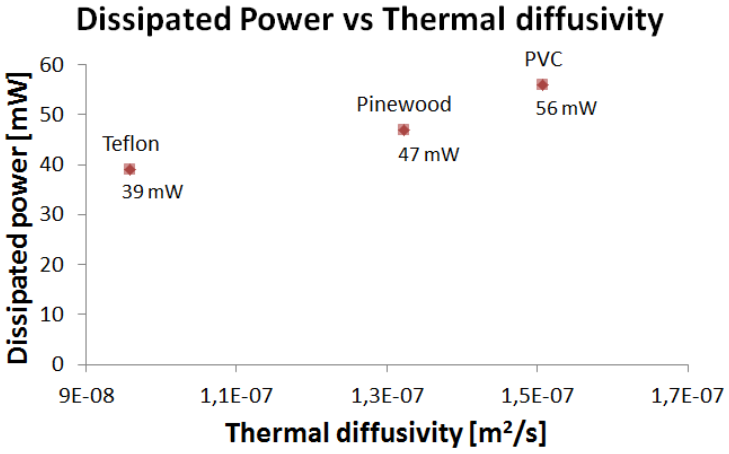

Figure 5.21: Dissipated power vs. thermal diffusivity for the tested materials.

The string **I** has been used to evaluate CV_k over the substrings $[\mathbf{I}_k\text{-}\Delta, \mathbf{I}_k]$. Figure 6.21 shows an example of data obtained using the PVC bar.

The (absolute) value of slip speed (expressed in [cm/s]) is reported as a function of the number of crank turns (solid line in Figure 5.22), while the dashed horizontal lines stand for the logical values (1,0): "1" refers to the condition $CV \geq CV_T$ (no slip), while "0" to the condition $CV < CV_T$ (slip detected).

A slip signal is fired at instant kT_s provided that $CV_k < CV_T$, according to the procedure described in section 5.2.5.3.

If the bar was at rest at instant t, the response time can be calculated as $kT_s - t$.

As it is shown in Figure 5.23, the response time decreases with thermal conductivity.

In particular, an almost 100% variation of the thermal conductivity corresponds to a variation of 17% of the response time. In the case of materials with very high thermal conductivities, such as metals (iron, for example, has a thermal conductivity three orders of magnitude higher than that of Teflon), a dramatic decrease of the response time is expected, which would require the development of an adequately fast readout electronics.

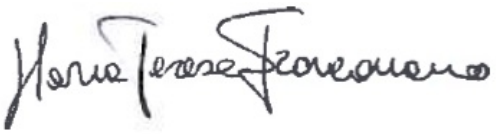

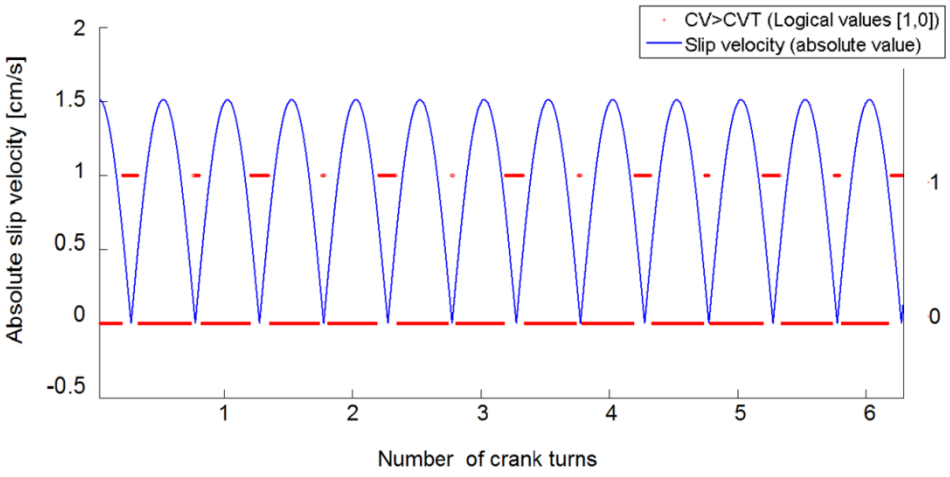

Figure 5.22: CV vs numer of crank turns, during a slip test.

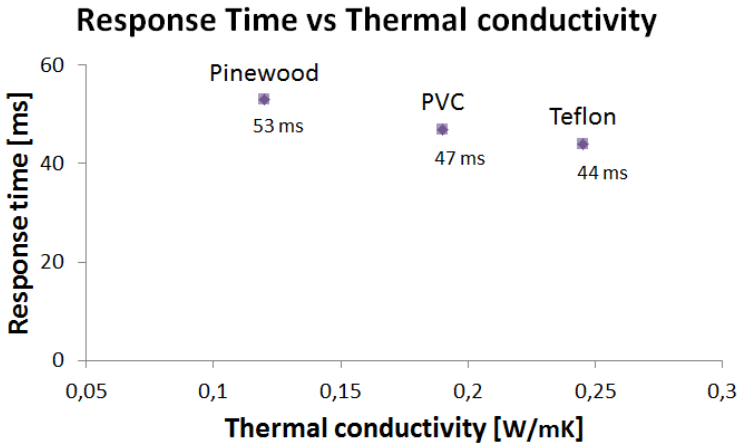

Figure 5.23: Response time of the thermal slip sensor.

For all the materials tested, the measured response times are significantly shorter than those of humans [Dahiya, 2010].

Short response times allow enough computation time to be allotted to the system controlling the grasping, still keeping the overall responsiveness of the artificial system in line with that of the human sensory-motor system.

As already mentioned in section 5.2, an array configuration has been investigated, in order to develop a sensing system capable of detecting not only

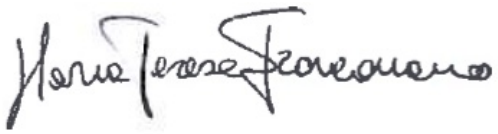

slip occurrence, but also slip direction. The following section is devoted to the description of such array of thermal slip sensing units.

5.3. Flexible arrays of thermal slip sensors

Tactile sensors are often arranged in array configurations, both for mimicking human mechanoreceptors spatial distribution and for redundancy.

During the inadvertent slippage of a manipulated object, it is often useful to detect also slip direction, in order to properly configure the robotic fingers closure.

Following the above mentioned considerations, a 2×1 cm^2 array, embedding 24 slip sensing units, has been developed, in order to improve the spatial acuity of the sensory system, as well as to allow the detection of object slip direction.

5.3.1. Design

The array includes 24 miniaturized sensing elements, in the shape of serpentines of Cr/Au, with a thickness of 2.5/9 nm. Each serpentine has a total length (if deployed) of 18.9 mm and it is 20um wide. The total area of the sensing element is 0.4 mm^2 (Figure 5.24).

The sensing units are arranged in a chessboard-like configuration for allowing the detection of slip along the main principal directions: North-South, East-West, North West/South East, North East/South West. Slip direction is inferred by considering the sequence of spatial activation of the sensing units when a slip event occurs (Figure 5.25 (A)).

Thirty-one pads connect the array to the read-out electronics. Each line of the chessboard is supplied with a constant voltage, while electrical connections guarantee the access to each sensing element for measurement purposes (Figure 5.25 (B)).

5.3.2. Array Microfabrication

The array has been developed using photolithography and lift-off, according to the following steps:

- 15 um of polyimide deposition on 4'' Si Wafer (sacrificial layer);

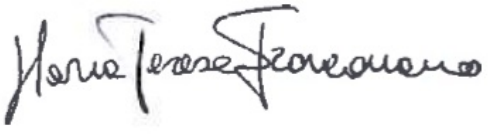

- Negative photoresist deposition (ma-N 400 microresist) on Duramide substrate and photolithography;
- Metal deposition (Cr/Au/Cr; 2,5nm/25nm/2nm);
- Lift-off;
- 15um of photo definible polyimide (HD 4110 MicroSystem) deposition and photolithography, for pads openings;
- 2nm Cr etching (using Cerium salt);
- Multilayer structure peel off from the sacrificial silicon wafer (using TMAH attack)

The average measured resistance of the sensing elements is 4.0 kΩ.

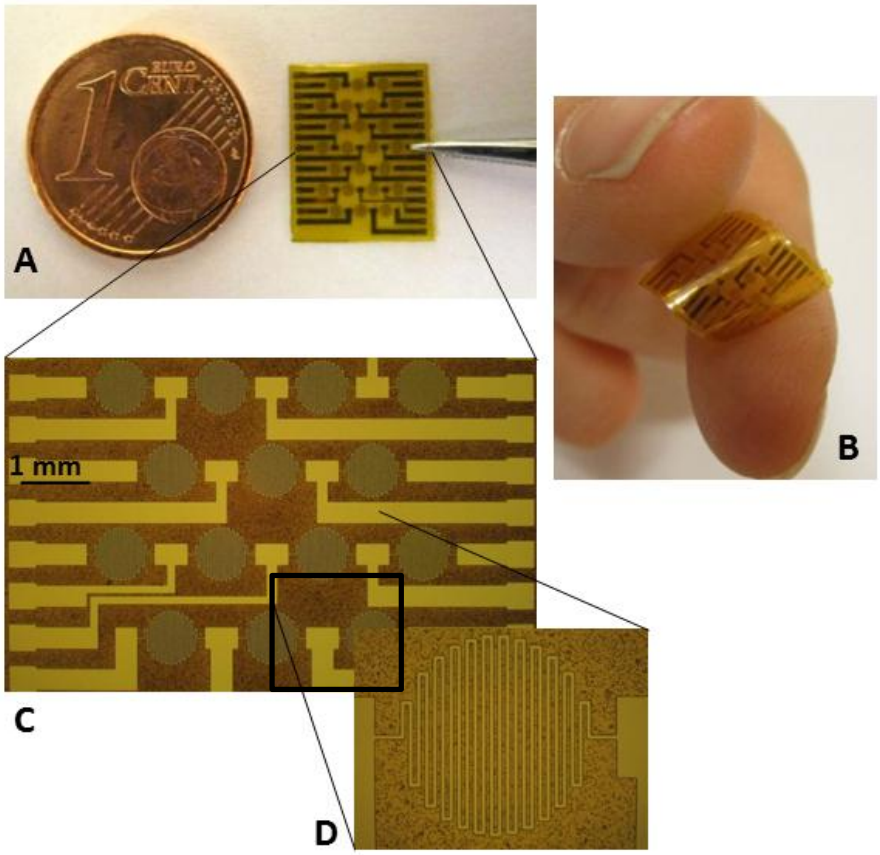

Figure 5.24: (A), (B): Slip sensors array (2×1cm^2). The sensing elements, i.e. serpentine-shaped microheaters (D), are distributed in a chessboard-like configuration (C).

Maria Teresa Francomano

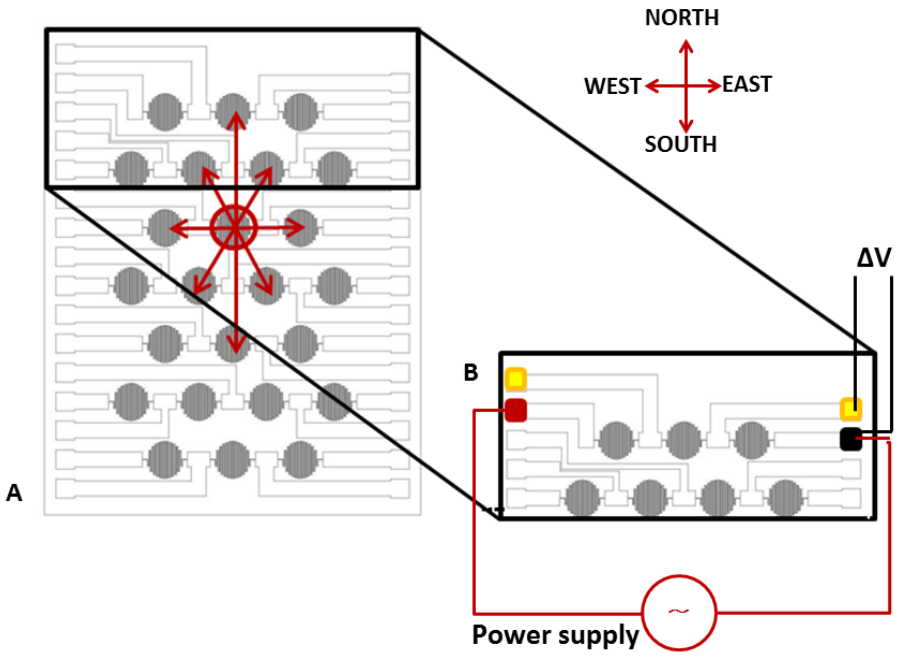

Figure 5.25: Schematic of slip directions detection (A) and array control (B).

5.3.3. Array control

Each row of the array is kept at a constant voltage.

If voltage drop variations across sensing elements overcome an experimentally defined threshold, the sensors fire a signal of slip occurrence.

By assuming point contacts and analyzing the sequence of activation of the sensing units, it is possible to retrieve the slip direction, thanks to an *ad hoc* algorithm implemented in LabView. The developed software includes the following features:

- Data acquisition;
- Data elaboration (for slip detection and slip direction detection);
- Data recording;
- User Interface (UI).

The UI has been designed in order to allow *i)* the selection of a path, for data recording; *ii)* the acquisition parameters setting; and *iii)* the display of results.

The control scheme implemented is summarized in the process flow in Figure 5.26.

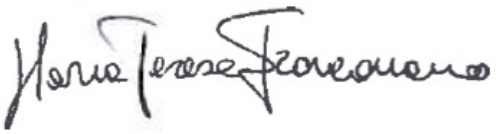

Data from all the sensing elements are acquired and recorded. By assuming the condition of point-wise contact, when slip is detected by one of the units in the array, the algorithm checks for possible slip detection by neighboring units. The starting point of slip as well as the retrieved slip direction are graphically displayed by means of virtual LEDs and arrow indicators.

The user can display also voltage variations and can manually interrupt the scanning. The cycling period is 300ms.

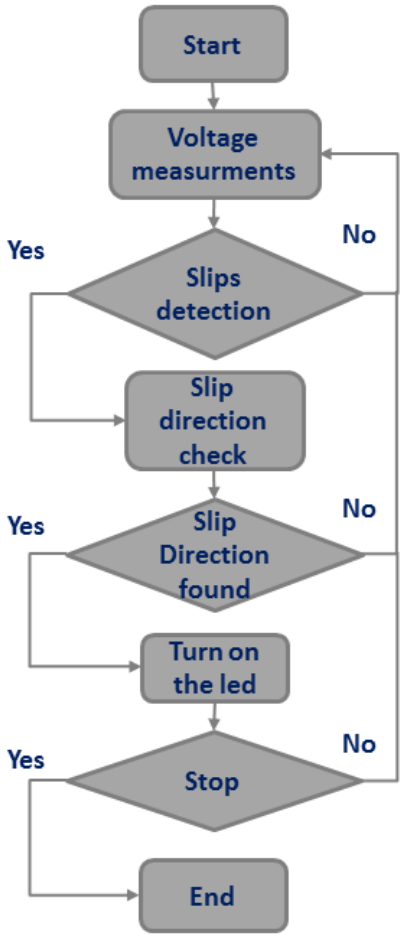

Figure 5.26: Workflow of the array control algorithm.

5.3.4. Set-up

Tests have been performed using a custom-made electronic board, replicating the array operation.

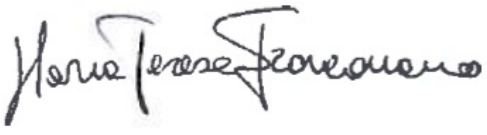

Figure 5.27 shows the set-up, which includes a power supply for keeping the array elements at a constant voltage. Each sensing element is connected to a channel of a DAQ card (NI 9205, by National Instruments), which is connected to a workstation, running Labview, by means of a chassis (cDAQ-9174, by Nation Instruments). An additional electronic circuit has been interposed between the array and the DAQ card. Its function consists in converting the measured voltage by sensors to a voltage within the limits of the DAQ analog input (AI) (+10 V and −10 V).

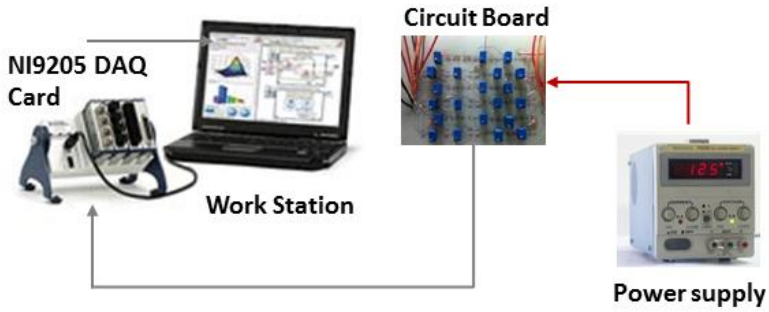

Figure 5.27: Experimental set-up for testing the array control software.

5.3.5. Results

Trimmers, having the same electrical resistance of the slip sensors, have been arranged in a chessboard-like configuration on the electronic board. The trimmers allow simulating the resistance variations occurring at the microheater, due to convective fluxes during slip events.

A slippage path has been defined (Figure 5.28) and simulated on the electronic board, by sequentially varying (manually) the resistance of the trimmers along the path. The starting point is denoted by **a** in Figure 5.28, while the slippage path is obtained by the sequence of steps from **a** to **l**.

The experimental tests validated the algorithm, showing its capability of detecting both the starting point of slip and its direction, according to the simulated trajectories (Figure 5.29).

Maria Teresa Francomano

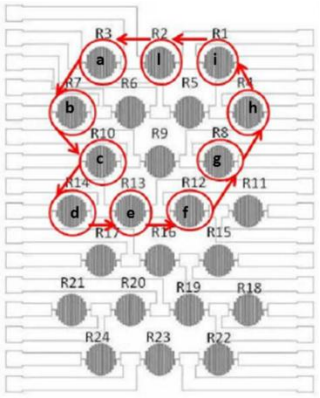

Figure5.28: Simulated slipping path (a-l).

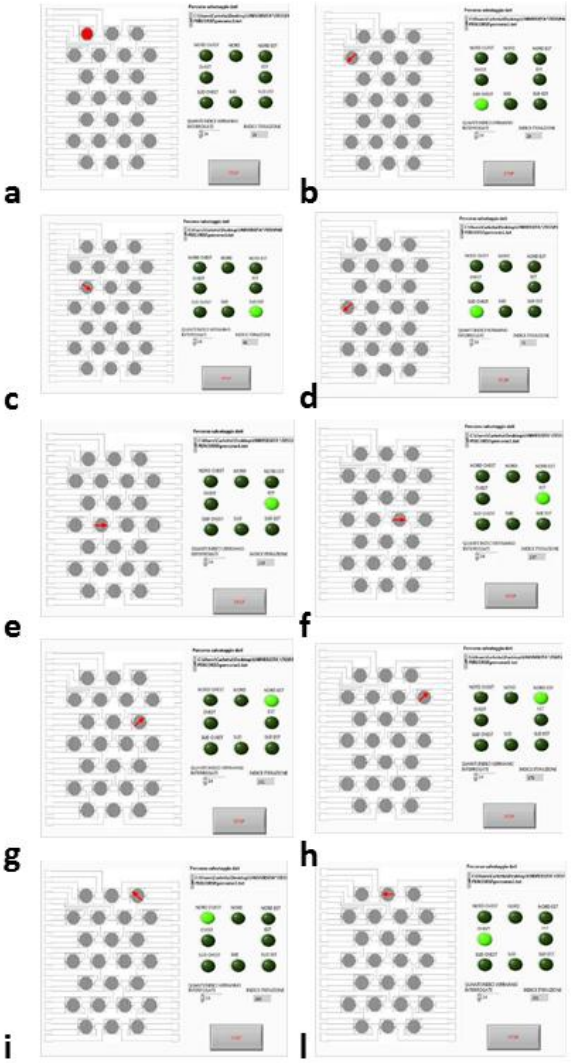

Figure 5.29: Detected slipping path, graphical UI.

Maria Teresa Francomano

5.4. Flexible multilayered silicon structures

In order to develop flexible devices (e.g. thermal slip sensors) integrating the readout electronics it is highly desirable to use silicon as substrate.

The bending capabilities of a multilayered structure, consisting of thin metallic films patterned on a silicon support and protected by a polymeric layer, have been analyzed.

The investigation has been focused on a SOI substrate, thinned by wet etching for obtaining a thickness of 2 μm. As it regards metallic thin films, Cr/Au and Cr/Pt have been taken into account. The polymeric protective layer is SU-8.

Being the thickness negligible compared to transversal dimensions, the device has been modelled as a two-dimensional structure (i.e. *laminated plate*).

The objective of this study is to determine the maximum curvature that the laminated plate can safely withstand as a function of:

- SU-8 thickness;
- Type of metals on the SOI (Cr, Au, Pt).

This study allows to determine which SU-8 thickness should be used, once the expected curvature of the structure is defined.

At first, the optimal thickness of the SU-8 layer has been analytically determined. Such thickness corresponds to the one that locates the neutral plane of the structure on the metallization plane. Such thickness is the safest for the integrity of metal layers.

In a second step, a FEM analysis has been performed for different SU-8 thicknesses to evaluate the maximum curvature that can be imposed to the structure with no failure occurring in metals, SOI or SU-8.

5.4.1. Optimal SU-8 thickness for metallization integrity

The analysis is based on the following two hypotheses:

1. the thickness and flexural stiffness of metal layers can be neglected compared to the thickness and flexural stiffness of either SU-8 or SOI plates.
2. SOI wafer thickness is constant($2\mu m$).

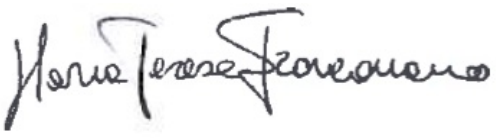

With reference to Figure 5.30, let η_n be the position of the neural plane. The objective of the investigation is to identify the SU-8 thickness so that $\eta_n = 2\mu m$. The symbols used in the following are summarized in Table 5.8.

Symbol	Meaning	Value
η_n	Neutral axis position	h_2
η_1	Neutral axis position of SU-8 plate (*if alone*)	$h_2 + \frac{h_1}{2}$
η_2	Neutral axis position of SOI plate (*if alone*)	$\frac{h_2}{2}$
h_1	SU-8 thickness	*To be determined*
h_2	Silicon thickness	$2\mu m$
E_1	SU-8 Young modulus	4.02 GPa
E_2	Silicon <100> Young modulus	129.5 GPa

Table 5.8: List of symbols.

The position of the neutral plane of the laminated structure can be estimated according to (5.16):

$$\eta_n = \frac{\eta_1 E_1 h_1 + \eta_2 E_2 h_2}{E_1 h_1 + E_2 h_2} \tag{5.16}$$

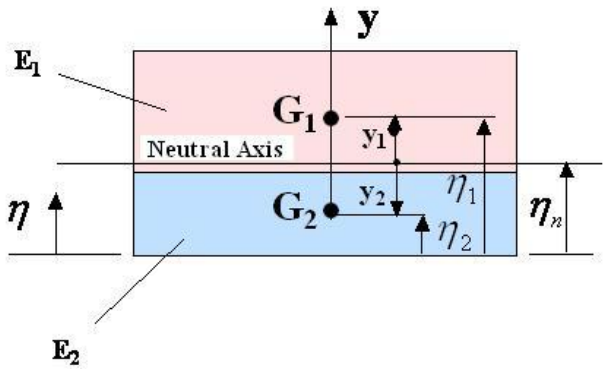

Figure 5.30: Schematic of the laminated device cross section.

By imposing $\eta_n = h_2$, we get the *desired optimal thickness for SU-8*:

Maria Teresa Francomano

$$h_1 = h_2\sqrt{\frac{E_2}{E_1}} = 11.2\ \mu m \tag{5.17}$$

The SU-8 thickness provided by (5.17) locates the neutral plane of the laminated plate on the silicon surface, where metals are deposited, so that no tensile/compressive stresses act on the metal films during bending.

5.4.2. FEM analysis

The value given by (5.17) could be critical for the microfabrication processes (i.e. during cutting). Moreover, the analytical investigation does not provide any information regarding the integrity of SOI or SU-8.

Therefore, a FEM analysis has been implemented in order to identify the maximum curvature that can be imposed to the laminated plate without the occurrence of mechanical failure in any of its components.

The implemented steps are:

1. Laminated plates with constant footprint (1000 x 1000 um^2) and different SU-8 thickness were designed using a CAD software; thickness varies from 10 um to 130 um.
2. A constant bending moment was applied at the edges of the laminated plate; the corresponding curvature C_n was retrieved from simulations.
3. The strain ξ_x at h_2 was evaluated.
4. The stress (s_x) at $h_2$was calculated according to (5.18) for different metals.
5. The maximum stresses in SOI and SU-8, due to the applied bending moment, were retrieved from FEM simulations.
6. By taking into account the proportionality between stresses and curvature, the maximum allowed curvature (C_{max}) for the plates was inferred using (5.19).

$$s_x = \frac{E}{1-\nu^2}\xi_x \tag{5.18}$$

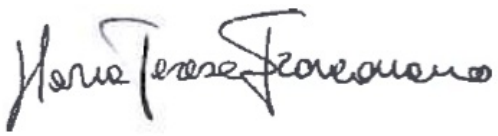

$$\frac{C_n}{s_{xn}} = \frac{C_{max}}{s_{max}} \rightarrow C_{max} = \frac{C_n s_{max}}{s_{xn}} \tag{5.19}$$

Relevant mechanical properties of materials are reported in Table 5.9.

Mechanical Property	Si	SU-8	Au	Pt	Cr
Young modulus, E [GPa]	129.5	4.02	78	168	279
Poisson modulus, ν	0.28	0.22	0.44	0.38	0.21
s_{max} [MPa]	2800	34	122	38	83

Table 5.9: Mechanical properties of Si, SU-8, Au, Pt, Cr.

5.4.3. Results

The maximum curvatures allowed by SOI, SU-8, Au, Pt and Cr, as a function of SU-8 thickness, are reported in the bi-logarithmic plot in Figure 5.31. Here curvatures are normalized with respect to $C_0 = 10^2\ m^{-1}$ (corresponding to the plate being wrapped around a cylinder with radius $10^{-2}\ m$). SU-8 thickness is in um.

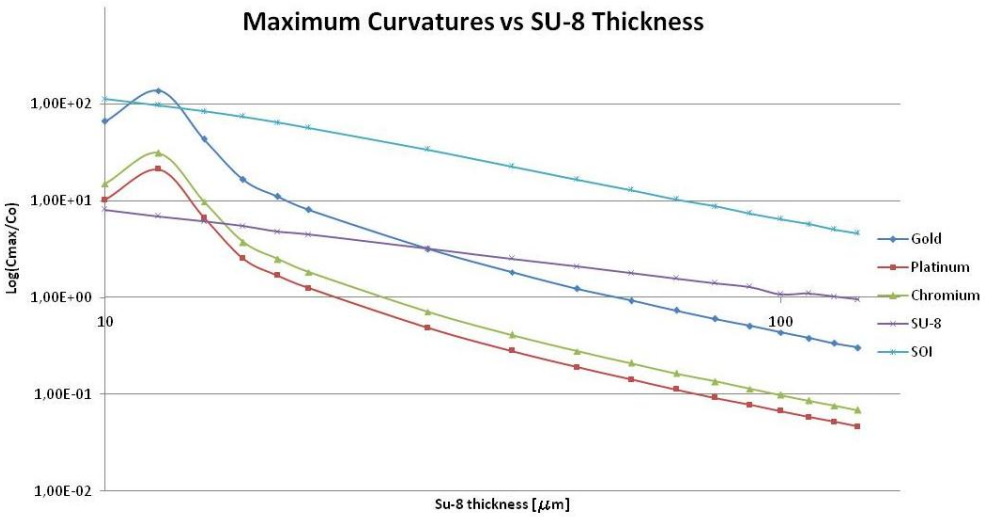

Figure 5.31: Maximum normalized curvatures (log) in function of SU-8 thickness (um, log).

For any SU-8 thickness, the maximum curvature that can be imposed to the laminated structure is the *minimum* among the maximum curvatures corresponding to the materials taken into account.

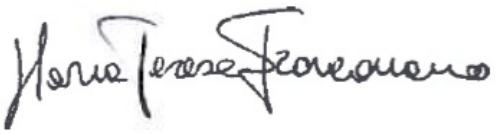

For SU-8 thickness ranging from 10 to 14 μm, the maximum curvature is upper-bounded by SU-8 strength.

Metals have different behaviors. In particular, Au withstands the highest curvatures, while Cr and Pt impose stricter constraints.

For SU-8 thickness above 14 μm, the maximum curvature is upper-bounded by Cr integrity.

Overall, *if Pt can be avoided*, the maximum curvature that can be imposed to the laminated plate, is highlighted in Figure 5.32 (solid black line).

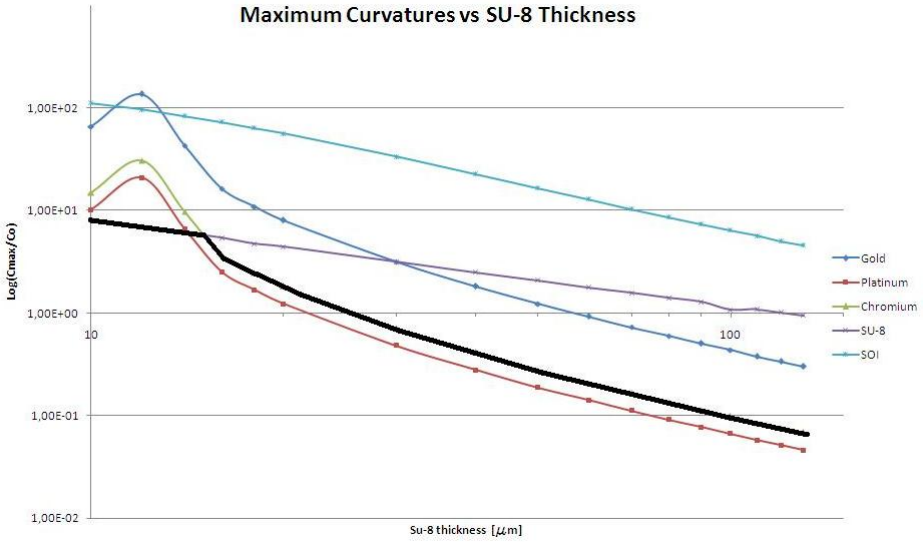

Figure 5.32: Maximum curvature as a function of SU-8 thickness.

The limit curvatures highlighted in Figure 5.32 are reported in Figure 5.33 in semi-logarithmic scale. Here a graphical representation of curvatures is also shown for SU-8 thicknesses of 10, 14, 16, 20, 30 and 50 um (a reference line is included in the figure).

The investigation allowed to evaluate the maximal curvature that can be safely imposed to the microdevice. The maximum curvature is a descending function of SU-8 thickness.

- For increasing curvatures, a mechanical failure is expected on SU-8 for SU-8 thickness between 10 and 14 um; on Cr/Au for larger SU-8 thicknesses.
- Pt should be avoided, since this material would easily undergo mechanical failure.

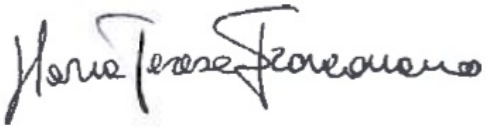

- In order to allow the microdevice to be safely wrapped around a cylinder with a 20 mm radius[9], SU-8 thickness should not exceed 25 um.
- The order of magnitude of the described results would not appreciably change if SU-8 is replaced with other polymers with similar mechanical properties. For instance, *polyimide* has a Young module which is only 23% smaller than that of SU-8. Therefore, being stresses directly proportional to E (eq. 5.18), the results presented here can be considered as slightly cautionary in the case this polymer is used to replace SU-8.

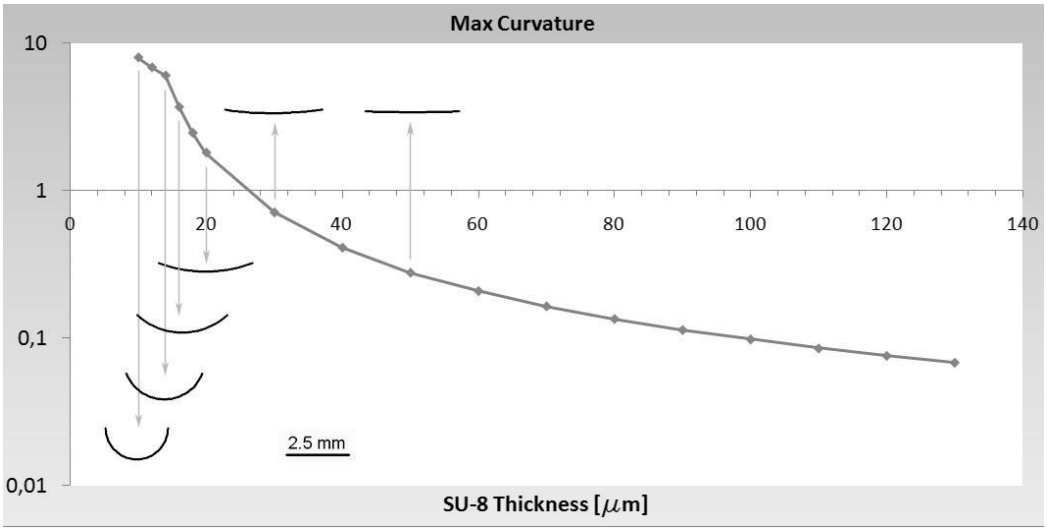

Figure 5.33: Maximum curvatures allowed as a function of SU-8 thickness.

Yielding has been considered as the critical failure mechanism for metals. This hypothesis may lead to an underestimation of maximum curvatures, since yielded metals could still be functional in several applications (e.g. in the case it is not required that the structure is bent repeatedly, nor it has to recover the unbent configuration after bending).

5.5. Discussion

Thermal slip sensors are simple to be microfabricated and robust with respect to the variety of possible surface features of the handled objects. Moreover, it is

[9] This special requirement is for the integration of the slip sensor on the robotic fingertip.

Maria Teresa Francomano

worth mentioning that the thermo-electrical principle, exploited by such sensors, does not require vibrations detection, and it can be implemented without resorting to moving parts. These properties represent an important advantage in robotic hands because mechanical noise, e.g. produced by motors, does not interfere with the sensor.

The first prototype of the thermal slip sensor, reported in literature, has been optimized for enhancing its performance in terms of response time. The main outcomes of the performed analysis regard the necessity of increasing the effective contact area of the microheater, thus increasing the heat flux exchange, as well as of replacing the contact material with one having better heat conduction properties.

According to the sensitivity analysis, an optimized prototype has been microfabricated, thus showing the technological feasibility of the optimized design.

With the final aim of integrating the sensor on robotic fingers (i.e. on the surface of cylinder-like structures), the thermal slip sensor has been developed on a flexible substrate. The sensing element, an Au microheater, has been sandwiched between two 15 um thick polyimide layers. This configuration implies that the metal, lying on the neutral plane of the structure, is not affected by compressive/tensile stresses during sensor bending.

The sensor has been functionally characterized. To this aim a dedicated control has been implemented for keeping the sensor at a constant temperature, and an experimental mechanical set-up has been developed in order to perform slip tests on three different and frequently used materials.

Experiments show the sensor capability in detecting slip events in about 40-55 ms, depending on the contacted material.

This result satisfies the requirement of having response times comparable but lower than those of the human skin receptors.

Moreover, in order to develop distributed sensory systems, mimicking the human skin receptors spatial acuity, an array configuration has been developed. A slip detection algorithm provides also information on slip direction. Nevertheless the

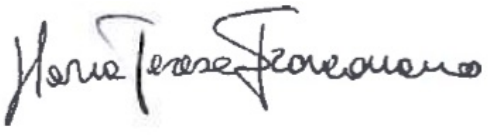

control system shows some limitations that can be overcome with additional work. In particular, the slip direction is actually detected in 300ms, a time too long for the intended application. Moreover, the current version of the software in based on the hypothesis of point contacts. Conversely, an improved version of the algorithm should allow recording simultaneously from all the sensing elements and elaborating in parallel the information, in order to detect the starting point of multiple slip events and their directions.

The possibility of developing the read-out electronics and the slip sensors on the same substrate has been also considered. This issue has been addressed by implementing an optimization analysis focused on obtaining the maximum curvature allowed for a multilayered structure, including a thinned silicon substrate, a metallization layer (for sensors sensing and connection parts) and finally a protective polymeric layer. The thickness of the latter has been retrieved from simulations in order to obtain the foldability of the multilayered structure on a cylinder with a diameter of 2 cm (i.e. the typical size of a robotic finger) without causing any failure in the whole device. Simulations provide design and material choices guidelines.

Improvements of the current thermal slip sensors can derive from the development of an adaptive control able to autonomously set the threshold value of slip occurrence as well as from the characterization of the sensor capability in discriminating initial contacts from slip events. Moreover, the readout electronics and the control will be further optimized and improved in order to be able to test the sensor with bars of several materials, covering a wider range of thermal conductivity values.

Finally, in order to test the effectiveness of the sensor in a real scenario, future work includes the sensor integration on a robotic fingertip and the development of a manipulation control scheme, integrating the sensor signals.

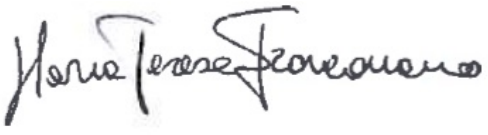

Bibliography

[Accoto, 2008] Accoto, D., Sahai, R., Damiani, F., Campolo, D., Dario, P., Guglielmelli, E. A slip sensor for biorobotic applications using a hot wire anemometry approach. Sens. Actuators A. 2008, DOI:10.1016/j.sna.2008.07.030.

[Accoto, 2010] Accoto, D., Francomano, M. T., Benvenuto, A., Luccarelli, C., Guglielmelli, E. Optimization of a thermal slip sensor using FEM and dimensional analysis. Proc. IEEE RAS/EMBS 3rd Int. Conf. Biomed. Robot. Biomechatronics, Tokyo, Japan, 26-29 Sept. 2010, 855-860.

[Adachi, 1983] S. Adachi, K. Oe, J. Electrochem. Soc. 1983, 130, 2427.

[Chakrabarti, 2004] Chakrabarti, R., Das, M., Chakraborty, D. Physical, mechanical, and thermal properties of PVC/PMMA blends in relation to their morphologies. J. Applied Polymer Sci. 2004, 93, 2721–2730.

[Chen, 2001] R.-H. Chen, C.-L. Lan, J. Microelectromech. Syst. 2001, 10, 62.

[Childress, 1985] Childress, D.S. Historical aspects of powered limb prosthesis. Clin. Prosth. Orthot. 1985, 9, 2-13.

[Cui, 2005] T. Cui, J. Wang, IEEE/ASME J. Microelectromech. Syst. 2005, 14, 895.

[Dahiya, 2010] Dahiya, R.S., Metta, G., Valle, M., Sandini, G. Tactile Sensing—from Humans to Humanoids. IEEE Trans. Robot. 2010, 26(1), 1-20.

[Engel, 2003] J. Engel, J. Chen, and C. Liu, “Development of polyimide flexible tactile sensor skin”, J. Micromech. Microeng., vol. 13, pp. 359-366, May 2003.

[Engel, 2005] J. Engel, J. Chen, Z. Fan, and C. Liu, “Polymer micromachined multimodal tactile sensors”, Sens. Actuators A, vol. 117(1), pp. 50-61, Jan. 2005.

[Fjelstad, 2011] J. Fjelstad, "Flexible Circuit Technology", 4th Edition, BR Publishing, Inc., Seaside, OR, USA, 2011.

[Fonseca, 2002] M. A. Fonseca, J. M. English, M. von Arx, M. G. Allen, J. Microelectromech. Syst. 2002, 11, 337.

[Francomano, 2012] M. T. Francomano, D. Accoto, and E. Guglielmelli, “Experimental characterization of a flexible thermal slip sensor”, Sensors, 12(11), 15267-15280, 2012.

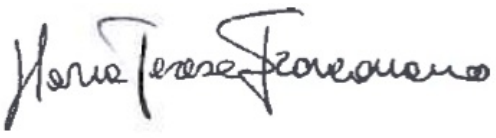

[Francomano, 2012b] Francomano, M. T., Accoto, D., Morganti, E., Lorenzelli, L., Guglielmelli, E. A microfabricated flexible slip sensor. Proc. IEEE RAS/EMBS 4th Int. Conf. Biomed. Robot. Biomechatronics, Rome, Itlay, 24-27 June 2012, 1919-1924.

[Kim, 2001] B. H. Kim, T. D. Chung, C. H. Oh, K. Chun, J. Microelectromech. Syst. 2001, 10, 33.

[Kratz, 1998] Katz, Randy. Contemporary Logic Design. The Benjamin/Cummings. 1998, 70–85. doi:10.1016/0026-2692(95)90052-7.

[Lipomi, 2011] D. J. Lipomi, M. Vosgueritchian, B.C-K. Tee, S. L. Hellstrom, J. A. Lee, C. H. Fox, and Z. Bao, "Skin-like pressure and strain sensors based on transparent elastic films of carbon nanotubes", Nature Nanotechnology, vol. 6, pp. 788- 792, December 2011.

[Liu, 2010] C. Liu, "Recent Developments in Polymer MEMS", Adv. Mater. 2007, 19, 3783–3790.

[Madou, 2002] M. J. Madou, Fundamentals of Microfabrication: The Science of Miniaturization, 2nd ed., CRC Press, Boca Raton, FL 2002.

[Mannsfeld, 2010] S. C. B. Mannsfeld et al., "Highly sensitive flexible pressure sensors with microstructured rubber dielectric layers", Nature Materials, 9,pp.859–864, 2010.

[Pang, 2012] C. Pang, G.-Y. Lee, T. Kim, S. M. Kim, H. N. Kim, S.-H. Ahn, and K.-Y. Suh, "A flexible and highly sensitive strain-gauge sensor using reversible interlocking of nanofibres", DOI: 10.1038/NMAT3380, 2012.

[Senturia, 2001] S. D. Senturia, Microsystem Design, Kluwer, Dordrecht, The Netherlands, 2001.

[Serway, 1998] R.A. Serway, Principles of Physics, 2nd ed., Saunders College Publishers, Fort Worth, Tx, 1998, p. 602.

[Shen, 2002] X.-J. Shen, L.-W. Pan, L. Lin, Sens. Actuators A 2002, 97–98, 428.

[Shibata, 2000] T. Shibata, Y. Kitamoto, K. Unno, E. Makino, J. Microelectromech. Syst. 2000, 9, 47.

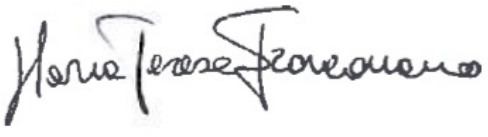

[Steinhagen, 1977] Steinhagen, H. P. Thermal conductive properties of wood, green or dry, from –40 to +100°C: a literature review. USDA Forest Service, Forest Products Laboratory, General Technical Report FPS-9. 1977.

[Wur, 1995] D. R. Wur, J. L. Davidson, W. P. Kang, D. L. Kinser, J. Microelectromech. Syst. 1995, 4, 34.

[Yoon, 2006] Y.-K. Yoon, J.-H. Park, M. G. Allen, IEEE/ASME J. Microelectromech. Syst. 2006, 15, 1121.

[Zhang, 1993] Z. L. Zhang, N. C. MacDonald, J. Microelectromech. Syst. 1993, 2, 66.

[Zhu, 2004] X. Zhu, D. M. Aslam, Y. Tang, B. H. Stark, K. Najafi, J. Microelectromech. Syst. 2004, 13, 396.

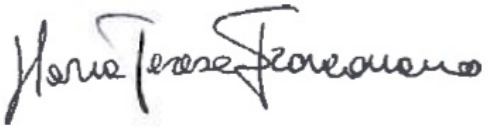

Chapter 6

Engineered surface for adhesion control[10]

The detection of object slip occurrence can inform the low level control system for triggering forces adaptation, as needed for stabilizing the grasp.

In the case of very slippery surfaces, such as lubricated or wet objects, grasp stabilization is a demanding task even for normal abled people.

Therefore, it would be useful to endow the robotic hand with the capability of managing adhesion forces as soon as a slip occurrence signal has been provided by a slip sensor.

But controlling the adhesion forces on wet surfaces is still an unmet technological goal.

State of the art techniques are mainly based on the use of adhesives [Nguyen, 2007], micropatterned surfaces [Taylor, 2010] or a combination of both [Lee, 2007].

[10] This work has been partly patented by the author (*Accoto D., Francomano M. T., Esposito C., (2012). Dispositivo e metodo per adesione controllata su substrato umido (Device and method for controlling adhesion on wet substrates). RM2012A000026*; publication n.1 of *List of Publications*).

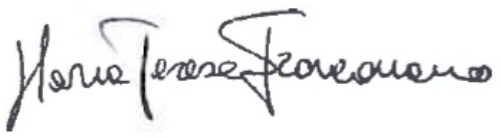

As it regards adhesives, synthetic reactive glues, such as cyanoacrylate [Bernard, 2001] or bioderived glues like fibrin [ASG, 2003], are usually employed. Recent studies demonstrate the potential of glues inspired by marine bioadhesives such as mussel proteins [Wiegemann, 2005; Guvendiren, 2008; Kamino, 2008]].

As it regards the use of micropatterned surfaces, Buselli et al. [Buselli, 2010] integrated pillars of different diameters and spacing, on the feet of a legged robotic capsule, for improving its friction properties during locomotion.

The techniques based on a combination of micropatterned surfaces and adhesives are often bioinspired. Adhesive pads are present on the feet surface of different insects, like Tettigonia viridissima (commonly known as grasshoppers) and Rhodnius prolixus, as well as of some vertebrates, like the tree frog [Gillett, 1932; Gorb, 2000; Barnes, 2007]. In particular, amphibians have a hierarchic structure on the toe pads, with microgrooves retaining a non-Newtonian two phasic secretion [Dirks, 2010].

In [Dodou, 2007] a pillar-patterned surface is coated with a mucoadhesive medium in order to improve the efficiency of a microdevice implementing the inchworm locomotion. A novel microstructured adhesive, equally effective in both dry and wet environments as well as in adhesion to both hydrophobic and hydrophilic surfaces, has been proposed in [Majumder, 2010]. The adhesive consists of a smooth, nearly elastic layer in which several subsurface microchannels are buried with or without a capillary liquid [Majumder, 2007; Verma, 2006].

The devices described in the above mentioned studies are not able to modulate the forces at the interface or consist of complex mechanisms/devices, not embeddable on robotic fingertips.

Simpler approaches, such as voltage-controlled adhesive devices [Perline, 2010a; Perline, 2010b] have been developed, but they are not specifically intended for wet environments, and limited experimental data are available about their actual performance.

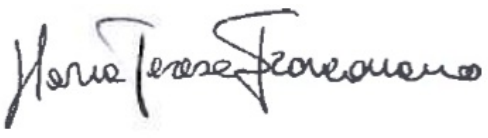

6.1. A novel technique for modulating adhesion forces

In order to actively control the adhesion on wet substrates, a novel technique, voltage-based and merging principles from electrowetting [Mugele and Baret, 2005] and wet adhesion [Qian, 2006] (namely "electrowet adhesion" [Accoto, 2012]), has been developed.

An *ad hoc* device has been microfabricated (Section 6.1.3.) for demonstrating the effectiveness of the proposed concept (Section 6.1.4.).

6.1.1. Theoretical background

Wet Adhesion

Wet adhesion is a phenomenon based on capillary suction. It enables insects (e.g. grasshoppers and flies) and amphibians (e.g. frogs) to adhere on wet and slippery surfaces.

With reference to Figure 6.1 let us consider a flat substrate (1) and a surface (2) with open channels separated by a liquid medium. Let W and h respectively be the width of the channels and the height of the gap between the substrate and the surface, with h<W.

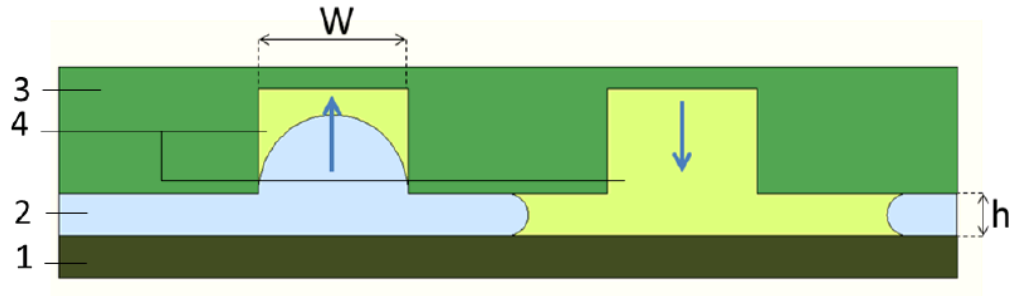

Figure 6.1: Schematic representing wet adhesion mechanism occurring in the frog toe pads when in contact with a wet substrate: 1. Flat substrate; 2. Water; 3. Frog pad surface with open channels; 4. Mucus. Arrows show the direction of capillary forces.

In the case of perfect wetting, the fluid pressure in the gap is given by:

$p_0=-\gamma/r$, where r is the radius of curvature of the meniscus (r=h/2) and γ is surface tension.

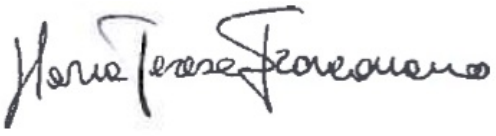

The liquid pressure in the channels is approximated as: $p_1=-\gamma/r^*$, where $r^*=W/2$. The (negative) pressure difference, $\Delta p=p_1-p_0=2\gamma(\frac{1}{h}-\frac{1}{W})$, corresponds to the suction pressure, responsible for the wet adhesion. It depends on both menisci geometry (h, W) and interface surface tension (γ).

If b is the length of the channel, the capillary force is $F_n=\Delta PbW= 2\gamma bW(\frac{1}{h}-\frac{1}{W})$.

Electrowetting

Electrowetting, first described by Gabriel Lippmann in 1875, consists in regulating the surface tension through the application of a voltage.

Several configurations are possible. The most common, named electrowetting on dielectric (EWOD), involves a planar electrode, an insulating layer, a liquid drop and a second electrode in contact with the liquid (Figure 6.2).

The contact angle (at the equilibrium) between the drop and the solid surfaces depends on surface conditions.

On smooth, planar and homogeneous surfaces, the contact angle is denoted as Young's angle, which corresponds to the equilibrium among tension forces at the three interfaces: solid (s)-liquid (l), liquid (l)-vapour (v), solid (s)-vapour (v):

$$\cos\theta=\frac{\gamma_{sv}\gamma_{sl}}{\gamma_{lv}} \tag{6.1}$$

The main equation describing electrowetting is:

$$(\frac{\partial\gamma}{\partial V})_{P,T,\mu}= -\sigma \tag{6.2}$$

where V is applied voltage, σ is the charge density at the liquid surface, P is pressure, T temperature and μ the chemical potential.

If the liquid is dielectric, σ can be considered as the surface charge density of a capacitor, and it is possible to evaluate σ as $\varepsilon_0\varepsilon_l V/d$. Hence, the variation of the surface tension coefficient is:

$$\Delta\gamma=-\frac{\varepsilon_0\varepsilon_l}{2d}V^2 \tag{6.3}$$

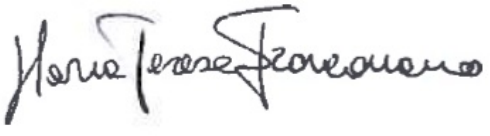

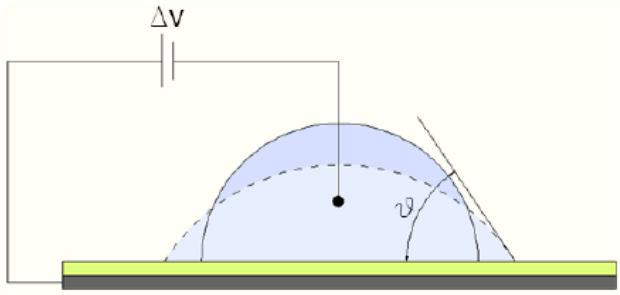

Figure 6.2: EWOD configuration. θ is the contact angle and ΔV is the applied voltage.

6.1.2. The electrowet adhesion

In Figure 6.3 the cross section of a channel, filled by two different immiscible liquids (1 and 2), is shown.

The radii of curvature, R_1 and R_2 of the meniscus between the two liquids are:

$$R_1 = R = \frac{W}{2\cos\theta} \tag{6.4a}$$

$$R_2 = +\infty \tag{6.4b}$$

The pressure difference can be evaluated as:

$$\Delta P = \gamma\left(\frac{1}{R_1} + \frac{1}{R_2}\right) = 2\frac{\gamma}{W}\cos\theta \tag{6.5}$$

According to (6.5), the capillary force is:

$$F_n = 2\gamma b\cos\theta \tag{6.6}$$

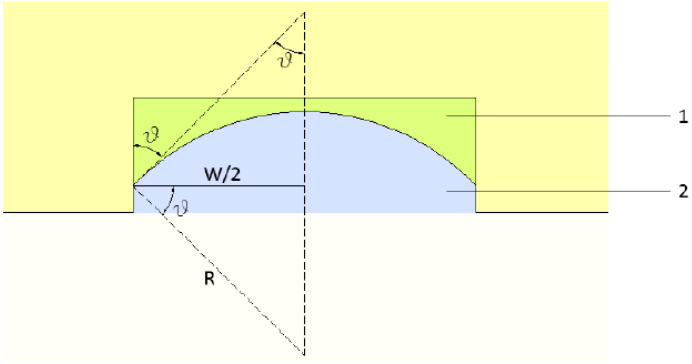

Figure 6.3: Wetting phenomenon in a solid-walled channel. Liquids (1) and (2) are immiscible.

Maria Teresa Francomano

Equation (6.6) reveals that F_n is proportional to channels length (b), surface tension coefficient (γ) and contact angle (θ).

Therefore adequate variations of these parameters allow to control the normal force F_n.

While b is merely a geometrical parameter, γ and θ depend on surface properties, which can be modified exploiting electrowetting principles (Figure 6.4).

The variation of normal force (6.6) due to an electric field can be expressed as:

$$\frac{dF_n}{dV} = 2b\frac{d\gamma}{dV}\cos\theta + 2b\gamma\frac{d\cos\theta}{dV} \qquad (6.7)$$

6.1.3. Active surface development

In order to demonstrate the feasibility of the electrowet adhesion technique, a microfabricated testing surface has been developed.

The device consists of a glass support with patterned interdigitated electrodes on top.

The electrodes are supplied with 60 V, in order to polarize an overlying patterned polymeric surface. The polarization causes a distribution of positive charges on the vertical walls (Figure 6.5).

The electrodes have been fabricated using a standard Pt lift-off process. Electrodes are interdigitated, each tooth is 150 um wide and spaced apart 25 um from the adjacent one, 1.5 cm long and 17.5 nm thick. The polymeric patterned layer that covers the electrodes (Figure 6.6) has been obtained using polydimetilsiloxane (PDMS; 10:1 volume ratio) soft-lithography.

The master mold has been obtained using the negative photoresist SU-8. The geometry transferred through the mold to the PDMS has 150 um wide channels, spaced apart 200 um and 15 mm long.

6.1.4. The experimental set-up

Adhesion tests have been performed in order to evaluate the performance of the developed active surface (section 6.1.3), once in contact with a wet substrate.

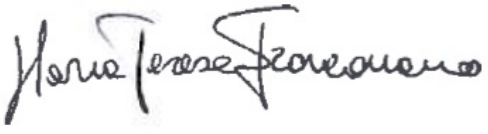

The PDMS surface has been coated using 0.1 ml of silicone oil (Sigma- Aldrich Poly(dimethylsiloxane) 200 fluid, kinematic viscosity 1000 cSt). The oil creates a concave meniscus in the polymeric channels (pure water, Figure 6.4 (A)).

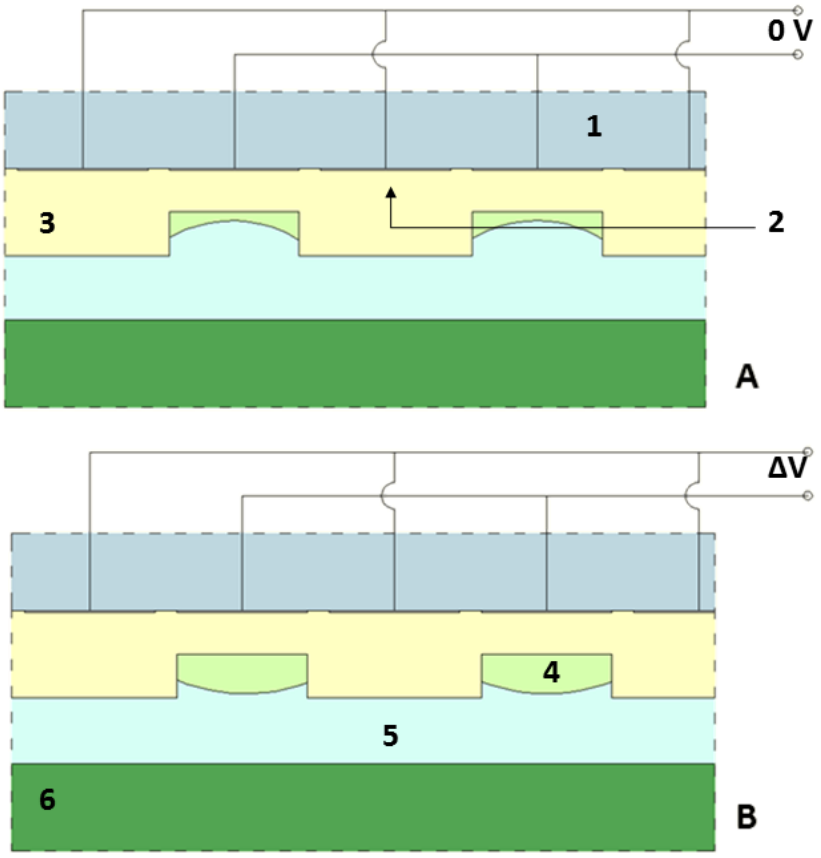

Figure 6.4: Example variation of the contact angle due to the application of an electric field (B). 1. Substrate, 2. Electrodes; 3. Polymeric patterned layer; 4. Mucus-like liquid; 5: Water; 6. Flat surface.

The wet substrate, for contacting the active surface, consists in a circular (Φ =28 mm) PET disc (rms=(1.9 ±0.3) um), sprayed with pure water before each session of experiments and dried afterwards.

Maria Teresa Francomano

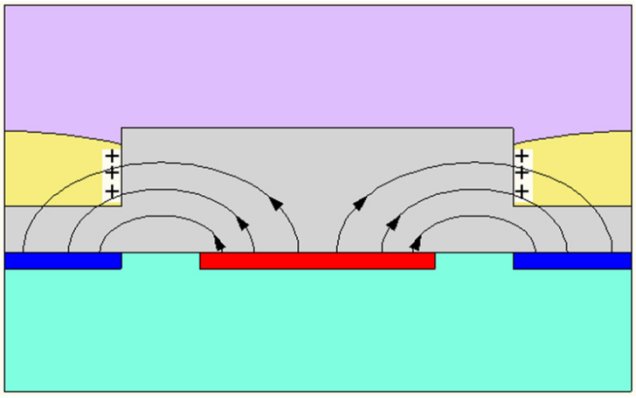

Figure 6.5: Charge distribution on the PDMS vertical walls when an electric field is applied.

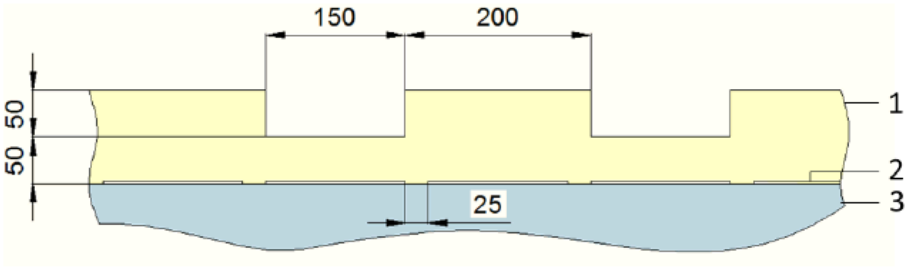

Figure 6.6: Cross section of testing device. Lengths are in μm. 1. PDMS patterned surface; 2. Pt electrode; 3. glass substrate. The thickness of the electrodes is not to scale.

A laboratory scale (EXACTA PSeries, resolution: 0.1 mg, linearity: 0.3 mg) has been adapted for detecting adhesion force changes.

Data obtained with the scale have been collected and analyzed with a dedicated software, developed in MatLab.

During the experiments the active substrate has been connected to a vertical precision positioning system (Newport EN lab-Jack M-EN40), by means of a rigid support (made of an acrylic resin).

A schematic of the experimental set-up is reported Figure 6.7.

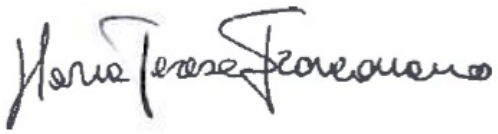

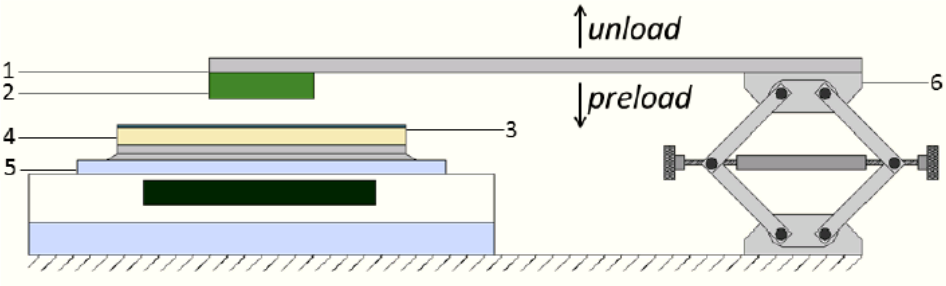

Figure 6.7: Experimental set-up. 1 represents the connection between the wet substrate (2) and the vertical precision positioning plane (6); during experiments the wet substrate is pressed on the active surface (3) lying on an acrilic resin support (4) positioned on the precision laboratory scale (5).

Voltage has been applied through a DC bench power supply connected to the electrodes through patterned pads.

6.1.5. Experimental protocol

Experiments have been performed in standard environmental conditions.

Experimental sessions have been performed implementing the following four conditions: *i*. patterned PDMS surface, no voltage supply; *ii.* patterned PDMS surface, voltage supply (60V); *iii.* flat PDMS surface, no voltage supply; and *iv.* flat PDMS surface and applied voltage (60V).

In Figure 6.8 example data (with patterned PDMS layer) are reported. It is possible to distinguish three phases.

- The first phase shows a decrement, with respect to the baseline, of the recorded value, due to the development of fluid bridges between the two liquids in contact (Figure 6.8(A)).
- In the second phase a preload, ranging from 300 to 400 Pa, is applied to the active surface (Figure 6.8 (B)).
- In the third phase the recorded values drop under the baseline, reaching a minimum (Figure 6.8 (C)). This minimum is related to the adhesion of the active surface to the wet substrate. The bigger is the gap between the baseline and the minimum value, the higher is adhesion force.

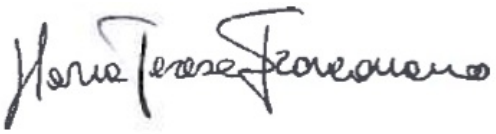

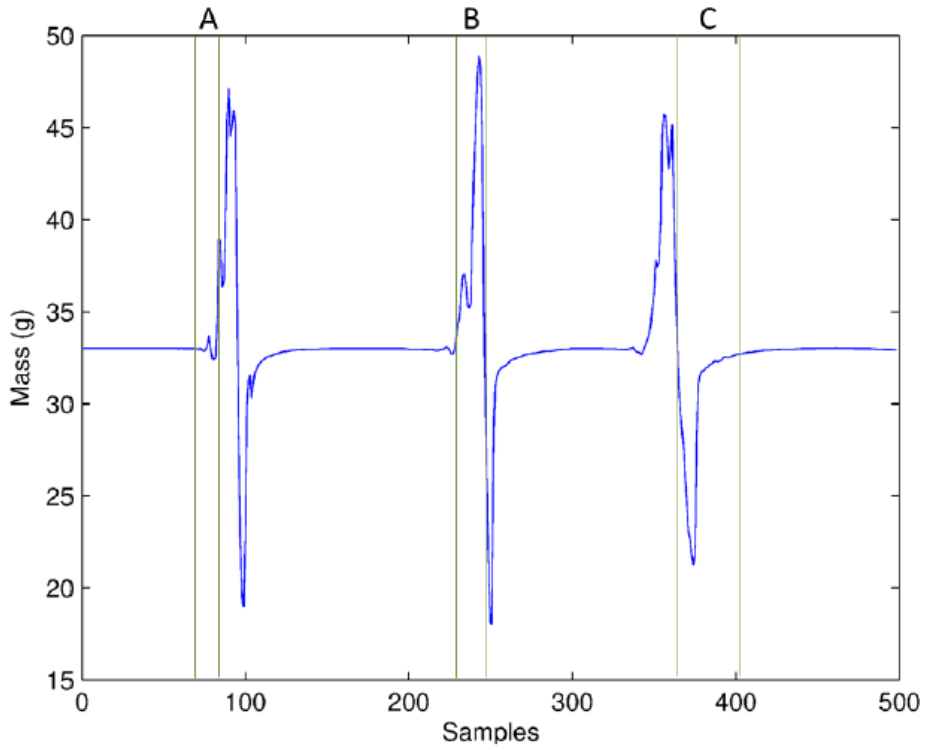

Figure 6.8: Experimental example data. Three phases are highlighted: A) shows a drop of the values under the baseline due to wet adhesion; B) is the preloading phase and C) represents the adhesion phase.

6.2. Results and Discussion

Tests have been performed according to the protocol described in section 6.1.5. Data collected for each of the defined experimental conditions, i.e. patterned/flat PDMS surface and voltage or no voltage supply, have been analyzed and compared with each other. One-way ANOVA tests have been implemented.

The first comparison regards patterned PDMS surface with applied voltage (class 1, Figure 6.9) or no voltage supplied (class 0, Figure 6.9). As shown in Figure 6.9, when voltage is applied, the median value of the measured adhesion force decrease of 58.3 mN/m (-34:9%).

Moreover, being the notches of the boxes not overlapped, the median values of the two classes differ from each other (95% confidence).

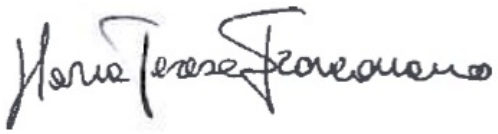

The ANOVA test has been also used to evaluate how surface patterning affects adhesion forces. Experiments have been performed with flat or patterned PDMS surfaces, with no voltage supplied.

For patterned PDMS the pressure is 339.7 Pa, while pressure drops to 248.4 Pa for flat PDMS. This means an adhesion force increase of 36.76% merely due to surface patterning (Figure 6.10).

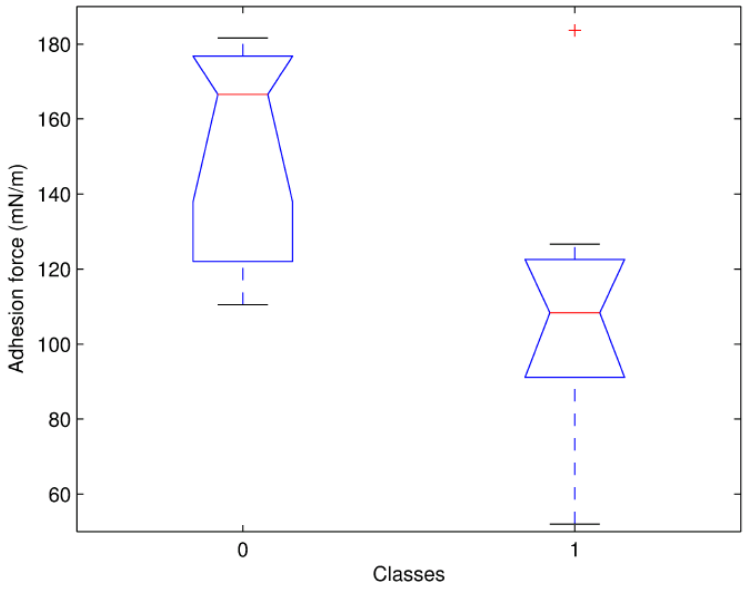

Figure 6.9: One-way ANOVA test applied to patterned PDMS surface. Class 0: no voltage applied; Class 1: 60V applied.

By comparing the adhesion force achieved using flat or patterned PDMS surface when the voltage is applied (Figure 6.11) an increase of 16% is noticed (due to both wet adhesion and channels walls polarization).

A further comparison, shown in Figure 6.12, between the two kinds of polymeric surfaces (i.e. flat and patterned), leads to the conclusion that difference in the adhesion force between patterned and flat surface is negligible if voltage is applied. This means that the adhesion promoted by micropatterns can be controlled by the application of an electric field: by applying a voltage, a patterned polymeric surface behaves like a flat one, showing a similar decrease in the adhesion force.

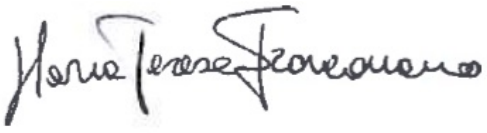

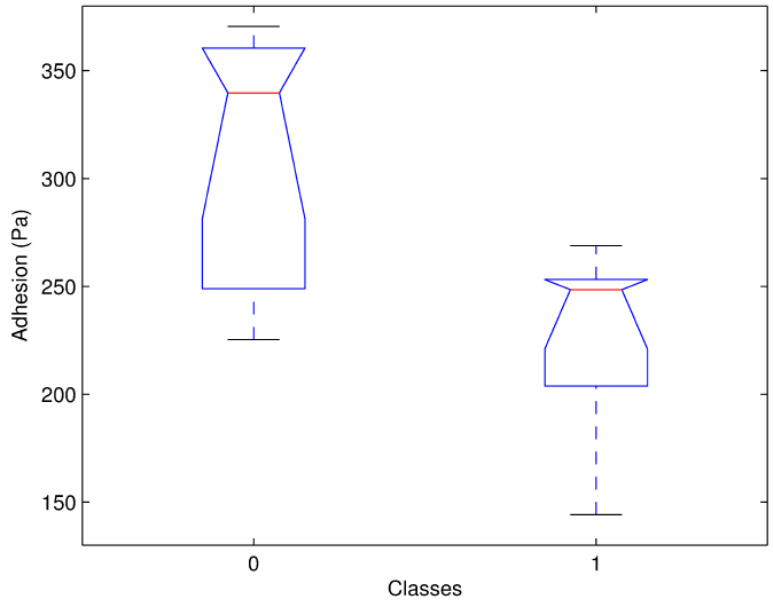

Figure 6.10: One-way ANOVA test, related to data obtained when voltage is not applied, both for patterned (Class 0) and flat (Class 1) PDMS layers. For the patterned PDMS layer, a nominal pressure has been evaluated considering as total contacting area: 5.66 cm^2.

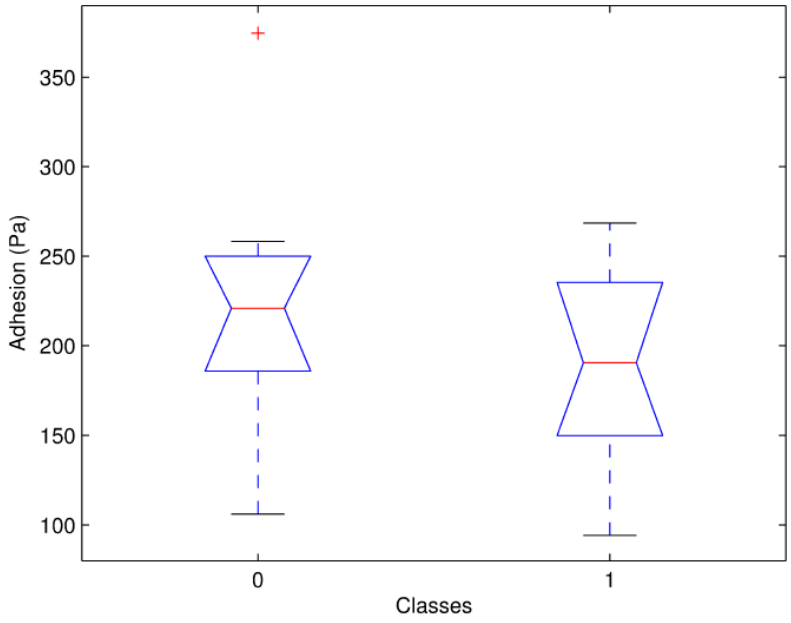

Figure 6.11: One-way ANOVA test, related to data obtained when voltage is applied, both for patterned (Class 0) and flat (Class 1) PDMS layers. For the patterned PDMS layer, a nominal pressure has been evaluated considering as total contacting area: 5.66 cm^2.

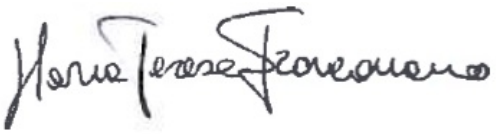

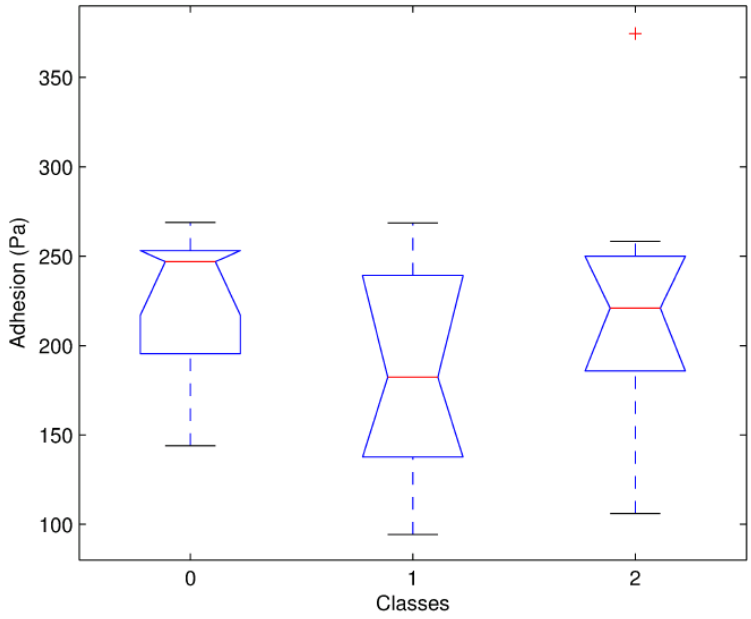

Figure 6.12: Comparison between trials performed using a flat PDMS layer, when voltage is applied (Class 1) and not (Class 0), and using a patterned PDMS layer when voltage is applied (Class 2).

6.3. Conclusion

A method for actively controlling the adhesion force on wet surfaces by means of electric fields, has been proposed and tested.

An active surface, including a glass substrate with interdigitated electrodes on top, and a micropatterned covering layer (in PDMS) has been fabricated and tested.

Results showed that a significant decrement in the adhesion force (34.9%) (Figure 6.9) occurs if an electric field is applied.

By comparing trials performed with polarized patterned PDMS layers and flat ones, it is possible to infer that the patterned surface behaves like the flat one (Figure 6.12). Therefore a sort of 'virtual smoothness' of polarized PDMS is observed.

The developed active surface, currently available on a rigid substrate (i.e. glass), can be easily developed on flexible (Chapter 5) or stretchable substrates (Chapter 7), thus enabling its integration on curved surfaces (e.g. robotic fingers).

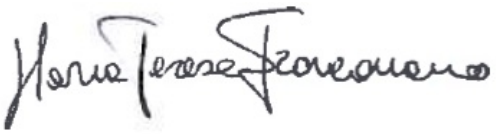

Bibliography

[Accoto, 2012] Accoto D., Francomano M. T., Esposito C., (2012). Dispositivo e metodo per adesione controllata su substrato umido (Device and method for controlling adhesion on wet substrates). RM2012A000026.

[ASG, 2003] American Society for Gastrointestinal Endoscopy Assessment Committee. Gastrointest. Endosc. 2003, 60, 327-333.

[Barnes, 2007] Barnes, W. J. P. Science, 2007, 318, 203–204.

[Bernard, 2001] Bernard, L.; Doyle, J.; Friedlander, S. F.; Eichenfield, L. F.; Gibbs, N. F.; Cunningham, B. B. Arch. Dermatol. 2001, 137, 1177–1180.

[Buselli, 2010] E. Buselli, V. Pensabene, P. Castrataro, A. Menciassi, and P. Dario, Evaluation of friction enhancement through soft polymer micro-patterns in active capsule endoscopy, Institute of Physics Publishing: Measurement Science and Technology, 21 (2010).

[Dirks, 2010] J. H. Dirks, C. J. Clemente, and W. Federle, Insect tricks: two-phasic foot pad secretion prevents slipping, Journal of the Royal Society: Interface, 7 (2010), pp. 587.593.

[Dodou, 2007] D. Dodou, A. del Campo, and E. Arzt, Mucoadhesive micropatterns for enhanced grip, IEEE EMBS, (2007).

[Gillett, 1932] Gillett, J. D.; Wigglesworth, V. B. Proc. R. Soc. London B, 1932, 111, 364–376.

[Gorb, 2000] Gorb, S.; Jiao, Y.; Scherge, M. J. Comp. Physiol., A 2000, 186, 821–831.

[Guvendiren, 2008] Guvendiren, M.; Messersmith, P. B.; Shull, K. R. Biomacromolecules 2008, 9, 122–128.

[Kamino, 2008] Kamino, K. Mar. Biotechnol. 2008, 10, 111–121.

[Lee, 2007] H. Lee, B. P. Lee, and P. B. Messersmith, "A reversible wet/dry adhesive inspired by mussels and geckos", Nature Letters, vol.448, pp. 338-341, 2007.

[Majumder, 2007] Majumder, A.; Ghatak, A.; Sharma, A. Science 2007, 318, 258–261.

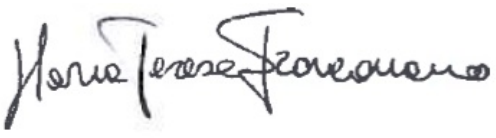

[Majumder, 2010] A. Majumder, A. Sharma, and A. Ghatak, "A Bioinspired Wet/Dry Microfluidic Adhesive for Aqueous Environments", Langmuir 2010, 26(1), 521–525.

[Mugele and Baret, 2005] F. Mugele and J.-C. Baret, Electrowetting: from basics to applications, Journal of physics: Condensed matter, (2005).

[Nguyen, 2007] Nguyen, W.; Byrd, E.; Alshed, D.; Chin, J.; Clerici, C.; Martin, J. J. Adhes. 2007, 83, 587–610.

[Pelrine, 2010a] R. E. Pelrine, H.Prahlad, J. S. Eckerle, R. D. Kornbluh, and S. Stanford, Electroadhesive devices, United States Patent, Pub. No. US 2010/0271746A1 (October 28, 2010).

[Pelrine, 2010b] R. E. Pelrine, H. Prahlad, J. S. Eckerle, R. D. Kornbluh, and S. Stanford, Electroadhesion, United States Patent, Pub. No. US 2010/0027187A1 (February 4, 2010).

[Qian, 2006] J. Qian, H. Gao, 'Scaling effects of wet adhesion in biological attachment systems', Vol. 2(1), pp. 51-58, 2006.

[Tayolor, 2010] G. W. Tayolor, A. Neville, D. G. Jayne, R. Roshan, T. Lisikiewicz, A. Morina, and P. Gaskell, Wet adhesion for a miniature mobile intra-abdominal device based on biomimetic principles, Journal of Mechanical Engineering Science, 2010, pp. 1473-1485.

[Verma, 2006] Verma, M. K. S.; Majumder, A.; Gahtak, A. Langmuir 2006, 22, 10291–10295.

[Wiegemann, 2005] Wiegemann, M. Aquat. Sci. 2005, 67, 166–176.

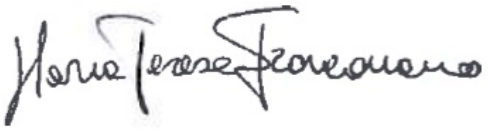

Chapter 7

Stretchable sensorized skin for prosthetic hands

As detailed in Chapter 2, the sense of touch is of paramount importance in the field of robotic manipulation, since it is central in the characterization of both static and dynamic events occurring at the interface between robotic fingers and manipulated objects.

In Chapter 5 artificial slip sensing is addressed. The thermal slip sensor detailed there is not able to discriminate contact events from slip events. To overcome this limit, it is sufficient to employ an additional sensor responsive to pressure, and not to slip.

As mentioned in Chapters 2 and 4, it is also important that sensors cover a large area, in order to attain an adequate spatial acuity. The distribution of the sensors over a large area, in turns, asks for adequate mechanical compliance, for accommodating all movements of the fingers, especially over the knuckles.

To this aims, a stretchable artificial skin, embedding pressure sensors, has been developed and detailed in the following paragraphs[11].

[11] This work was conducted during the candidate 5-month research stay at Prof. S.P. Lacour's lab, EPFL, Switzerland and was a collaborative effort between the LASA, EPFL (Prof. A. Billard's lab) and gmTronics (an Analog Electronics company in Geneva). The author was in charge of the sensor matrix development and testing.

7.1. Flexible versus stretchable substrates

A mapping is said to be *isometric* if, according to a selected metrics, it preserves the distance between any two points.

Therefore, a one-to-one mapping **f** of a surface **S** onto a surface **S*** is called *isometry* if the length of an arbitrary arc on **S** is equal to the length of its image on **S***.

If **f** is an isometry from **S** to **S***, then $\mathbf{f}^{-1}$ is an isometry from **S*** to **S**, and the surfaces **S** and **S*** are said to be *isometric*.

Pure bending deformations, where there is no stretching or shrinking of fibers, are examples of isometries.

Gauss' *Theorema Egregium* is the main analytical tool for establishing whether two surfaces can be obtained from each other by bending without stretching. The Theorem can be stated as follows: if **f**: **S**→**S*** is a local isometry, then Gauss curvature of **S** at P equals Gauss curvature ($\boldsymbol{\kappa}$) of **S*** at **f**(P).

The Gauss Curvature ($\boldsymbol{\kappa}$) is defined as the product of the two principal curvatures of a surface (k_1 and k_2): $\boldsymbol{\kappa}= k_1 \times k_2$.

Gauss' Theorem implies that a deformation, which does not produce stretching or shrinking, preserves the product of the principal curvatures at any point on **S**. In other terms, Gaussian curvature of a surface is an invariant under isometries.

If two surfaces are characterized by different Gauss curvatures, they cannot be isometrically (i.e. without stretching) deformed into each other. As an example, a spherical surface with radius R ($\boldsymbol{\kappa}= 1/R^2$) cannot be deformed into a plane, a cylinder or a cone ($\boldsymbol{\kappa}= 0$) without stretching.

Originally planar microsystems should be stretchable if they should accommodate surfaces with both curvatures different from zero. This problem, for instance, often occurs if skin-like sensors should cover a prosthetic hand with a complex surface (i.e. not just cylindrical or flat, as above the knuckles).

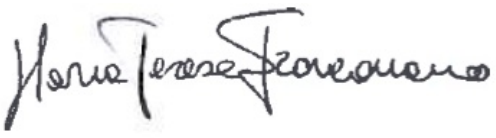

7.2. Stretchable materials

Stretchable systems include a substrate and a set of conductors, equally responsible of the stretchability of the device.

The principal materials used in stretchable systems are [Fjelstad, 2011]:

- **Nitrile rubber** (NBR), which has good elastic properties and a good temperature range (–40°C to +125°C). It is oil resistant, which makes it suitable for automotive as well as for non-latex glove applications.
- **Poly-dimethylsiloxane** (PDMS) is the most used material. It shows several desirable properties: *i)* it can be filled with other materials, thus changing its electrical/thermal properties; *ii)* it is biocompatible and it has a high thermal resistance; iii) it is transparent, with excellent optical stability; iv) it can be used for 2D/3D moldings.
- **Thermoplastic polyurethanes** (TPU) are another potential material for stretchable circuits. TPU films are extremely tear and abrasion resistant as well as highly stretchable (more than PDMS). Moreover, they have good low-temperature performance and good mechanical properties combined with high elasticity.
- **Metal conductors**. Making conductors stretchable is a complex issue. As a result, there have been a number of different investigations and developments in this area (section 7.3). Proposed solutions are mainly based on novel design strategies as well as on the development of new conductor materials (e.g. composiste conductors).
- **Composite conductors**. In addition to metal foils, a great effort has been paid for the development of new composite materials (i.e. metals mixed with a stretchable polymer; section 7.3) The conductivity of these mixtures is lower than metals, but they are more stretchable. One of the challenges is that these solutions do not tend to be solderable.

7.3. Stretchable technologies

Stretchable technologies refer to electrical and electronics circuits/devices that are elastically or inelastically stretchable by more than a few percentage, while retaining their functions [Kim, 2008].

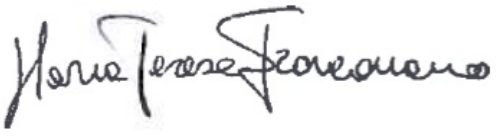

There are three main ways for stretching devices (Figure 7.1):

- Linear stretching: two prospicient ends are pulled in opposite directions.
- Two-dimensional (2D): linear stretching in two perpendicular directions is simultaneously applied to the device.
- Three-dimensional (3D) stretching: a two-dimensional stretching is applied to the device while it is also wrapped around a 3D object.

The several difficulties and challenges associated to the development of completely stretchable devices lead also to the investigation of hybrid solutions, where stretchable components are combined with rigid or bendable parts.

The first stretching solutions were mainly employed for developing electrical connections, accommodating the movements of actuated parts. The connections were obtained by folding flexible circuits in an accordion-like manner (i.e. out-of-plane stretching) [Fjelstad, 2011].

Currently, some of the proposed solutions for stretchable devices are based on carbon nanotubes [Hansen, 2007] or nanoparticle implantation within elastomers [Urdaneta, 2007; Corbelli, 2011] as well as on nanotube composites, which appear very promising [Sekitani, 2008].

A completely different approach is based on obtaining the desired mechanical properties not through new materials but through new structural configurations of the established ones.

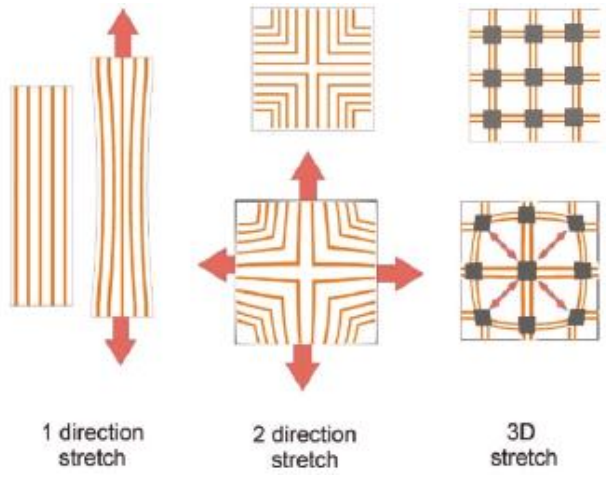

Figure 7.1: Ways of stretching [Fjelstad, 2011].

Maria Teresa Francomano

It has been demonstrated that, although thin metal films can sustain only small strain (~1%), if they are placed on the top of an elastic substrate, during stretching, multiple microcracks are formed in the metal [Lacour, 2006]. The organization of cracks and/or folds strongly reflects the strain field in the membrane. Parallel wrinkles (cracks) emerge under uniaxial compression (tension), whereas a large diversity of motifs may be obtained under more complex strain fields [Lacour, 2003; Lu, 2007; Gonzalez, 2011]. This technique allows deformations up to 50%. Drawbacks of this technique are the electrical restrictions of extremely thin metal films, the need for high cost equipment and the processing of nonstandard assembly technology on those substrates. Furthermore, the number of microcracks increases as the substrate is deformed and therefore, a change in the resistance of the patterned conductive lines is observed. Some applications of this technology include electronic circuits used for skin electronics [Lumelsky, 2001] and microelectrode arrays used for monitoring the neuron activity in the brain [Yu, 2007].

Beside the aforementioned solutions, there are other techniques and design strategies for improving stretchability, as detailed in the following paragraphs.

7.3.1. Wavy layouts

Ultrathin material structures formed into 'wavy' geometries offer stretchability without inducing significant strains in the materials themselves [Baca, 2008; Sun, 2007].

There are two basic types of out-of-plane wavy layouts on stretchable supports (Figure 7.2).

The first one (Figure 7.2 (a)) consists in depositing the thin metal film on a pre-stretched substrate. It is reported that once the substrate is released, mechanical relaxation creates 'wavy' configurations, with wavelengths and amplitudes that depend primarily (but not exclusively) on the elastic properties of the substrate as well as on its thickness [Jiang, 2007; Kim, 2008b]. Even though this unique design offers a controllable stretchability without losing electrical performance, it is limited to relatively small circuits and deformation of only a few percent. Some

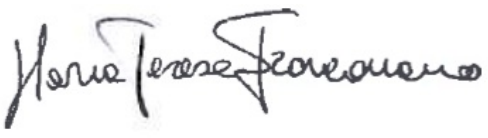

of the earliest results used spontaneous buckling patterns due to the evaporation of thin films of gold onto PDMS [Lacour, 2006].

Figure 7.2 (b) shows the second type of wavy configuration [Sun, 2007]. Here, patterned sites of adhesion on the substrate and/or the ribbon create localized bondings. The non-bonded regions can delaminate from the substrate as the substrate prestrain is released. The main advantage of this second type of structure is that it offers control over the buckling period in a way that allows its optimization for higher stretchability. With such an approach, it is possible, in fact, to achieve reversible stretching up to 100% strains or even more, the maximum tensile stresses being often limited only by cohesive fracture of the elastomeric substrate [Sun, 2007]. These structures can be implemented in ribbons, membranes or wires of various materials.

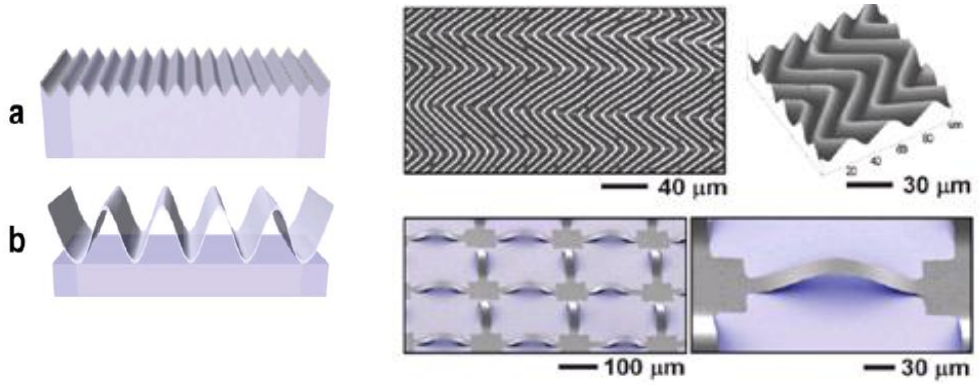

Figure 7.2: Out-of-plane wavy layouts. Waves are generated: (a) by prestrain and release, after metal thin film deposition, of the substrate; (b) by non-bonded laminated regions.

Although out-of-plane stretching may be useful in several applications, current efforts are focused on developing devices able to be stretched in-plane, for taking advantage as much as possible of their thin profile.

Therefore, planar 2D thin metal springs are usually patterned on silicone elastomers. FEM analyses are widely used to characterize the shape of the conductors in order to allow high deformations without permanent damage.

Figure 7.3 shows an example of a thin embedded die and the metal interconnections before and after releasing from the wafer [Gonzalez, 2011]. Here, a specific design of metal lines with a sinusoidal shape allows to stretch

Maria Teresa Francomano

them in a 2D spring fashion. The stretchability of these interposers does not exceed 10%.

In Figure 7.4 a similar example is also reported [Gonzalez, 2011].

In order to keep electrical resistance low and to increase, at the same time, the stretchability of the meanders, multiple sinusoidal lines, parallel to each other, are designed (Figure 7.4). In this case, electrical bridges are placed between the tracks in the regions where the lowest deformation is observed (Figure 7.4). These bridges help keeping the continuity of the lines after failing in a specific region: if a metal track fails, only one section of the line is lost (between two bridges). This redundancy helps increasing the reliability of the system.

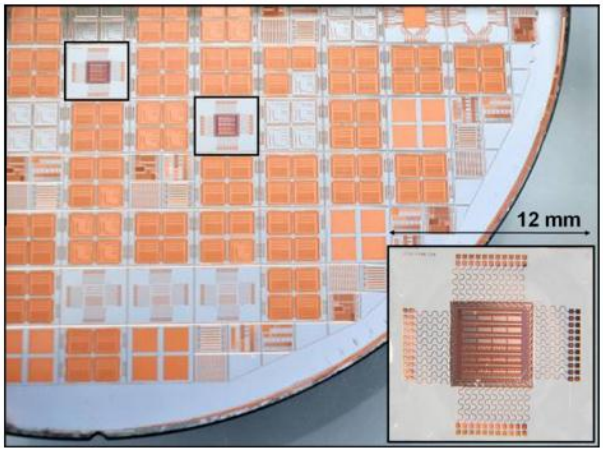

Figure 7.3: Sinusoidal 2D springs for electrical interconnections.

A horseshoe metal track shape has been also proposed [Brosteaux, 2007, Gonzalez, 2008]. In this design, stresses are distributed in a wider region than the apex of the curve.

In some applications, where high density interconnections and low stretchability are required (~40%) a pattern with a zig-zag structure is preferred [Hsu, 2009].

7.3.2. Open meshes

Another approach is based in open meshes [Someya, 2005]. Such devices are developed using bendable materials [Dinyari, 2008]: the strain accommodation is provided by in-plane rotations, with a motion similar to that of scissors [Someya, 2005].

Maria Teresa Francomano

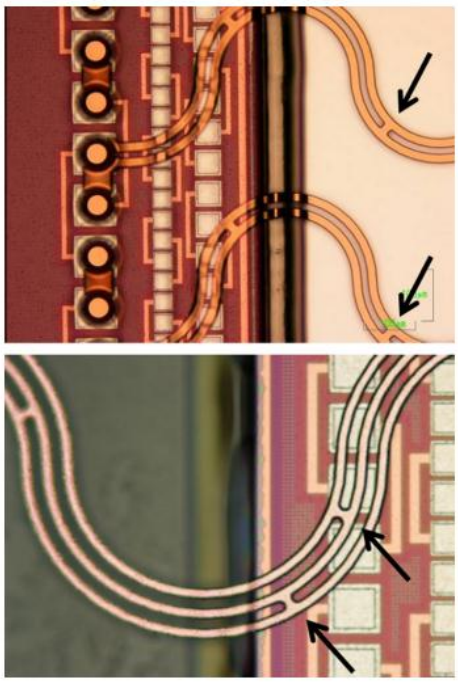

Figure 7.4: 2D spring shaped electrical connections. Arrow indicate the electrical bridges between parallel lines.

Figure 7.5 shows a narrow strip with such a mesh design. Tensile strains applied to the ends of this structure cause the bridges to rotate in a manner that transforms the open squares into rhombuses: the strip lengthens and narrows as a result. Circuits that exploit this principle can use, for example, the bridges for electrical interconnects [Someya, 2005].

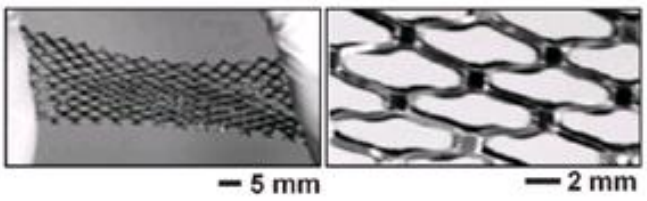

Figure 7.5: Open meshes stretchable interconnections [Kim, 2008].

7.4. Flexible Poliurethane (PU) Foam as stretchable substrate

Stretchable substrates with tunable properties provide an alternative for enabling the development of stretchable devices (e.g. sensorized thin devices, mimicking human skin anatomical and functional heterogeneity).

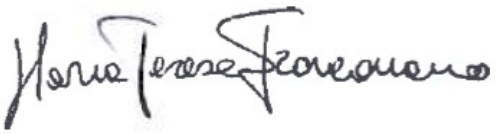

To this aim, recent works (@ LSBI lab, EPFL) have been focused on using a Flexible Polyurethane Foam (FPF) as substrate [Vandeparre, 2013].

FPFs include soft domains (i.e. air-filled cells) inside a relatively stiff domain in polyurethane (PU) (Figure 7.6).

The substrate structure arises spontaneously during the polyurethane foam formation, thanks to the foaming effect of the blowing agent [Vandeparre, 2013].

In particular, layers of FPFs, hundreds of microns thick, have been fabricated using a bar coater set-up (Figure 7.7). A two-component mixture is dispensed within a spacer of a pre-defined thickness and then a sliding bar is rolled over the spacer. During rolling, an overpressure is applied above the foam, which is covered with a flat polyimide foil, thus constraining its vertical expansion. After crosslinking, the foam substrate is peeled off the polyimide substrate [Vandeparre, 2013].

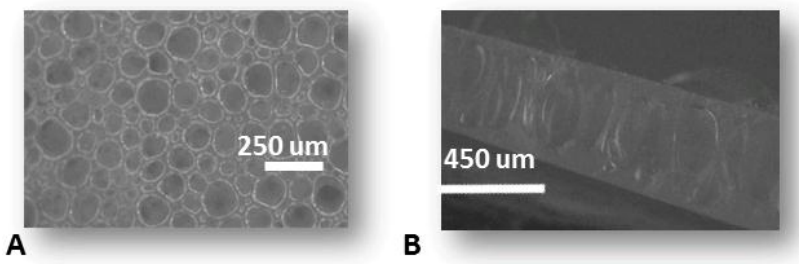

Figure 7.6: FPF layer. A. Top view; B. Cross section.

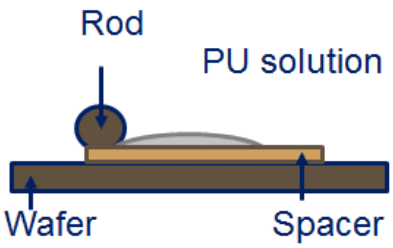

Figure 7.7: Bar coating of a FPF layer.

A variety of 2-component systems are available for the foam production, allowing a wide range of foam densities (Figure 7.8), morphologies and, as a result, also mechanical properties (Figure 7.9).

Maria Teresa Francomano

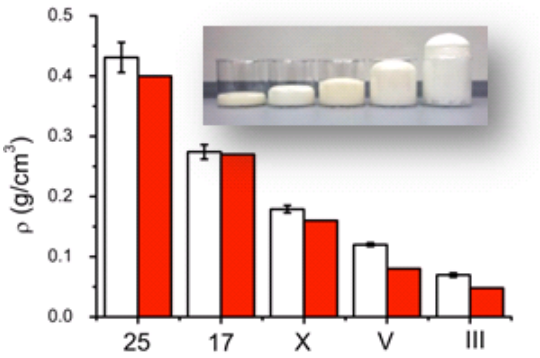

Figure 7.8: Variety of foam densities.

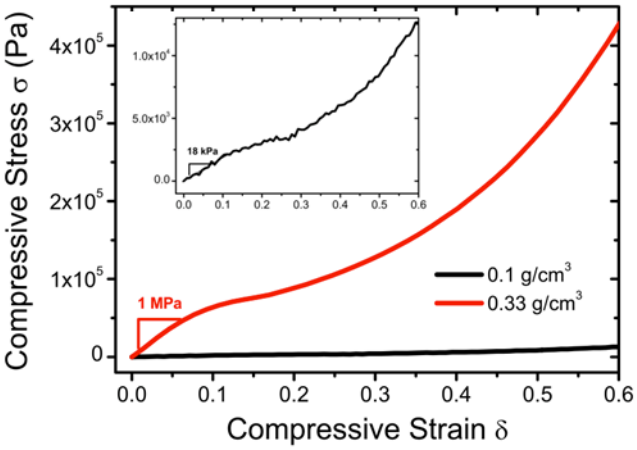

Figure 7.9: Compressive Stress-strain curves of Stiff (Red) and Soft (Black) FPF substrates under tensile loading. PU foam layers with densities of 0.1 and 0.33 g/cm3 have muduli of 18 kPa and 1MPa, respectively [Vandeparre, 2013].

Thin metal films have been coated on this FPF substrate. After deposition, the thin film is uniform and smooth across the film surface (Figure 7.10), while by applying uniaxial cycles of tension/compression to the substrate, a spontaneously generated pattern of localized folds and cracks in the film occurs (Figure 7.11).

Breaking processes, localized above the air cells, guarantee a percolating path of the metal film, which assures the electrical continuity of the patterned tracks (Figure 7.12) [Vandeparre, 2013].

Maria Teresa Francomano

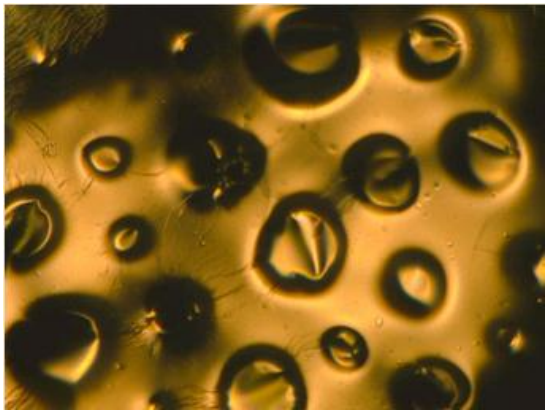

Figure 7.10: Thin gold film deposited on a FPF layer.

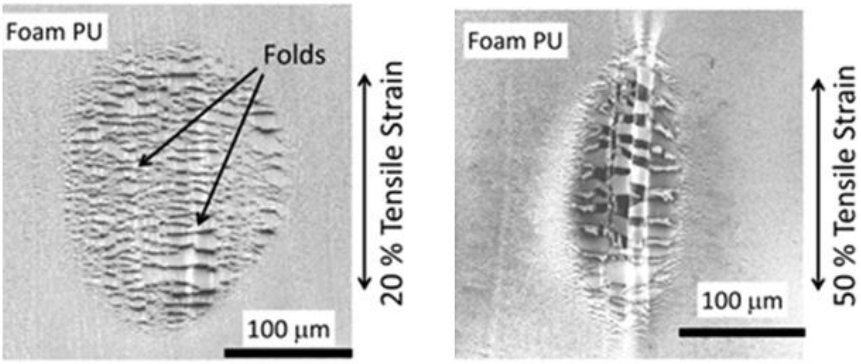

Figure 7.11: Strain localization of metal cracks above air cells (during stretching) [Vandeparre, 2013].

After complete breaking, a honeycomb structure is obtained, which can be compared to open meshes devices (section 7.3.2). The main difference dwells on the presence of a stretchable substrate, instead of a flexible one, so that beside rotation, up to a certain strain, meshes bridges are also extended. This allows larger stretching.

Finally, the stretchability of the metal films on the FPF substrates depends on the foam density: softer foams allow better performance [Vandeparre, 2013].

7.5. Soft Contact/Pressure Sensors on a stretchable PU Foam

A stretchable artificial skin has been designed in order to coat a robotic finger, i.e. two phalanges and two knuckles so that it can nicely accommodate repeated

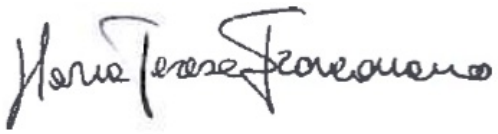

finger movements while monitoring contact in multiple locations along the finger.

The skin is made of FPF layers (section 7.4), with capacitive sensors embedded, in order to detect contact events and pressures during object manipulation.

Preliminary characterization of the capacitive sensors shows that they are able to detect light contact (few kPa) with plastic or metallic objets.

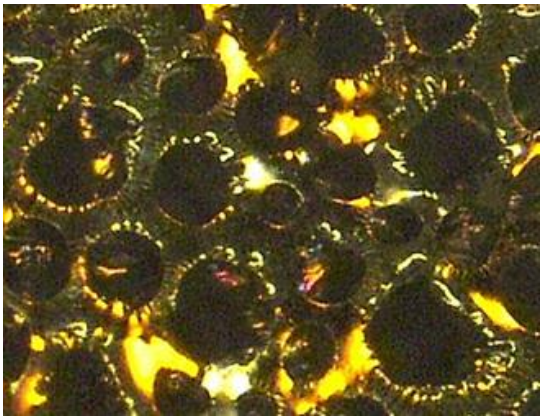

Figure 7.12: Gold path integrity above bulk PU zones, after the application of cyclic uniaxial deformations.

7.5.1. Skin design

The sensory skin is a multilayered structure (Figure 7.13) including four layers of soft polyurethane PU foam and sub-micron thick metallization.

The whole thickness of the skin ranges from 0.8 to 2 mm.

The skin integrates the compliant capacitive sensors with 3.5x1.5 mm^2 surface area, and their readout electronics (Flexible PCBs, FPCBs), developed on a flexible substrate (i.e. polyimide).

The FPCBs are integrated on the second layer of the skin, where sensors pads as well as Ground and AC Shields pads are located. The electrical connection of Ground and AC shield, patterned both above and underneath the second layer, is guaranteed by VIAs.

A schematic of the array is depicted in Figure 7.14 (A).

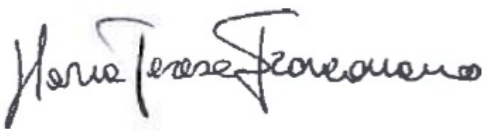

The capacitive sensors are distributed along the finger, i.e. on three sides of the phalanges (two lateral sides and bottom) and above the knuckles (Figure 7.14(B)).

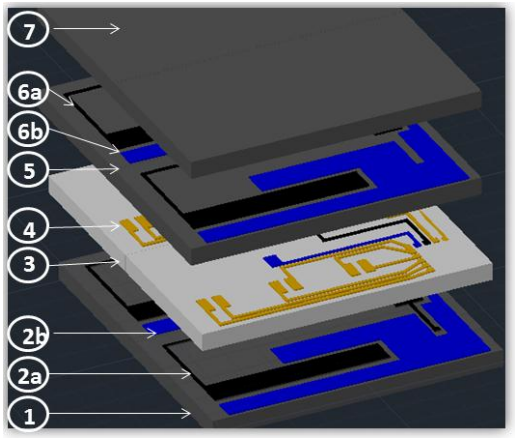

Figure 7.13: 3D rendering of the multilayered skin. From the bottom to the top: the first FPF substrate (1) has Ground (2a) and AC shield (2b) patterned on top, while the active sensing elements (4) are patterned on the second FPF layer (3). The third layer (5) replicates the first one (1), with two metal tracks on top (i.e. Ground (6b) and AC schiels (6a)). Finally a FPF layer (7) convers the structure. The electrical connection of Ground and AC shield along the three layers is guaranteed by VIAs.

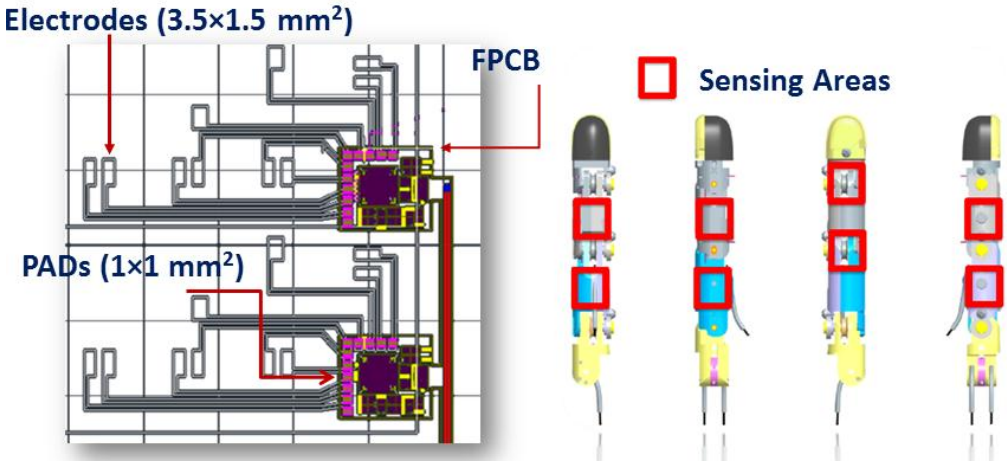

Figure 7.14: A. Schematic of the capacitive sensors array. B. Sensing areas (2 capacitive sensors are present within each area), distributed along a robotic finger.

The main steps of the microfabrication process are detailed in section 7.5.3.

Maria Teresa Francomano

7.5.2. Sensors detection strategy

The skin includes four areas, each with 2 sensing units. The latter consist of two capacitors in parallel. The total capacitance, C, being $C=C_1+C_2$ (Figure 7.15).

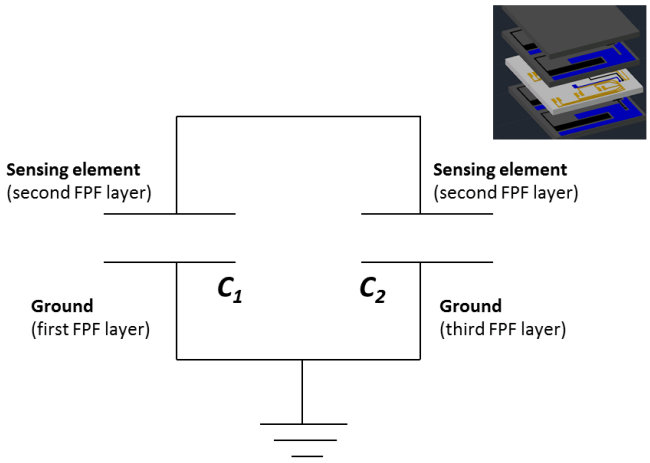

Figure 7.15: Schematic of each sensing unit, whose capacitance is: $C=C_1+C_2$.

The sensing unit is modeled as a deformable capacitor, composed of two highly compliant electrodes with a surface A and separated by a constant distance l_0, as illustrated in Figure 7.16.

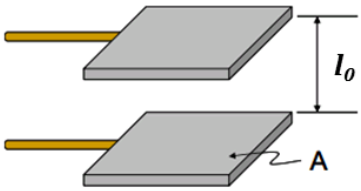

Figure 7.16: Schematic of a planar capacitor.

The PU foam layer between the electrodes provides compliance, and the deformation characteristics of the foam ensure large variations in the capacitance under deformations.

Assuming the electrode area, A, is much larger than the separation distance, l_0, the capacitance of the parallel plate is given by (7.1), where ε_0 is the permittivity of vacuum and ε_r is the relative permittivity of the dielectric material (PU foam). The nominal capacitance, C, is defined as the capacitance without applied stress:

Maria Teresa Francomano

$$C = \frac{\varepsilon_0 \varepsilon_r A}{l_0} \tag{7.1}$$

The length of the sensor is *L* and the width *w*. Therefore (7.1) can be rewritten as:

$$C = \frac{\varepsilon_0 \varepsilon_r L w}{l_0} \tag{7.2}$$

A change in the capacitance may be calculated as a total differential (for small changes):

$$\Delta C = \frac{\delta C}{\delta L}\Delta L + \frac{\delta C}{\delta w}\Delta w + \frac{\delta C}{\delta l}\Delta l \tag{7.3}$$

Assuming *w* constant, the relative change in capacitance is:

$$\Delta C = \left(\frac{\Delta L}{\delta L} + \frac{\Delta l}{\delta l}\right) C_{ref} \tag{7.4}$$

$\frac{\Delta L}{\delta L}$ is the uniaxial longitudinal strain due to stretching, before skin folding around the robotic finger (Figure 7.17). After skin folding, it is assumed that the surface area of the capacitor plates does not change.

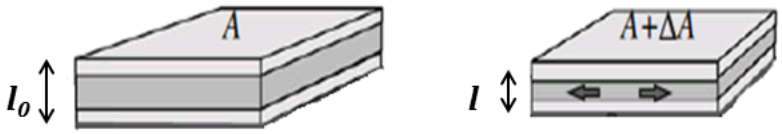

Figure 7.17: Capacitor local deformation resulting in a local change of the electrode area A (A+ΔA).

When the pressure is applied, the material is strained perpendicularly to the capacitive plates. As mentioned, *A* remains constant. Therefore the capacitance variation is merely due to the change in the distance between plates.

The ε_r of the PU foam has been characterized by using the *16451B Dielectric Material Test Fixture* (by Agilent Technologies). The obtained value is $\varepsilon_r = 2.16 \pm 0.20$.

Maria Teresa Francomano

By considering this value and according to the geometrical parameters of the metal plates (3.5×1.5mm^2) as well as to the thickness of each layer (~450 um), one finds that the expected capacitance of each sensing unit is $C = 446.26 \pm 41 fF$.

As reported in Table 7.1, the measured capacitance per sensing unit is comparable with the one expected. Higher variance with respect to the theoretical value (e.g. in correspondence of elements 2 and 6) can be due to the not uniformity of the layers thickness.

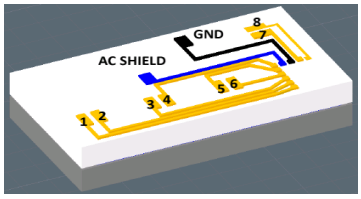

Sensor	C_0 [fF]	Sensor	C_0 [fF]
1	(491.48±0.89)	5	(436.79±0.22)
2	(388.93±0.25)	6	(387.02±0.24)
3	(471.34±0.23)	7	(453.88±0.27)
4	(454.32±0.29)	8	(494.24±0.28)

Table 7.1: Measured capacitance values per each sensing unit.

7.5.3. Skin Fabrication

The main steps of the fabrication process (Figure 7.18) can be outlined as follows:

(1) manufacturing of sub-millimeter thick PU membranes using a bar coater (the process is detailed in section 7.4);

(2) evaporation and patterning of thin Ti/Au films (titanium/gold, 5/25nm thick) for Ground, AC shield and active electrodes;

(3) PU foam multilayer assembly using a polyurethane glue;

(4) bonding of the electronic flexible circuit board.

7.5.4. Experimental tests

Experimental tests have been performed in order to characterize the capacitive sensors.

The sensing elements have been contacted using different materials (i.e. plastic, metal and human skin). Moreover different pressures have been applied in order to preliminarily characterize the capacitance variation.

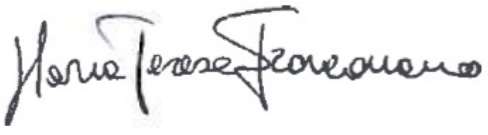

The experimental set up is described in section 7.5.4.1, while results are reported in section 7.4.4.2.

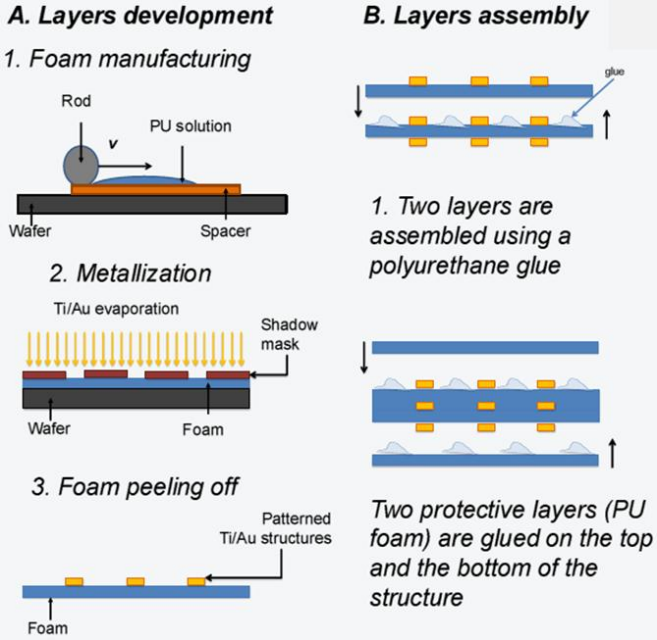

Figure 7.18: Main steps of the sensorized skin fabrication process.

7.5.4.1. Experimental set-up[12]

The experimental set-up (Figure 7.19) includes: a flexible PCB (FPCB), integrated on the second layer of the skin (Figure 7.14A); a custom board, which connects the FPCB to an evaluation kit, the *AD7147 CapTouch evaluation board kit* (by Analog Devices). The evaluation kit is connected through USB to a workstation, running the *CapTouch software* (by Analog Devices).

Capacitance values, from each sensing units can be displayed and recorded, for further elaborations.

[12] The readout electronics has been developed by gmTronic (Geneva, Switzerland).

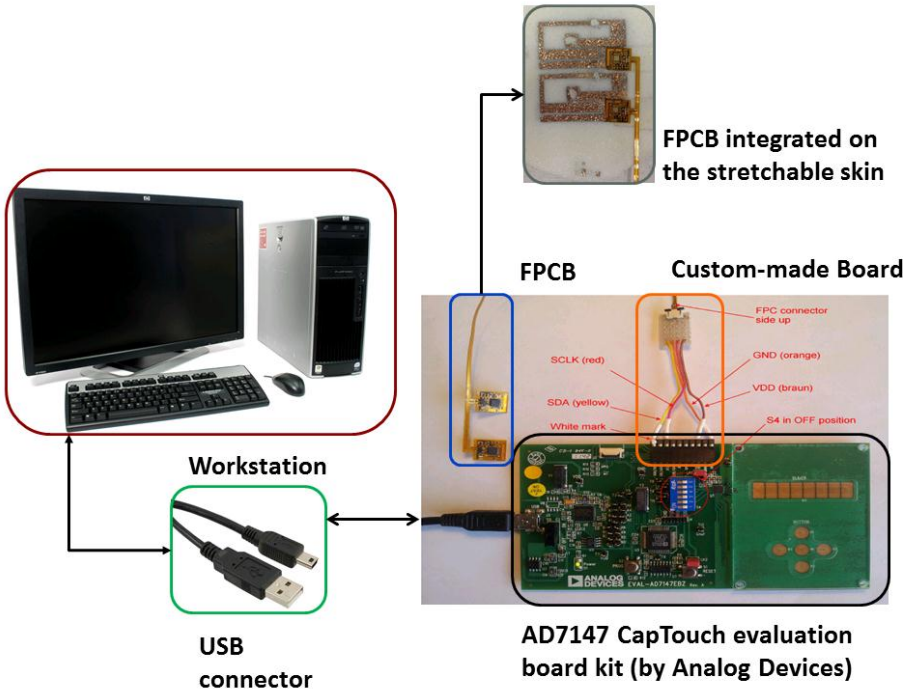

Figure 7.19: Experimental set-up for capacitance measurements.

The AD7147 evaluation board, whose block diagram is reported in Figure 7.20, is powered via the USB connection. The evaluation software allows data to be read from and written to the AD7147.

The main component on the board is the AD7147 AD converter. It is connected to six capacitance sensors (one slider and five buttons) and allows the user to evaluate a variety of sensors that may be suitable for a particular application. Anyhow, it is possible to disconnect the AD7147 via switches. This allows the user to plug an external sensor PCB into the evaluation board via the ZIF connector, J2, or edge connector, J1.

The external sensor board must have an AD7147 mounted on it. It is not possible to use the AD7147 that is located on the evaluation board with external sensors.

An ADuC841 microcotroller, included in the evaluation board, can be used for host communication to an AD7147 on an external sensor board.

The VDD signal goes through an ADP3303 voltage regulator (3.3 V output) before being distributed around the board.

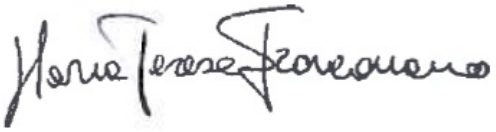

An USB noise suppression chip helps reducing noise on the D+ and D− USB signals. Finally the LED indicates whether power is active or not.

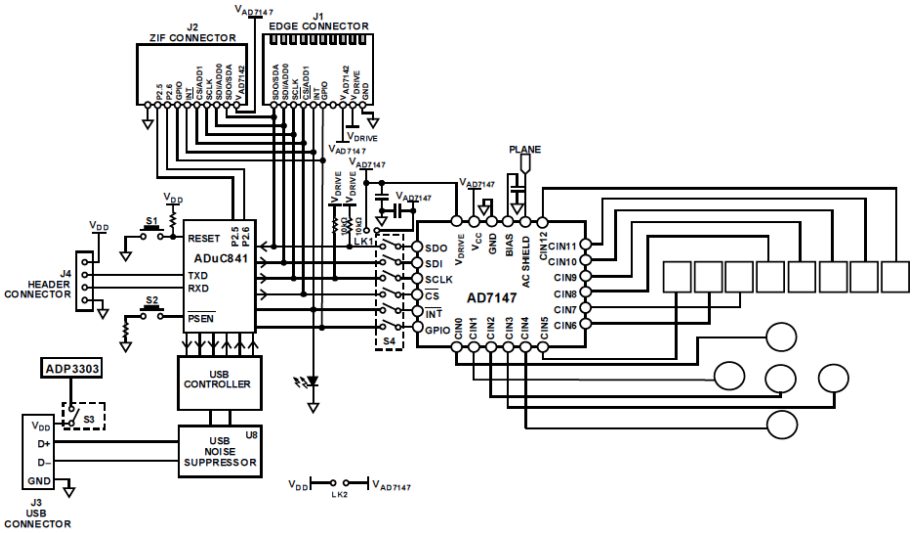

Figure 7.20: Block diagram of the AD7147 evaluation board [AD7147 Datasheet].

The AD7147 Eval Kit is connected to the FPCB by a custom-made board (HandConnector PCB). The latter is connected to the evaluation board via J1 connector (Figure 7.20).

Each FPCB (Figure 7.21 (A)) is 200 µm thick and is connected to the HandConnector PCB by means of a flex wire. The latter is 2.5 mm wide, 150 mm long, 300um thick and hold 4 connections endings, as shown in Figure 7.21 (B).

Each FPCB can read signals from 8 sensing units and it consists of:

- 10 pads (Figure 7.21 (C)): 8 for the capacitive sensors, 1 for the AC-shield and 1 for the Ground (GND) (see section 7.5.1.).
- AD7147-1, for capacitance measurements.
- 1 linear regulator (ADP121-AUJZ30, by Analog Devices) for low noise measurement.
- 1 LED, for debugging purpose.
- 1 reference SMD capacitor, for calibration purpose.
- 4 selectable I2C addresses using 2 resistor jumpers.

A schematic of the electrical circuit of the FPCB is reported in Figure 7.22.

Maria Teresa Francomano

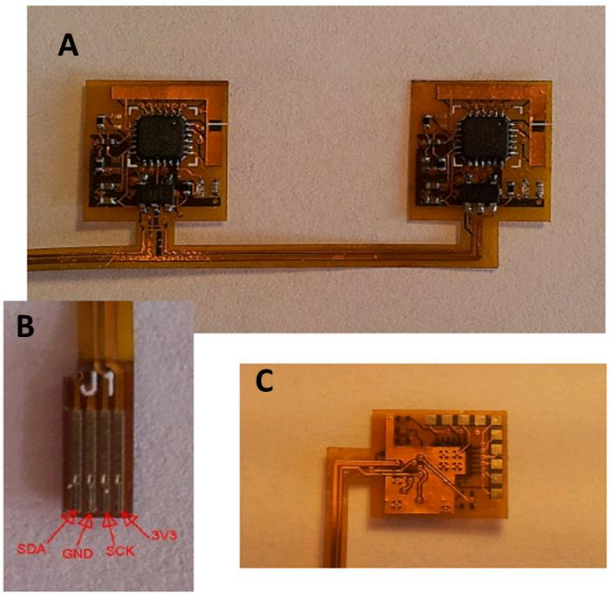

Figure 7.21: A. Snapshot of two FPCBs (one per each phalanx); B.The 4 connections endings of the FPBC, to be connected to the custom-made board; C: Back side of one FPCB, showing PADs.

The FPCBs as well as the custom-made electronic board (HandConnector PCB) designs and development have been accomplished by gmTronic (Geneva, Switzerland).

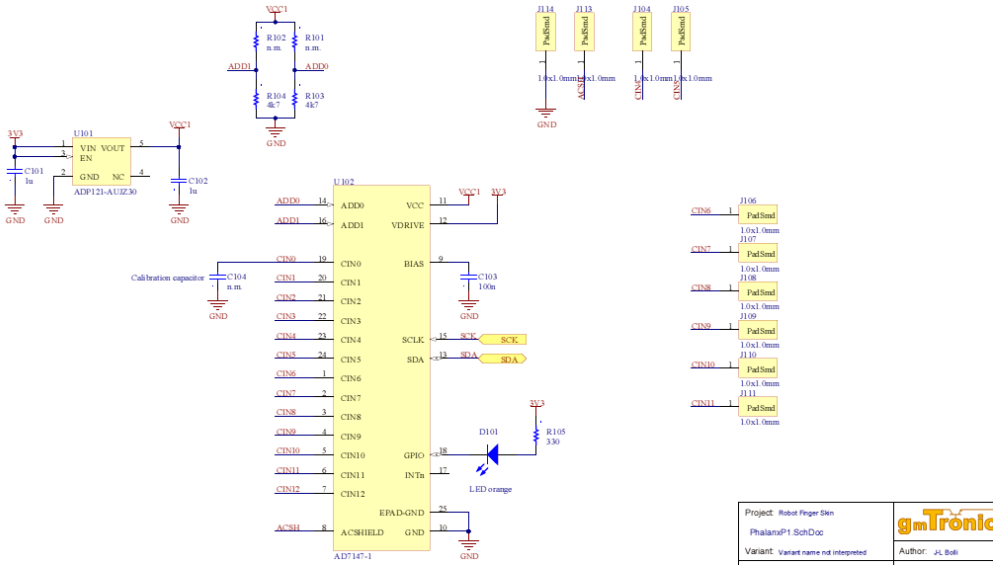

Figure 7.22: Block diagram of the FPCB.

7.5.4.2. Results and Discussion

The capacitive sensors can detect light hand pressed contacts with objects made of plastic, metal and fingers.

A threshold control and a custom made interface allows to intuitively display the touched sensing element (Figure 7.23).

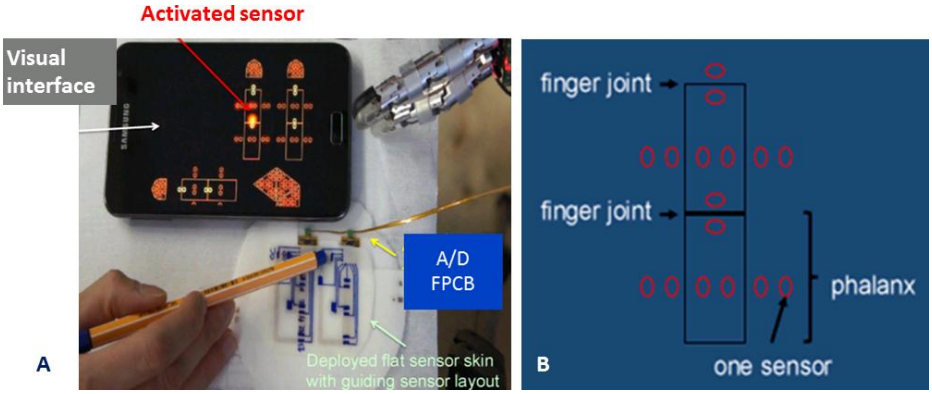

Figure 7.23: Contact tests. A. The sensorized skin is connected to the control of a robotic hand (i.e. the iCub left hand); by means of a visual interface (B) [13]it is possible to identify the touched sensing element.

The sensors have been preliminarly characterized by applying a pressure range of 0.5-5.3kPa, using testing weights.

The minimum detectable pressure is 1.2 kPa. Figure 7.24 shows the obtained calibration curve.

As expected, by increasing the applied pressure, the capacitance variation increases, due to the decrease of the distance between capacitor plates.

Considering the skin design (section 7.5.2), the capacitance C is:

$$C = C_1 + C_2 = 2C_1 \tag{7.6}$$

When pressure is applied to the soft capacitors, the distance, *d*, between the parallel plates varies (Figure 7.25):

[13] The user inerface has been developed by the LASA (head of the lab: Prof. A. Billard), EPFL.

Maria Teresa Francomano

$$d = d_1 = d_2 = d_0(1 - \xi) \tag{7.7}$$

where ξ is the deformation (compressive strain), depending on the applied pressure (P) and the PU foam layer Young Modulus (E)[14]:

$$\xi = \frac{P}{E} \tag{7.8}$$

According to (7.8), C_1 can be expressed as:

$$C_1 = \varepsilon_0 \varepsilon_r \frac{A}{d_1} = \varepsilon_0 \varepsilon_r \frac{A}{d_0 - \xi d_0} = \frac{C_0}{1 - \xi} \tag{7.9}$$

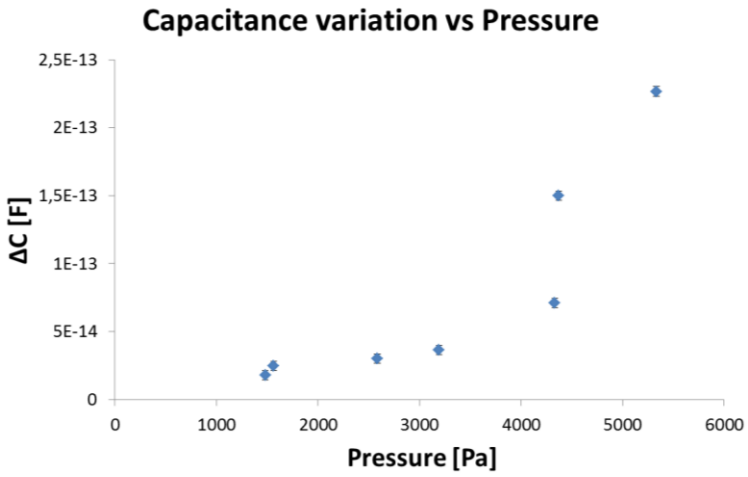

Figure 7.24: Capacitance variations (with respect to the measured capacitance when no pressure is applied) occurring in correspondence of one of the sensing unit, versus applied pressures. Ten measurements have been performed per each applied pressure value.

The total capacitance variation is then:

$$\Delta C = C - 2C_0 = \frac{2C_0 \xi}{1 - \xi} \tag{7.10}$$

Equation (7.10), according to (7.8), can be expressed as:

[14] For simplicity sake, the absolute value of strain is considered here.

Maria Teresa Francomano

$$\Delta C = 2C_0 \frac{P}{E - P} \tag{7.11}$$

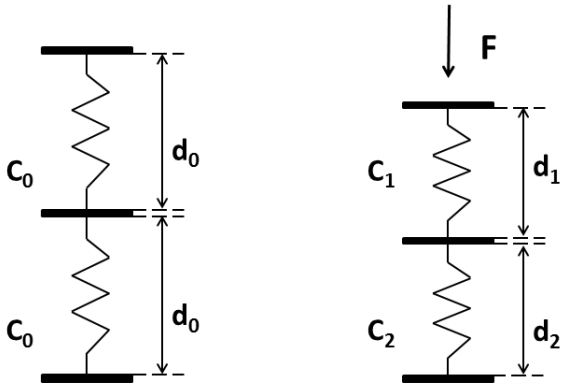

Figure 7.25: Schematic of soft capacitive sensors deformation when a force F is applied.

Figure 7.26 shows the fitting of the experimental data, by interpolating (7.11). The minimum RMS is obtained by using C_0=190fF and E=1.26kPa. Both values are in good agreement with experimental values (Table 7.1 and Figure 7.9).

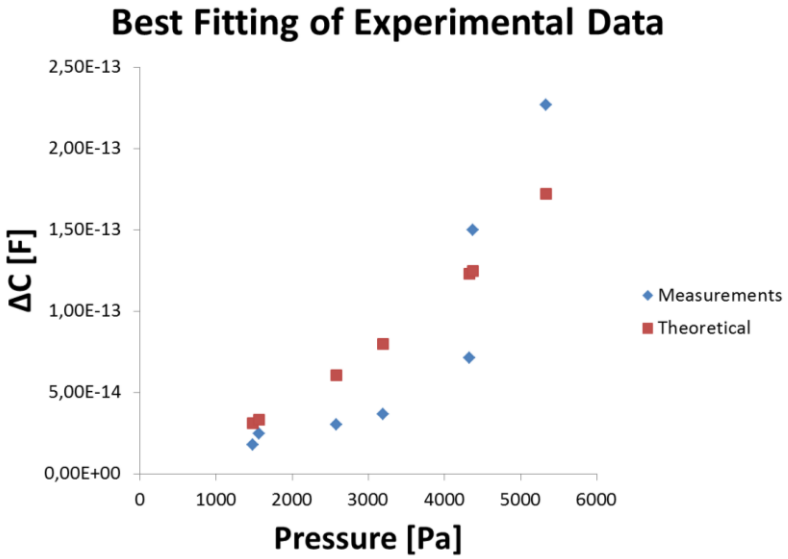

Figure 7.26: Best fitting of experimental data. The minimum RMS is obtained by using C_0=190fF and E=1.26kPa.

Figure 7.27 shows an example of data obtained during one trial, applying increasing pressure values on the same sensing unit.

Maria Teresa Francomano

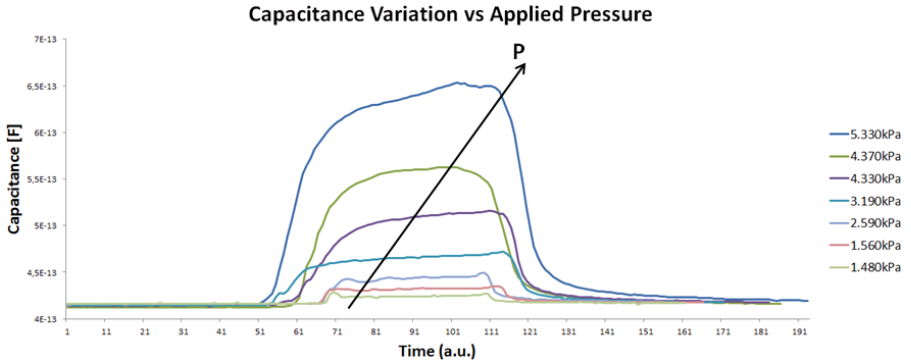

Figure 7.27: Example of data obtained during one trial when different pressure are applied on the same sensing unit.

Multiple contact tests have also been performed, showing that cross talking among the sensing areas does not occur.

Figure 7.28 depicts an example multiple contact test. Here two values of pressure are applied simultaneously: 2.59kPa above the sensing element n.1 and 4.33kPa above the sensing element n.8.

The major capacitance variations occur in correspondence of the touched units. Although the units within the same sensing area registered a "side" capacitance variation (which is lower than the one measured on the directly involved units), the sensing element of the other areas of interest are not affected.

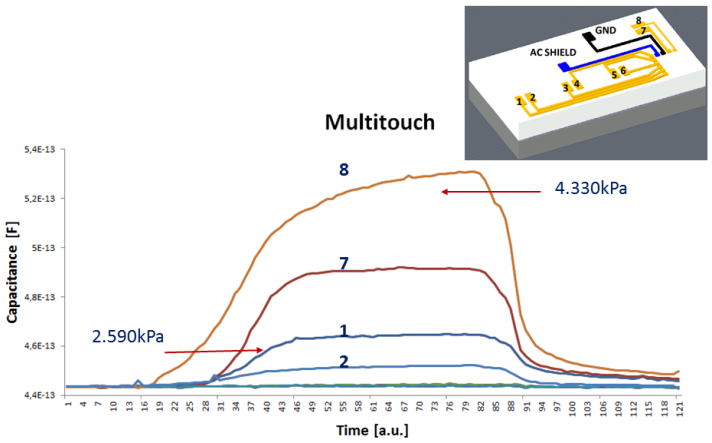

Figure 7.28: An example of multitouching. A pressure of 2.59kPa is applied to the sensing unit n.1, while a pressure of 4.33kPa is applied to the unit n. 8. The pressure is applied simultaneously to the two different units.

Maria Teresa Francomano

Finally, when the skin is stretched by about 10%, the reference capacitance C_0 increases by about 19% and similar contact is reliably detected (Figure 7.29).

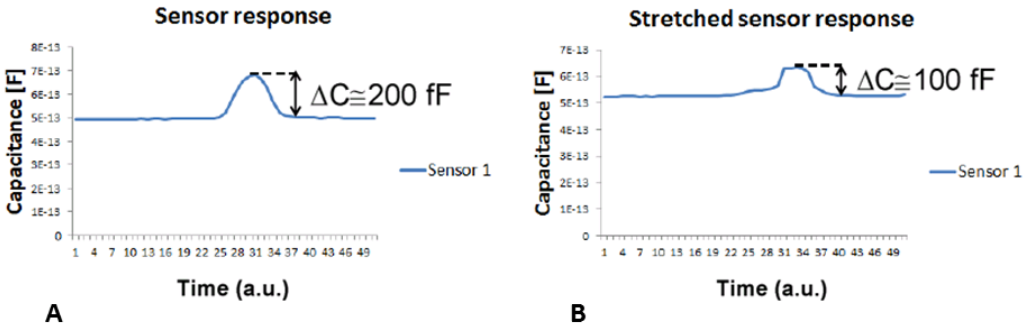

Figure7.29: On-off sensor response, once pressed by human finger. A. Sensor response if the skin is flat; B. Sensor response if the skin is stretched uniaxially by 10%.

7.6. Development of Crystalline Foams

In order to have substrates mapping the desired and pre-defined mechanical properties, it is necessary to develop the foam layers in a controlled way.

Recently, the generation of bubbles with well controlled sizes have been achieved using microfluidic devices, [Marmottant, 2009] consisting of micrometric channels with specific geometries to mix two fluid phases.

Centimetric bubbles are produced by 'bubbling', i.e. by injecting air through a tube exiting in a liquid pool. Buoyancy force detaches bubbles that were linked to the inlet tube by capillarity. At small scales buoyancy forces (proportional to the volume) are inefficient compared to capillary forces (proportional to the perimeter). Therefore an active method is needed to produce tiny bubbles. The bubble detachment can be achieved at small scales with the help of a co-flowing liquid stream, focusing the gas jet through a tiny orifice ('flow-focusing' technique) [Marmottant and Raven, 2009].

An example of microfluidic device for implementing this method has been developed [Colosi, 2013]. The channels, made of PDMS, have been fabricated by soft lithographic processes. The device includes three inlets (two for the insertion of a polymeric liquid and one for the gas flow) and one outlet.

The geometry of the microfluidic chip is reported in Figure 7.30.

Maria Teresa Francomano

The main steps of the fabrication process are outlined in Figure 7.31. The master mold is obtained by photolithography of SU-8/100: 1ml/inch has been spun coated (2000 rpm) in order to obtain a layer 150um thick. Then a two steps soft bake is performed (15 min at 60°C and 45 min at 90°C). An UV exposure phase follows and finally a two steps post bake (1min at 60°C and 12 min at 90°C). The obtained SU-8 master mold is reported in Figure 7.32(A). The PDMS is finally deposited on the mold and after curing it is peeled off from the mold. The PDMS structure obtained is showed in Figures 7.32(B).

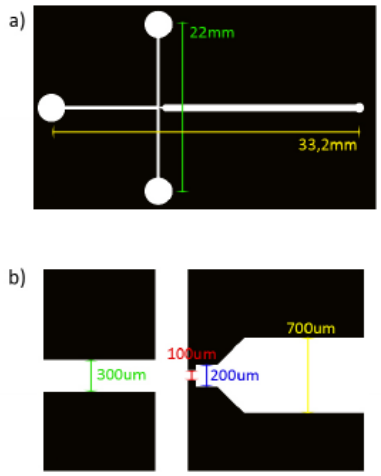

Figure 7.30: a) Whole microfluidic chip sizes; b) Channels dimensions.

In order to have close channels, 300um high, two layers of patterned PDMS are bonded by applying a light pressure.

The microfluidic chip is finally packaged, obtaining the structure in Figure 7.33.

The mechanism of bubble formation is due to the periodic pinch-off of the gas jet by the liquid stream [Dollet, 2008]. Pinch-off occurs in the small orifice, 100um wide (Figure 7.34). There are two control parameters: the gas pressure, P_g, and the liquid flow rate, Q_l,. The pinch-off frequency, f, is proportional to the liquid flow [Marmottant and Raven, 2009].

The experimental set up (Figure 7.35) includes a gas reservoir, a pressure regulator and a digital pressure gauge, a microscope and a microfluidic pump for liquid dispensing.

Maria Teresa Francomano

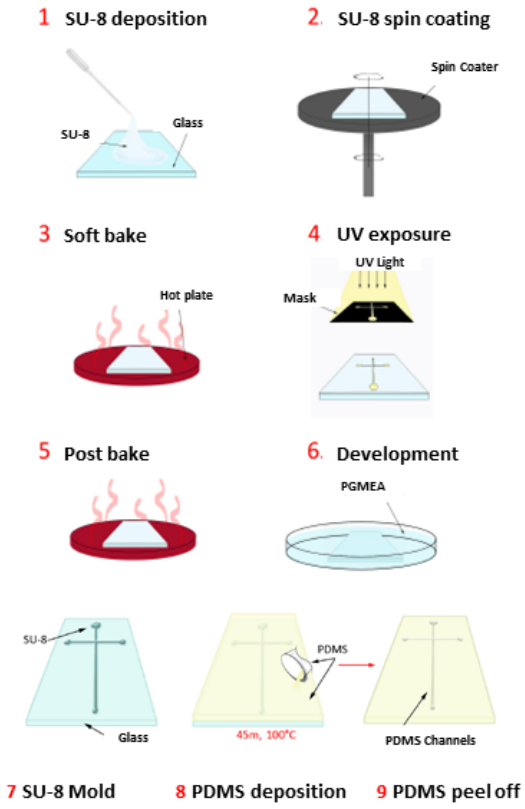

Figure 7.31: Main steps of the microfluidic chip fabrication.

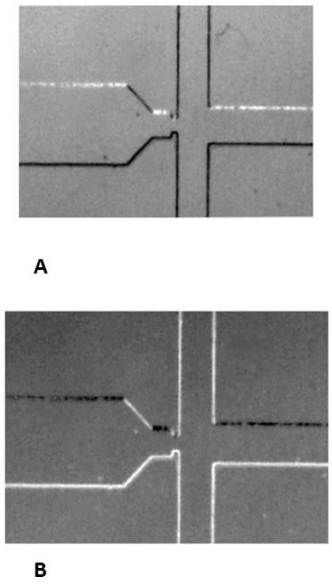

Figure 7.32: Photos of the SU-8 Master mold (A) and of the PDMS replica (B).

Maria Teresa Francomano

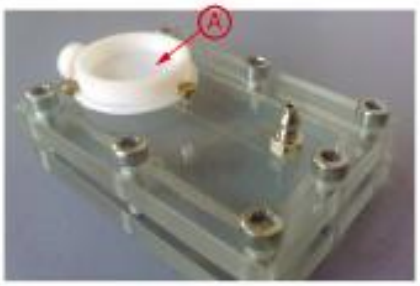

Figure 7.33: Microfluidic chip packaging. (A) is the foam reservoir.

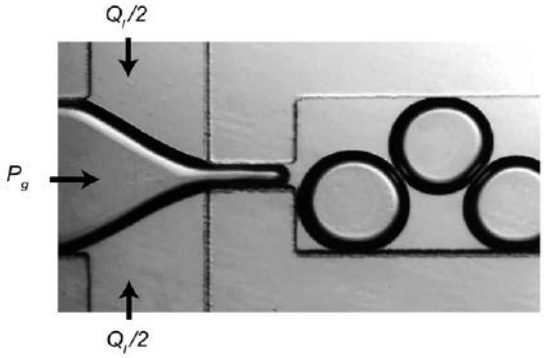

Figure 7.34: Pinch-off mechanism at the orifice. Q_l is he liquid flow, and P_g is the gas pressure.

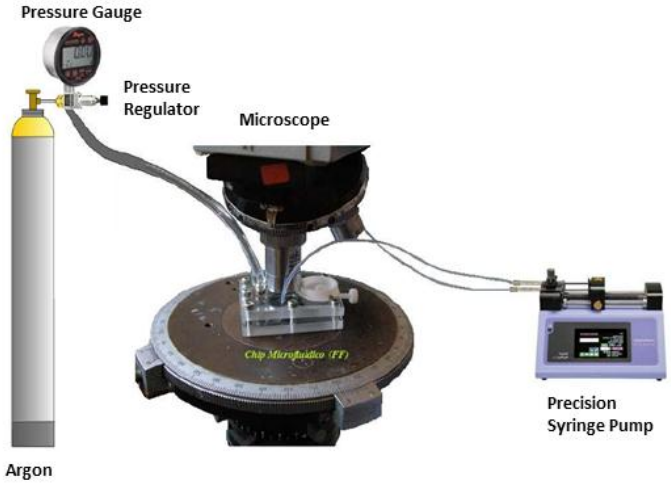

Figure 7.35: Experimental set-up. The gas is Argon. A pressure regulator (Parker 8310) and a pressure gauge (Dwyer DCG) have been used. The microscope includes a camera, connected to the workstation for capturing static and dynamic images. Finally the liquid flow is regulated by a precision syringe pump (Harvard Apparatus Pump 11 Elite)

Maria Teresa Francomano

Examples of results obtained by varying process parameters (i.e. P_g and Q_l) are reported in Figure 7.36.

When the density of bubbles is high enough, the foam is formed in the exit channel. Because of their sizes, bubbles are monodisperse and they promptly self-assemble in ordered patterns (namely 'flowing crystals' or 'microfluidic crystals') (Figure 7.37).

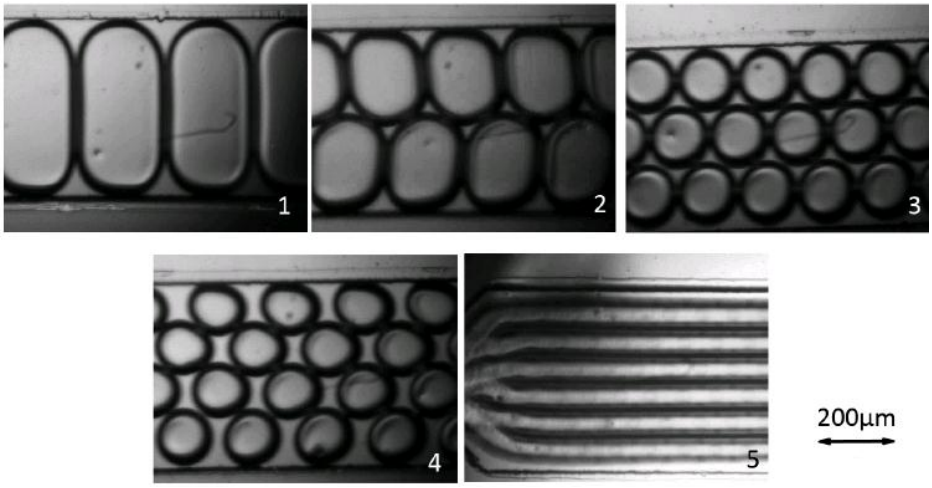

Figure 7.36: Pattern obtained in the output channel. Set parameters: 1. P_g=28.61 KPa, Q_l=2ul; 2. P_g=19.31 KPa, Q_l=3ul; 3. P_g=31.92 KPa, Q_l=3.8 ul; 4. P_g=45.09 KPa, Q_l=4.5ul; 5. P_g=46.54 KPa, Q_l=6ul.

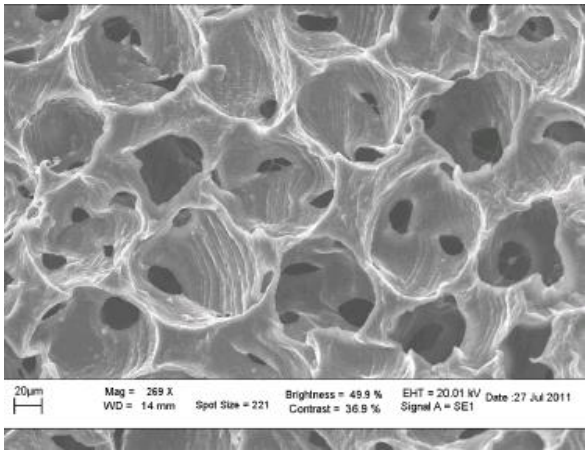

Figure 7.37: SEM image of an obtained foam.

The polymer used in this experiment is the Polyvinyl alcohol (PVA), which is water- soluble and biocompatible.

Maria Teresa Francomano

The gas used for the bubbles is Argon. Once the foam is developed in the microchannel and reserved in the output reservoir, it is frozen in liquid nitrogen, in order to firm up. Finally a freeze-dry process is performed in order to remove water, initially present in the liquid polymeric phase.

The obtained foam is dry and not compliant. However the developed microfluidic chip is flexible for being used with other polymeric means, in order to obtain a soft foam.

Finally, it is worth restating that the tuning of only two parameters, i.e. Q_l and P_g, allows to simply modulate the bubble sizes during the foam generation, thus obtaining heterogeneous patterns.

7.7. Discussion

In order to develop a sensorized skin, covering the robotic hand and accommodating all robotic fingers movements, stretchable technologies have been addressed, since stretchable devices can be deformed from a flat surface into any shape.

The substrate employed is a soft polyurethane (PU) foam. The non uniform structure of this material confers heterogeneous properties to the substrate, such as in the human skin, especially in terms of mechanical features (e.g. tunable Young's Modulus value).

An array of capacitive pressure sensors has been embedded in a multilayered PU foam structure. Preliminary tests demonstrate the sensors capability in detecting contact events as well as in discriminating pressure values, ranging from 1.2 kPa to about 6kPa.

Nevertheless, the integration on robotic fingers implies a further characterization of the sensors in both static and dynamic conditions, as well as the development of an accurate model describing the relation between the mechanical features of the substrate and the sensors performance.

Finally, the development of an engineered PU foam substrate, i.e. designed to have known spatial modulated mechanical properties (e.g. using the flow

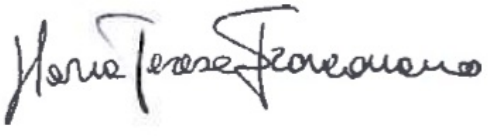

focusing method, section 7.6) and integrating slip and pressure sensors could be a huge improvement towards the realization of a fully-functional skin.

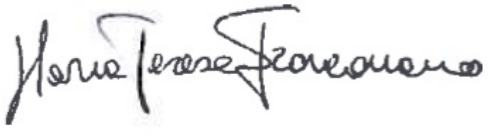

Bibliography

[AD7147 Datasheet] www.analog.com

[Corbelli, 2011] G. Corbelli et al., Advanced Materials, 23, 4504, 2011.

[Baca, 2008] A. J. Baca, J.-H. Ahn, Y. Sun, M. A. Meitl, E. Menard, H.-S. Kim, W. M. Choi, D.-H. Kim, Y. Huang, J. A. Rogers, Angew. Chem. Int. Ed. 2008, 47, 2.

[Colosi, 2013] C. Colosi, et al., Langmuir 2013 29 (1), 82-91.

[Brosteaux, 2007] Brosteaux D et al. Design and fabrication of elastic interconnections for stretchable electronic circuits. IEEE Electron Dev Lett 2007;28:552–4.

[Dinyari, 2008] R. Dinyari, S.-B. Rim, K. Huang, P. B. Catrysse, P. Peumans, Appl. Phys. Lett. 2008, 92, 169901.

[Dollet, 2008] B. Dollet et al., "Role of channel geometry on the bubble pinch-off in flow-focusing devices", The America Physical Society, 2008.

[Fjelstad, 2011] J. Fjelstad, "Flexible Circuit Technology", 4th Edition, BR Publishing, Inc., Seaside, OR, USA, 2011.

[Gonzalez, 2008] Gonzalez M et al. Design of metal interconnects for stretchable electronic circuits. Microelectron Reliab 2008;48(6):825–32.

[Gonzalez, 2011] M. Gonzalez, "Design and implementation of flexible and stretchable systems", Microelectronics Reliability 51 (2011) 1069–1076.

[Hansen, 2007] T. S. Hansen, K. West, O. Hassager, N. B. Larsen, Adv. Funct. Mater. 2007, 17, 3069.

[Hsu, 2009] Hsu YY et al. In situ observation on deformation behavior and stretchinginduced failure of fine pitch stretchable interconnect. J Mater 2009;24(12):3573–82.

[Jiang, 2007] H. Jiang, D.-Y. Khang, J. Song, Y. Sun, Y. Y. Huang, J. A. Rogers, Proc. Natl. Acad. Sci. USA 2007, 104, 15607.

[Kim, 2008] D.H. Kim and J. A. Rogers, "Stretchable Electronics: Materials Strategies and Devices", Adv. Mater. 2008, 20, 4887–4892.

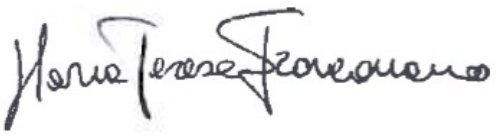

[Kim, 2008b] Kim DH et al. Materials and noncoplanar mesh designs for integrated circuits with linear elastic responses to extreme mechanical deformations. Natl Acad Sci USA 2008;105(48):18675–80.

[Kim, 2012] D. H. Kim, R. Ghaffari, N. Lu, and J. A. Rogers, “Flexible and Stretchable Electronics for Biointegrated Devices”, Annu. Rev. Biomed. Eng., vol. 14, pp. 113-128, Aug. 2012.

[Lacour, 2003] Lacour S et al. Stretchable gold conductors on elastomeric substrates. Appl Phys Lett 2003;82:2404.

[Lacour, 2006] S.P. Lacour, T. Li, D. Chan, S. Wagner, Z. Suo, “Mechanisms of reversible stretchability of thin metal films on elastomeric substrates”, Applied Physics Letters, 2006, vol. 88, p. 204103_1-204103_3.

[Lu, 2007] Lu N et al. Metal films on polymer substrates stretched beyond 50%. Appl Phys Lett 2007;91:221909.

[Lumelsky, 2001] Lumelsky VJ et al. Sensitive skin. IEEE Sens J 2001;1(1).

[Marmottant and Raven, 2009] P. Marmottant, and J.-P. Raven, "Microfluidics with foams", Soft Matter, 2009, 5, 3385–3388.

[Sekitani, 2008] T. Sekitani, Y. Noguchi, K. Hata, T. Fukushima, T. Aida, T. Someya, Science Express 2008.

[Someya, 2005] T. Someya, Y. Kato, T. Sekitani, S. Lba, Y. Noguchi, Y. Murase, H. kawaguchi, T. Sakurai, Proc. Natl. Acad. Sci. USA 2005, 102, 12321.

[Sun, 2007] Y. Sun, J. A. Rogers, J. Mater. Chem. 2007, 17, 832.

[Urdaneta, 2007] M. G. Urdaneta, R. Delille, E. Smela, Adv. Mater. 2007, 19, 2629.

[Vandeparre, 2013] H. Vandeparre, I. R. Minev, Q Liu, Z. Suo, and S.P. Lacour, "Fold and crack localization in thin films coated on microcellular elastic substrates", submitted to Advanced Materials, January 2013.

[Yu, 2007] Yu Z et al. Stretchable microelectrode array: a potential tool for monitoring neuroelectrical activity during brain tissue deformation. J Neurotrauma 2007;24:1278 [P200].

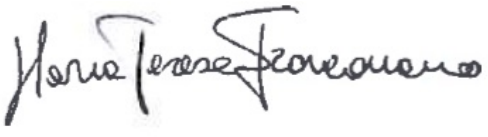

Chapter 8

Conclusion

Human manipulation capabilities, exploited in about 60% of daily life activities, are still unmatched. To get close to the performance of their biological counterpart, hand prostheses should allow the manipulation of objects even without additional (e.g. visual) cues, and the effective regulation of both force and precision grasps.

To this aims, a sufficient exteroceptive sensory feedback is mandatory as well as a reliable bidirectional communication channel between the nervous system and the robotic prosthetic device (Figure 1.1).

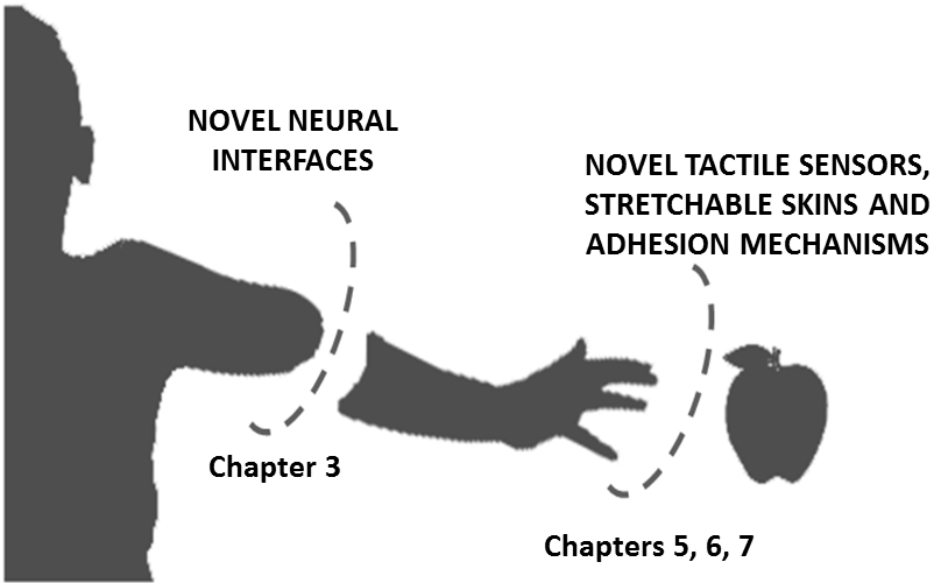

Figure 8.1: Main PhD thesis addressed issues.

Maria Teresa Francomano

Both of these challenges have been addresses in this Phd thesis, the first topic (i.e. neural interfaces) has been addressed in Chapter 3, whereas the second topic (i.e. exteroceptive interfaces) in Chapters 5, 6 and 7 (Figure 8.1).

8.1. Overview of the presented work

The first part of this work focuses on the problem of effectively interfacing the human limb to a robotic prosthesis, presenting a feasibility analysis of a novel neural interface for the peripheral nervous system, combining high selectivity, low invasiveness and resilience against physiological reactions. The main novelty aspect is in the stimulation strategy: the interface consists of implantable microprobes that electromagnetically excite peripheral nerves in a selective way, while reducing the impact of fibrotic tissue. Standard electric recordings can be used in the efferent channel. The analytical investigation, performed taking into account also thermal constraints, provided evidence of the feasibility of the proposed approach.

The second part of the presented work is centered on the problem of effectively interfacing a prosthesis to manipulated object, in order to obtain a proper sensory flow. A critical overview of the state-of-the-art of current existing devices showed that contact, pressure and slip detection, are the most important sensing modalities for characterizing static and dynamic events during objects manipulation.

An electronic skin has been developed. The skin is a multilayered structure embedding capacitive sensors, able to detect light contact with plastic and metallic objects, as well as the applied pressure (the minimum value detectable is 1.2kPa). The readout electronics, developed on a flexible substrate (i.e. polyimide) is integrated on the skin (in correspondence of the upper surface of the robotic phalanxes, once the skin is folded). The layers of the skin are made of a heterogeneous stretchable substrate, i.e. polyurethane foam. The peculiarity of the substrate relies on the tunability of its mechanical properties, attained by varying the thickness and the density of the foam. To this regard a possible technique for modulating in a controlled way the pattern of the microcellular

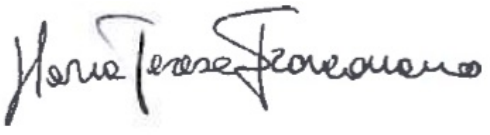

structure of the foam in also proposed, mainly based on generating polymeric foam by microfluidic chips, implementing the "flow focusing technique".

Contact and pressure sensors anyhow are not sufficient for characterizing also dynamic events such as handled object slip occurrence.

Slip detection is crucial for performing effective manipulation tasks. In fact, during the manipulation of delicate or fragile objects, it is important to reduce interaction forces to their lowest effective value, in order to avoid damaging the object, while still guaranteeing a stable grasp.

A novel slip sensor has been developed. The sensor has no moving parts and exploits a thermo-electrical transduction principle. Since the sensor does not rely on the detection of vibrations, mechanical noise, e.g. produced by motors, does not affect its performance. Moreover, it is equally effective on rough and smooth objects. The sensing element and its electrical connection are sandwiched between the two polyimide layers, which have the same thickness, thus lying on the neutral plane of the structure. This configuration preserves the metal from possible structural failures caused by tensile stresses that may arise during bending. The sensor characterization returns response times less than 50 ms, i.e. comparable to the human mechanoreceptors response time. Moreover, an array configuration of thermal slip sensors has been developed. The sensory system is able to detect the starting point of a slip event and its direction. Finally, in order to integrate the readout electronics on the same substrate (i.e. silicon) housing the sensing elements, the bending capabilities of a multilayered structure have been analyzed and design constraints have been retrieved.

Once slip occurrence is detected, an adaptation of forces occurs. This mechanism is arduous in case of a wet object is manipulated, due to its slippery surface. In order to address this problem, thus allowing to achieve a stable grasp, a novel technique for modulating the adhesion forces on wet surfaces has been implemented. The technique (patented and named "electrowet adhesion") merges principles from electrowetting and wet adhesion. A voltage-controlled engineered surface has been developed in order to implement the proposed technique. Results show variation up to 30% of the adhesion force.

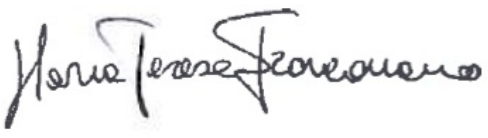

8.2. Major achievements beyond the state of the art

In this thesis the investigations on novel solutions for overcoming current technological limitations at the interface between the prosthetic hand and the human neural system as well as between the former and the manipulated objects are reported.

For both interface levels (Figure 1.1, Figure 8.1) common microfabrication technologies and materials have been used, with the final aim of having flexible/stretchable systems. Hence mechanical mismatches at the interface are reduced and the foldability of the developed devices around complex and dynamic surfaces is allowed.

The major achievements obtained beyond the current state of the art, can be outlined as follow:

1. *Enabling microtechnologies for improving the interface between the prosthesis and the neural system:*

- Theoretical feasibility analysis of a novel birectional neural interface based on EM stimulation.

2. *Enabling microtechnologies for improving the interface between the prosthesis and the object:*

- Contact/pressure sensors on a heterogeneous stretchable substrate.
- Flexible slip microsensors with performance comparable to those of human mechanoreceptors.
- Flexible arrays of slip microsensors able to detect slip direction.
- A novel technique and device for modulating the adhesion force at the interface with wet surfaces.

In conclusion, the developed enabling technologies contribute to tackle the challenge of effectively restoring the interrupted link between the amputees body and the external environment.

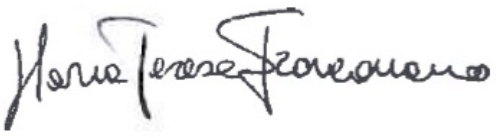

8.3. Further improvements and potential impact

The work presented in this PhD thesis can be considered as a deep investigation of novel solutions for challenging issues related to prosthetics. The next step is to further improve the technologies mainly for effectively integrating them in an advanced prosthetic hand and for testing the performance of the device in a real scenario.

To this aim some of the possible advancements that can be addressed to improve the presented solutions are outlined:

- According to the main outcomes of the feasibility analysis reported in Chapter 3, the design optimization, as well as the fabrication and testing (both *in vitro* and *in vivo*), of the proposed neural microprobes, for interfacing artifacts with the peripheral neural system, is required for assessing the effectiveness of the *in situ* EM stimulation of nervous fibers. Special attention should be devoted to evaluate the selectivity of stimulation, i.e. the capability to address specific nervous fibers.
- As it regards, the thermal slip sensors and the capacitive pressure sensors, further improvements require the implementation of intelligent and adaptive control algorithms. The integration of the sensors on a robotic hand and the development of a manipulation control scheme, integrating the sensors signals, should also be performed.
- A major achievement could be the development of an artificial skin, embedding the tactile sensors (i.e. slip and pressure sensors) and the engineered surface for actively controlling the adhesion forces using the *electrowet adhesion* principle. This task can be accomplished both by integrating the developed technologies in a hybrid flexo-stretch skin, as well as by adequately translating the proposed devices on a unique stretchable substrate.
- Finally, it would be interesting to investigate the possibility of restoring the original sensory perceptions of the hand, by transferring stimuli coming from the artificial exteroceptive sensors, in the bionic limb, to the human nervous system. This task could be accomplished by modifying the sensory system in order to provide output signals compatible to the novel neural

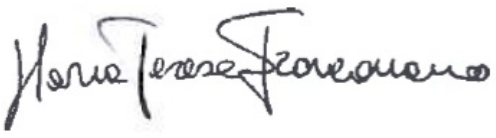

interfaces technology (e.g., neuromorphic signals, i.e. voltage pulses, resembling the neurons spikes of action potentials).

In conclusion, it is worth mentioning that there are other fields where both the proposed technologies (i.e. neural interfaces and exteroceptive engineered surfaces including tactile sensors and adhesion mechanisms) could potentially enable novel functionalities or improve existing ones. Such fields include, for example: haptics and wearable robotics, interactive electronics, robotic surgery, telemedicine, immersive reality, etc. To enlarge towards these directions the potential impact of the researches presented in this work, new and application-oriented studies could be undertaken.

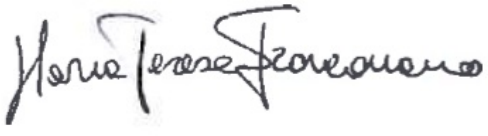

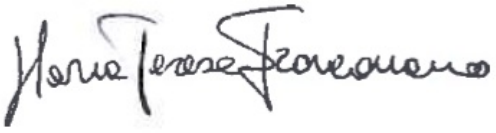

List of Publications

Patents

[1] Accoto D., Francomano M. T., Esposito C., (2012). Dispositivo e metodo per adesione controllata su substrato umido (Device and method for controlling adhesion on wet substrates). RM2012A000026.

Peer-reviewed journals

[2] M. T. Francomano, D. Accoto, and E. Guglielmelli, "Experimental characterization of a flexible thermal slip sensor", Sensors, 12(11), 15267-15280, 2012.

[3] D. Accoto, M. T. Francomano, A. Rainer, M. Trombetta, P. M. Rossini, E. Guglielmelli, "An implantable neural interface with electromagnetic stimulation capabilities", Medical Hypothesis, accepted, January, 2013.

[4] M. T. Francomano, D. Accoto, and E. Guglielmelli, "Artificial Sense of Slip–A Review", IEEE Sensors Journal, 2013, DOI:10.1109/JSEN.2013.2252890.

Peer-reviewed International conference proceedings

[5] D. Accoto, M. T. Francomano, A. Benvenuto, C. Luccarelli,E. Guglielmelli, "Optimization of a thermal slip sensor using FEM and dimensional analysis", in Proc. 3rd IEEE RAS & EMBS International Conference on Biomedical Robotics and Biomechatronics, Tokyo, Japan, September 26-29, pp. 855-860, 2010.

[6] Sudano, D. Accoto, M. T. Francomano, F. Salvinelli, E. Gugliemelli, "Optimization of kinetic energy harvesters design for fully implantable cochlear implants", in Proc. 33rd Annual International Conference of the Engineering in Medicine and Biology Society, Boston, Massachusetts USA, August 30 - September 3, pp. 7678-7681, 2011.

[7] M. T. Francomano, D. Accoto, E. Morganti, L. Lorenzelli, E. Guglielmelli, "A microfabricated flexible slip sensor", in Proc. 4 th IEEE RAS & EMBS International Conference on Biomedical Robotics and Biomechatronics. Rome, Italy, June 24-27, pp. 1919-1924 , 2012.

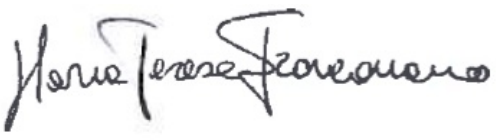

[8] M. Moscato, E. Schena, P. Saccomandi, M. T. Francomano, D. Accoto, S. Silvestri, "A micromachined intensity-modulated fiber optic sensor for strain measurements: working principle and static calibration", in Proc. 34th Annual International Conference of the Engineering in Medicine and Biology Society, August 28- September 1, San Diego, California USA, 2012.

[9] D. Accoto, M. Cidda, E. Schena, M.T. Francomano, P. Saccomandi, E. Guglielmelli, and S. Silvestri, "A micro opto-mechanical displacement sensor based on micro-diffraction gratings: design and characterization", accepted, EMBC 2013.

National and International Conference/Workshop Abstracts

[10] D. Accoto, M. T. Francomano, A. Benvenuto, E. Guglielmelli, "A tactile microsensor for advanced robotic prosthetics", MEMS In Italy, Otranto (Italy) June28 -July 1 2010.

[11] M. T. Francomano, D. Accoto, A. Benvenuto and E. Guglielmelli, "A slip microsensor for hand prosthetics application", GNB 2010, Torino (Italy), July 8-10, 2010.

[12] M. T. Francomano, D. Accoto, and E. Guglielmelli, "A microsensor on flexible substrate for slip detection", GNB2012, Rome (Italy), June 26-29, 2012.

[13] M. T. Francomano, N. Sommer, S. El Khoury, J. L. Bolli, M. Lauria, H. Vandeparre, J. B. Keller, A. Billard, S. P. Lacour, "Artificial finger phalanges' skin for robotic hands", 2013 MRS Spring Meeting & Exhibit, San Francisco (USA), 1-5 April, 2013.

[14] M. Cidda, E. Schena, D. Accoto, M. T. Francomano, E. Guglielmelli, and S. Silvestri, "Design and characterization of a micro opto-mechanical displacement sensor", XVII AISEM Annual Conference, Brescia, February 5-7 2013.

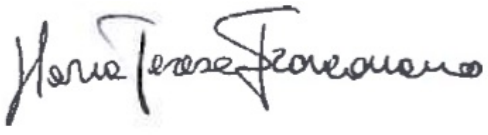

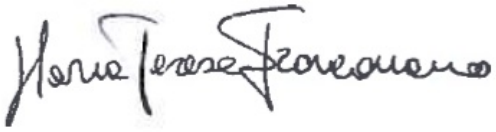

Acknowledgements

This last page of the thesis is dedicated to the people who shared with me this long, hard but fulfilling road.

First of all I would like to thank Professor Eugenio Guglielmelli for giving me the possibility of participating in several research activities, believing in my abilities and helping me with precious advices.

I would like to express my gratitude to Dino, my mentor. I have to thank him for keeping pushing me towards new challenges (which, frankly speaking, often made me nervous), thus helping me to acquire scientific and organizational skills.

I would also like to thank the Reviewer of the thesis, Professor Stéphanie Lacour, who provided precious and constructive feedback to improve this work. Moreover, I would like to thank her for hosting me in her lab during the last for six months of my PhD course. Warm thanks to the members of the LSBI and LASA, @ EPFL, for welcoming me as a friend.

I would also thank all the members of my and neighbor labs: Luca S., Edoardo, Giorgio C., Simone, Nevio, Angelo, Alessio, Rosa, Eugenia, Valentina, Eleonora, Francesco, Luca R., Fabrizio T., Domenico, Giovanni, Alessandro, Loredana, Flavia S., Giorgio P., Marco S., Flavia B., Emiliano, Roberto, Edda, for the great time spent together as colleagues and friends. Thanks also to Fabrizio S., Nino and Max!

A special thanks goes to Antonella and Anna Lisa, my two dear friends, next to me in good and bad times (and viceversa)!

I would like also to thank my friends: Mary, Antonio, Marco, Marianna, Mara and Giovanna.

Last but not least I would like to thank my parents, my brother Antonio and all my whole loving family.